AD_____

Award Number: W81XWH-07-1-0454

TITLE: Photonic Breast Tomography and Tumor Aggressiveness Assessment

PRINCIPAL INVESTIGATOR: Swapan K. Gayen, Ph. D.

CONTRACTING ORGANIZATION: Research Foundation of CUNY
                                                    New York, NY 10019-2925

REPORT DATE: July 2011

TYPE OF REPORT: Annual Summary

PREPARED FOR: U.S. Army Medical Research and Materiel Command
                            Fort Detrick, Maryland 21702-5012

REPORT DOCUMENTATION PAGE

Form Approved
OMB No. 0704-0188

1. REPORT DATE	2. REPORT TYPE	3. DATES COVERED
July 2011	Annual Summary	15 June 2010 – 14 June 2011

4. TITLE AND SUBTITLE

Photonic Breast Tomography and Tumor Aggressiveness Assessment

5a. CONTRACT NUMBER

5b. GRANT NUMBER
W81XWH-07-1-0454

5c. PROGRAM ELEMENT NUMBER

6. AUTHOR(S)

Swapan K. Gayen, J. A. Koutcher, X. Ni, M. Alrubaiee, Binlin Wu

E-Mail: gayen@sci.ccny.cuny.edu

5d. PROJECT NUMBER

5e. TASK NUMBER

5f. WORK UNIT NUMBER

7. PERFORMING ORGANIZATION NAME(S) AND ADDRESS(ES)

Research Foundation of CUNY
New York, NY 10019-2925

8. PERFORMING ORGANIZATION REPORT NUMBER

9. SPONSORING / MONITORING AGENCY NAME(S) AND ADDRESS(ES)
U.S. Army Medical Research and Materiel Command
Fort Detrick, Maryland 21702-5012

10. SPONSOR/MONITOR'S ACRONYM(S)

11. SPONSOR/MONITOR'S REPORT NUMBER(S)

12. DISTRIBUTION / AVAILABILITY STATEMENT
Approved for Public Release; Distribution Unlimited

13. SUPPLEMENTARY NOTES

14. ABSTRACT

The tasks performed and the progresses made during the fourth year include: (a) carrying out research on development of non-invasive near-infrared (NIR) diffuse optical imaging (DOI) approaches for detection of breast tumors in early stages of growth when those are more amenable to treatment; and (b) training of CCNY researchers at MSKCC in magnetic resonance spectroscopic imaging (MRSI) for detection of lactate in tumors. The NIR optical imaging research involved: (i) development of time reversal optical tomography (TROT) approach for imaging of single absorbing and single scattering targets as a function of position, and two targets as a function of separation between them;(ii) adaptation and comparison of Principal Component Analysis (PCA) and Non-negative Matrix Factorization (NMF)methods to DOI problem and comparing those with previously-developed OPTICA (optical tomography using independent component analysis). These approaches were demonstrated to be suited for detecting and locating small targets in tissue-simulating turbid media. MRSI investigation of lactate holds promise for assessment of tumor aggressiveness. A new research pre-proposal was developed and submitted to CDMRP 2011 BCRP Idea Award category for funding.

15. SUBJECT TERMS
Breast cancer, near-infrared imaging, optical tomography, independent component analysis, principal component analysis, non-negative matrix factorization, time reversal optical tomography, finite element method, lactate detection, magnetic resonance spectroscopy and imaging

16. SECURITY CLASSIFICATION OF:

a. REPORT	b. ABSTRACT	c. THIS PAGE	17. LIMITATION OF ABSTRACT	18. NUMBER OF PAGES	19a. NAME OF RESPONSIBLE PERSON USAMRMC
U	U	U	UU	78	19b. TELEPHONE NUMBER *(include area code)*

Table of Contents

Page

4. INTRODUCTION

The HBCU/MI Partnership Training Award project, "*Photonic Breast Tomography and Tumor Aggressiveness Assessment*," is designed to establish a breast cancer training and research program at the City College of New York (CCNY) through close collaboration with the researchers at the Memorial Sloan Kettering Cancer Center (MSKCC). The focus of the training component of the project is to familiarize the CCNY researchers who happen to be physical scientists and engineers to the biological aspects of cancer research through attending relevant courses, and cancer research practicum through laboratory rotations. The objectives of the research component of the project are to develop optical imaging and spectroscopic approaches to (a) distinguish between aggressive and slow growing, metastatic and non-metastatic tumors, (b) non-invasively detect and diagnose breast tumors at early stages of growth.

During the *fourth* reporting period (June 15, 2010 – June 14, 2011) covered by this report, the major research thrust was on developing near-infrared (NIR) light-based experimental methods and numerical algorithms for detection of targets in breast tissue simulating model medium with the goal of detecting breast tumors at early stages of growth. The trainees also continued learning the magnetic resonance spectroscopic imaging (MRSI) with selective multiple-quantum coherence transfer (SelMQC) sequence to explore its potential to investigate the glycolytic activity of tumors.

5. BODY

We have made substantial progress in developing **non-invasive near-infrared optical imaging modalities for early detection of breast cancer** (*Specific Aim 4*) that we started during Year 1 of the project [1] and pursued and reported in the subsequent years [2,3]. The goal of the research is to develop optical spectroscopy and imaging approaches that use the near-infrared light to obtain three-dimensional (3-*D*) tomographic images of human breast to enable detection, localization, and possible diagnosis of tumor(s) in the breast. Early detection of breast tumor with requisite sensitivity and specificity is a daunting task and we continued development of different approaches, which include:

- *Diffuse Optical Imaging using Decomposition Methods;*
- *Time Reversal Optical Tomography (TROT);* and
- *Finite element method* (FEM).

We provide a brief outline of activities and accomplishments in these areas, and refer to appended materials for detailed description where applicable.

5.1. Diffuse Optical Imaging Using Decomposition Methods

We have previously reported on the development of Optical Tomography using Independent Component Analysis (OPTICA), extended it to include multi-wavelength probing and explored its efficacy on a more realistic model breast (*Specific Aim 4, Task #15 and Task #16*) [2-4]. Diffuse optical imaging (DOI) for detection and retrieval of location information of targets in a highly scattering turbid medium may be treated as a "blind source separation" (BSS) problem [5]. Independent Component Analysis (ICA), the basis for OPTICA, is one of the different matrix decomposition methods for solving the BSS problem and retrieving desired information. Other decomposition methods include Principal Component Analysis (PCA) [6] and Non-

negative Matrix Factorization (NMF) [7]. The three algorithms have different assumptions, which may lead to different favored conditions.

ICA assumes the signals from different targets to be independent of each other, and optimizes a relevant measure of independence to obtain the ICs associated with different targets [4]. The position co-ordinates of targets in three dimensions are determined from the individual components separately. PCA [6] assumes that the PCs contributing to the signal are uncorrelated and explain the most variance in the signal. NMF [7] seeks to factorize a matrix into two non-negative matrices (component signals and weights) and requires the contributions to signal and the weights of the components to be non-negative. It does not imply any relationship between the components. Our objective was to test and compare the efficacy of these three approaches in solving the DOI problem. We used both simulative data and experimental data for absorptive and scattering targets embedded in model scattering media. Details of the theoretical formalism, numerical algorithms, simulation and experiment are detailed in the pre-print of a submitted paper (*attached as Appendix 3*); only a brief overview is presented below.

Blind source separation (BSS), also known as blind signal separation is a general problem in information theory that seeks to separate the contributions from different sources to the measured signal, which is a weighted mixture of signals from those sources. Assuming the source signals are linearly mixed, the BSS problem can be presented in matrix notation as, *X=AS*, where *X* represent measured signal, *A* is a mixing or weighting matrix, and S represents signals from the sources. The objective of BSS is to retrieve the source signals and their weights from the measured signal. Due to the lack of prior knowledge of the source signals, statistical analysis methods, such as ICA, PCA and NMF are used to retrieve source information.

In DOI one measures the signal at the sample boundary, which is a weighted mixture of contributions from embedded targets. The signal is the perturbation in the light intensity distribution at the sample boundary, and ideally is the difference between the signal recorded with the target(s) and that without the targets. In practice signal without the targets is reasonably approximated by an average of the signals recorded for different scanning positions of the sample. DOI is thus a BSS problem in the optical domain, and the problem was investigated using three matrix decomposition approaches, ICA, PCA and NMF, for absorptive and scattering targets.

In *simulation*, the sample was considered to be a 40-mm thick uniform slab of scattering medium, as shown in Fig. 1 of *Appendix 3*. Its absorption and diffusion coefficients were taken to be $\mu_a = 0.003$ mm^{-1} and D = 1/3 mm, respectively, which are similar to the average value of those parameters for human breast tissue. An absorptive and a scattering point target were placed at (50, 60, 15) mm and (30, 30, 25) mm, respectively. The absorption coefficient of the absorptive target was set to be higher than the background with $\Delta\mu_a = 0.01$ mm^{-1}, while the diffusion coefficient was taken to be the same as that of background. The diffusion coefficient of the scattering target was set to be lower than the background (higher scattering coefficient) with $\Delta D = -1$ mm, while the absorption coefficient was taken to be the same as the background. The incident CW beam was assumed to step scan the sample at 21×21 grid points covering 80×80 mm^2 area, with a step size of 4 mm. Light on the opposite side was recorded at 41×41 grid points covering the same area. Multiplicative Gaussian noise of 5% was added to the simulated data. The data matrix *X* was then obtained, and analyzed using the three different algorithms.

To evaluate the efficacy of the decomposition methods in *experiments*, we carried out two different experiments with two different samples. The first sample used a 250 mm × 250 mm × 50 mm transparent plastic container filled with Intralipid-10% suspension in water as the background medium. The concentration of Intralipid-10% was adjusted to provide [8,9] an absorption coefficient of μ_a ~ 0.003 mm-1, and a transport mean free path l_t ~ 1.43 mm at 785 nm. The second sample used a similar container with dimension of 250 mm × 250 mm × 60 mm filled with Intralipid-20% suspension in water. The concentration of Intralipid-20% was adjusted to provide [8, 9] μ_a ~ 0.003 mm^{-1}, and l_t ~ 1 mm at 790 nm. These optical parameters of the medium were selected to be similar to those for human breast tissue. The thickness of the samples was also comparable to that of a typical compressed female human breast.

In the first experiment, two absorptive targets were embedded in the medium. The targets were ~ 10-mm diameter glass spheres filled with a solution of Indo-cyanine green dye in water. The absorption coefficient μ_a was adjusted to be 1.15 mm^{-1} at 785 nm, with μ_s approximately the same as that of the background medium. The targets were placed at (57.2, 18.1, 20.0) mm and (19.9, 48.1, 25.0) mm, respectively. In the second experiment, two scattering targets were embedded, which were also ~ 10 mm diameter glass spheres, filled with Intralipid-20% suspension in water. The transport mean free path, l_t was adjusted to be 0.25 mm, with scattering coefficient $\mu_s \approx 11$ mm^{-1}, and absorption coefficient μ_a same as the background medium. The targets were placed in the mid-plane ($z = 30$ mm) in the container with a lateral distance of 40 mm from each other (center to center).

The experimental setup (shown schematically in Fig. 6 of *Appendix 3*), was based on what we assembled (*Specific Aim 4, Task #14*) earlier in the project [1]. A 10-mW 785-nm diode laser beam was used to illuminate the first sample, while a 100-mW 790-nm diode laser beam was used for the second sample. The input surface (source plane) of the samples was scanned across the laser beam in an x-y array of grid points to realize the multi-source interrogation of the samples. The transmitted light from the exit surface (detector plane) was recorded by a 1024 pixel ×1024 pixel (pixel size = 24 µm) CCD camera (Photometrics CH350) equipped with a 60-mm focal-length camera lens. Each pixel of the CCD camera can be considered to be a detector implementing the multi-detector signal acquisition arrangement. A set of 16-bit 1024 pixel ×1024 pixel images were acquired. The two samples were scanned in an array of 11×12 and 11×15 grid points, respectively, with a step size of 5 mm in both cases. The processes of scanning and data acquisition were controlled by a personal computer. At all scan positions, raw transillumination images of the samples were recorded by the computer for further analysis. A 16-bit 1024 x 1024 pixels CCD camera recorded the transmitted signal. The sample was scanned across the laser beam in a 16x26 *x-y* array of grid points and a two-dimensional transmission image was recorded for each position for each wavelength to meet the multi-source multi-detector (each pixel of a CCD camera being a detector element) imaging arrangement. The resulting data was analyzed using the numerical algorithm of ICA, PCA and NMF. The details of the experimental arrangement, data acquisition, processing and analysis methods are presented in attached *Appendix 3*.

The key **result** from *simulated data* is that the positions and optical strengths of the targets retrieved by ICA, PCA and NMF algorithms in excellent agreement with the known values.

The results from the *experiments* using absorptive and scattering targets demonstrate that overall, all three algorithms detect and locate the scattering and the absorptive targets with good accuracy, the maximum deviation of any one coordinate from the known value being ~3 mm.

The (*x, y, z*) positions of the targets were retrieved with good accuracy. The decomposition provided by ICA is "cleaner" than that of the PCA. PCA did not clearly separate the two absorptive targets used in the first experiment. NMF decomposition seems to provide residue-free "cleaner" images than the other two methods in this study. Appendix 3 provides further discussion on implication of results.

5.2. Time Reversal Optical Tomography

We have been pursuing development of the *Time Reversal Optical Tomography* (TROT) approach, [2, 3] in our on-going quest for fast and accurate methods for detection and localization of tumours in breast, and for detection of margins during surgical removal of breast tumours (*Specific Aim 4*).

The time reversal (TR) invariance, the basic symmetry that commonly holds in microscopic physics, forms the basis for macroscopic imaging [10] in TROT. TROT also adapts and incorporates, in optical domain, the vector subspace classification method, Multiple Signal Classification (MUSIC). MUSIC was developed by Devaney and co-workers for finding the location of scattering targets whose size is smaller than the wavelength of acoustic waves or electromagnetic waves (radar) used for probing the homogeneous or inhomogeneous background medium in which the targets were embedded [11, 12]. In optical imaging application, a *response matrix* represents the transport of light from multiple sources through a turbid medium with embedded targets to an array of detectors. The response matrix is constructed from the experimental data that represent the perturbation in light intensity distribution on the sample boundary due to the presence of target(s). The 'time reversal (TR) matrix' is constructed by multiplying the response matrix by its transpose matrix for continuous wave illumination (by adjoint matrix for frequency-domain case). Mathematically, the TR matrix is equivalent to transfer of light from multiple sources through a turbid medium with embedded targets to an array of detectors, and back, and is similar to the time-reversal matrix used in the general area of array processing for acoustic and radar time-reversal imaging [12]. The eigenvalue equation of TR matrix is solved, and the signal and noise are separated into orthogonal subspaces, using an *L*-curve regularization method. Then a pseudo spectrum is calculated directly for all voxels in the sample using MUSIC [11, 12]. Pseudo tomographic images can be generated using pseudo values. Locations of targets are determined by the global maxima (or local maxima in low SNR case) components in the pseudo spectrum. Details of the theoretical formalism and numerical algorithms of TROT along with tests of its efficacy using simulative and experimental data have been detailed in a manuscript submitted for publication in and is attached to this report as *Appendix 4*. We will present only the key results in the body of this report, and refer to *Appendix 4* for further details.

First we tested the potential of TROT in an ideal situation using a challenging problem in *simulation* that involved detecting and locating 6 targets embedded in a 40-mm thick breast tissue-simulating scattering medium. The six point-like absorptive targets, with absorption coefficient difference of $\Delta\mu_a = 0.01$ mm-1 from the background, were placed at A (24 mm, 26 mm, 9 mm), B (38 mm, 38 mm, 15 mm), C (38 mm, 38 mm, 21 mm), D (40 mm, 38 mm, 21 mm), E (44 mm, 42 mm, 21 mm) and F (30mm, 30mm, 31 mm), respectively. The origin (0 mm, 0 mm, 0 mm) was located at the upper-left corner of the input boundary (source boundary) of the sample. As can be seen from the assigned coordinates, targets C and D are located at two adjacent grid points, and are close to target E, and these three targets are located in the same *z* layer. Consequently, targets C and D are expected to be very difficult to resolve, and hard to distinguish from target E. Target B and C have the same lateral position x and y, and different depths. Target A is close to the source

plane, while F is close to the detector plane. As detailed in Section 4 of Appendix 4, TROT formalism could detect all 6 targets and retrieved their locations to be at the exact known target locations. With the highly encouraging result from simulation even for a considerably challenging task, we proceeded to test the approach for the realistic situation of detecting and locating targets from experimental data.

We have experimentally investigated the efficacy of TROT by imaging both absorptive and scattering target(s) embedded in Intralipid-20% suspension in water, a model medium whose optical absorption and scattering properties can be adjusted by varying the concentration. The initial results for the absorptive target(s) were presented in the Third Annual Report [3], and are detailed in *Appendix 4*. Here we present a brief account of the study with a scattering target and leave the details for *Appendix 4*.

The sample used a 250 mm × 250 mm × 60 mm transparent plastic container filled with Intralipid-20% suspension in water as the background medium. The concentration of Intralipid-20% was adjusted to provide an estimated [8,9] absorption coefficient $\mu_a \sim 0.003$ mm^{-1} at 790 nm, and a transport mean free path $l_t \sim 1$ mm, which were similar to the average values of those parameters for human breast tissue, while the cell thickness of 60 mm was comparable to thickness of a typical compressed breast. The target was a glass sphere of diameter 10 mm filled with Intralipid-20% suspension in water to provide a transport mean free path l_t of 0.25 mm, and a scattering coefficient $\mu_s \approx 11$ mm^{-1}. The depth of the scattering target was varied to explore the efficacy of TROT in locating and characterizing a scattering target.

A multi-source interrogation and multi-detector signal acquisition scheme, shown in Fig. 2 of Appendix 4, was used to acquire data. A 100-mW 790-nm diode laser beam was used to illuminate the samples. A 1024 × 1024 pixels charge coupled device (CCD) camera equipped with a 60-mm focal-length camera lens was used on the opposite side of the sample to detect the transmitted light on the boundaries of the slab samples (detector plane). The pixel size was 24 µm. The multi-source illumination scheme was realized by scanning the sample across the laser beam in a two-dimensional *x-y* array of grid points using a computer-controlled translation stage. The sample was scanned across the laser beam in an array of 9 × 9 grid points, with a step size of 5 mm. The scanning and data acquisition processes were controlled by a personal computer (PC).

The depths (z-positions) of the target that were used in the experiment are: 15 mm, 20 mm, 25 mm, 30 mm, 35 mm, 40 mm, and 45 mm. A typical cross-section pseudo image and the corresponding spatial profiles are displayed in Fig. 1(a) when z = 30 mm. It is compared to the simulation results with 20% Gaussian noise (Fig. 1(b)). The lateral (x, y) spatial profiles of the pseudo image generated using simulated data are considerably wider, while the axial (z) spatial profile is narrower than those obtained using experimental data, while the peak values from the two cases are of the same order. The retrieved target positions are listed in Table I.

It is evident from the results in Table I, that the TROT formalism locates the positions of the scattering target with considerable accuracy. The lateral (x, y) positions are determined with higher accuracy than the axial (z) position. The resolution of experimental result seems to be better than the simulation, which we attribute to the noise level of 20% used in simulation which presumably is higher than the experimental error.

A comparison of experimental results for scattering and absorptive targets validate the common notion that it is more challenging to locate and image scattering targets than absorptive targets in a highly scattering medium. The results from experiment and simulation show that TROT, being a non-iterative approach, is a faster and less computation intensive approach for detecting small

targets in highly scattering turbid media and determining their locations in 3-D than other inverse image reconstruction techniques.
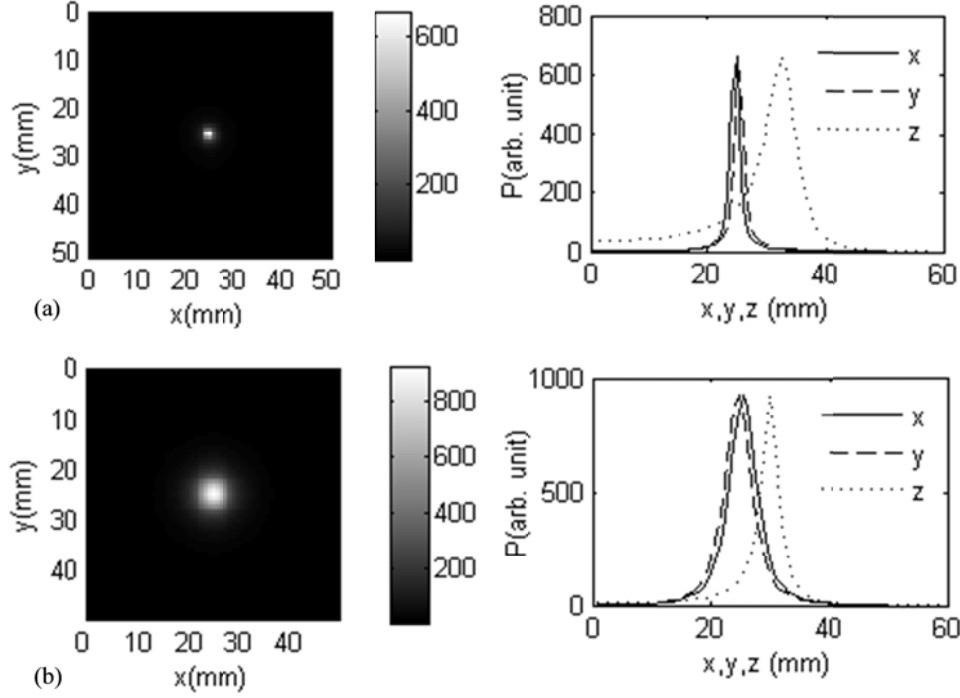

Fig.1. Pseudo image of the target (left pane) and corresponding spatial intensity profiles (right pane) when the target is located at z = 30 mm: (a) experimental data; (b) simulation with 20% Gaussian noise added. *P* is pseudo value calculated using Eq. (20) in *Appendix 4*.

Table I. Positions of a scattering target located at different depths

Known Positions [x, y, z (mm)]	Retrieved Positions [x, y, z (mm)]	Error (mm) [$\Delta x, \Delta y, \Delta z$]
25.7, 24.5, 15	24.9, 25.9, 18.5	0.8, 1.4, 3.5
25.7, 24.5, 20	27.2, 26.7, 20.5	1.5, 2.2, 0.5
25.7, 24.5, 25	25.7, 26.7, 23.5	0.0, 2.2, 1.5
25.7, 24.5, 30	24.9, 25.2, 32.5	0.8, 0.7, 2.5
25.7, 24.5, 35	24.9, 25.2, 36.5	0.8, 0.7, 1.5
25.7, 24.5, 40	24.9, 25.9, 41.5	0.8, 1.4, 1.5
25.7, 24.5, 45	24.9, 25.9, 45.5	0.8, 1.4, 0.5

We are pursuing development of the TROT formalism for extended targets, which will be suited to detect, locate, and diagnose breast tumors at later stages, as well.

5. 3. Finite Element Method for Optical Tomography

We are exploring the Finite Element Method (FEM) that has found considerable use in optical tomography [13], as another viable approach to optical mammography (*Specific Aim 4, Task# 17 and Task# 18*). One of the objectives is to use FEM to obtain optical properties around the suspect sites that TROT can locate with high accuracy without needing long computation time. While FEM is more computation intensive than TROT, using it only over the limited suspect sites located by TROT will reduce the computation time significantly.

We pursued testing and adaptation of a program called NIRFAST [14] developed by researchers at Dartmouth College for modeling NIR frequency domain light transport in tissue based on FEM. We have evaluated the program in simulation under different conditions that include number of targets, their location, size and optical properties, sample geometry, source and detector positions, and noise level. It is tested for both two-dimensional (2-*D*) and three-dimensional (3-*D*) absorptive and scattering targets. in 2D and 3D problems. Some examples are shown as below.

Two-Dimensional Problems

First, we considered the sample to be 10-cm diameter ***circle***, with background optical properties: $\mu_a =$ 0.01 mm^{-1}, $l_t = 1$ mm ($\mu_{s'} = 1$ mm^{-1}). Sixteen (16) optical fibers are assumed to be placed at the edge around the circle, equally spaced and used as both sources and detectors. In forward model, the source positions are considered to be located 1 mm below the surface [15], where the initial scatterings of the incident photons are assumed to occur. To avoid the strong boundary effect, when one fiber is used as the source, other 15 fibers are used as detectors. Measurements are taken with every fiber used in turn as a source resulting in accumulation of data using 240 source and detector pairs located 1 mm below the edge around the circle. Two absorptive and two scattering circular targets are embedded as follows.

Two absorptive and two scattering circular targets with different optical properties and sizes are embedded. The center of the circle is set to be the origin of the coordinates (0, 0) mm. The position, optical property and size of the four targets are listed in Table II.

Table II. Target position, property and size

Target#	Position (x, y) (mm)	μ_a (mm^{-1})	$\mu_{s'}$ (mm^{-1})	Radius (mm)
1	-20, -20	0.015	1	5
2	20, 20	0.02	1	2.5
3	20, -20	0.01	2	5
3	-20, 20	0.01	4	2.5

The mesh of the sample and the source (*), detector (detector) and target (circle) positions are shown in Fig. 2. Forward model data in frequency domain with modulation frequency 100 MHz was generated using NIRFAST. Background random noise level of 1% was added and compared with zero-noise case. The data is then used for reconstruction also using NIRFAST through an iterative process, where the forward model data is repeatedly calculated while varying the optical properties of every voxel, and compared with the original data. The uniform background property ($\mu_a = 0.01$ mm^{-1}, $\mu_{s'} = 1$ mm^{-1}) was
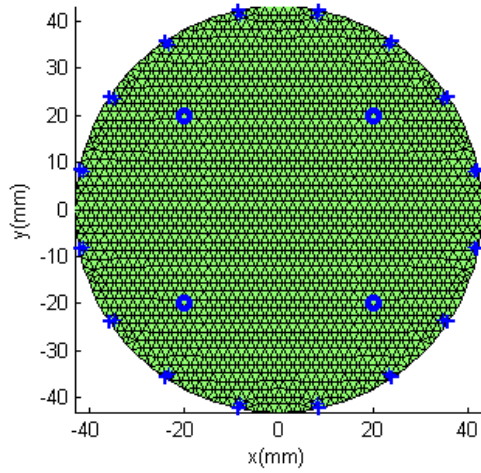
10

Fig. 2. Sample mesh and the source, detector, target positions

Fig. 3. Reconstructed absorption and scattering properties

used as the starting point. The optimization of the property is approached by minimizing the difference between the reconstructed forward model data and the original data. Maps of absorption and scattering properties are reconstructed simultaneously, as shown in Fig. 3. As shown in Fig. 3, all four targets are detected, and both absorption and scattering properties are reconstructed. The reconstructed target sizes are comparable to the actual ones. When no noise is added, the reconstructed optical properties of the large targets are close to the known values, while the properties of the small targets are not quite accurate. While 1% random noise was added, the sizes of the large targets are still close to actual values, and the error in reconstructed properties is about 20%. However, the small targets are hardly detected. The reconstruction result can be improved by changing conditions, such as, higher modulation frequency, more source-detector pairs etc.

Next we considered a *rectangular sample* of size 80 mm x 40 mm, with $\mu_a = 0.01$ mm^{-1}, $l_t = 1$ mm ($\mu_{s'} = 1$ mm^{-1}). 13 sources and 13 detectors are located on the entrance side and exit side, respectively. The sources are considered to be located 1 mm below the side, and used one at a time successively. Transmitted data are detected by 13 detectors for all 13 sources. In total, 169 source and detector pairs are used. One absorptive and one scattering circular targets are embedded. The center of the rectangle is set to be the origin of the coordinates. The position, property and size of the targets are listed in Table III.

Table III. Target position, property and size

Target#	Position (x, y) (mm)	μ_a (mm^{-1})	$\mu_{s'}$ (mm^{-1})	Radius (mm)
1	-10, 0	0.02	1	5
2	10, 0	0.01	2	5
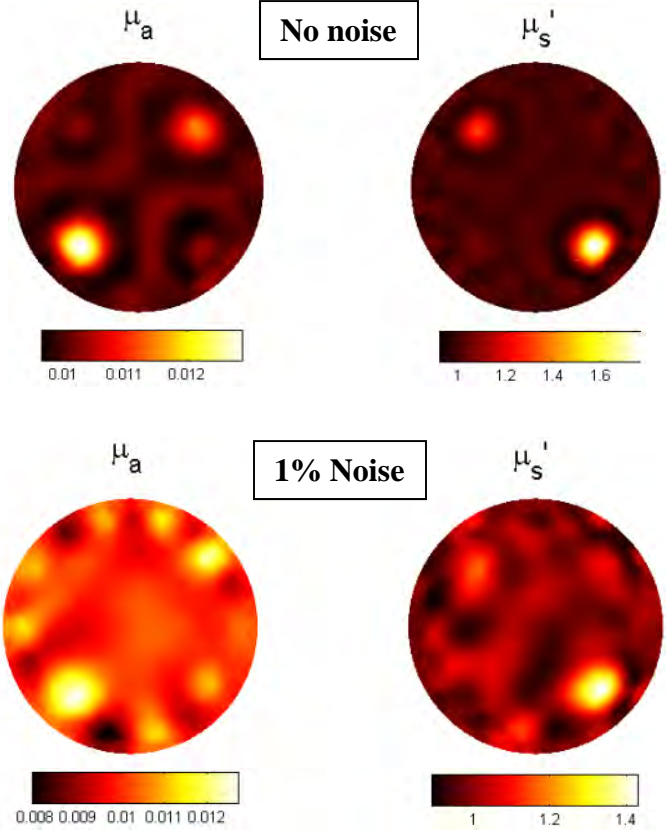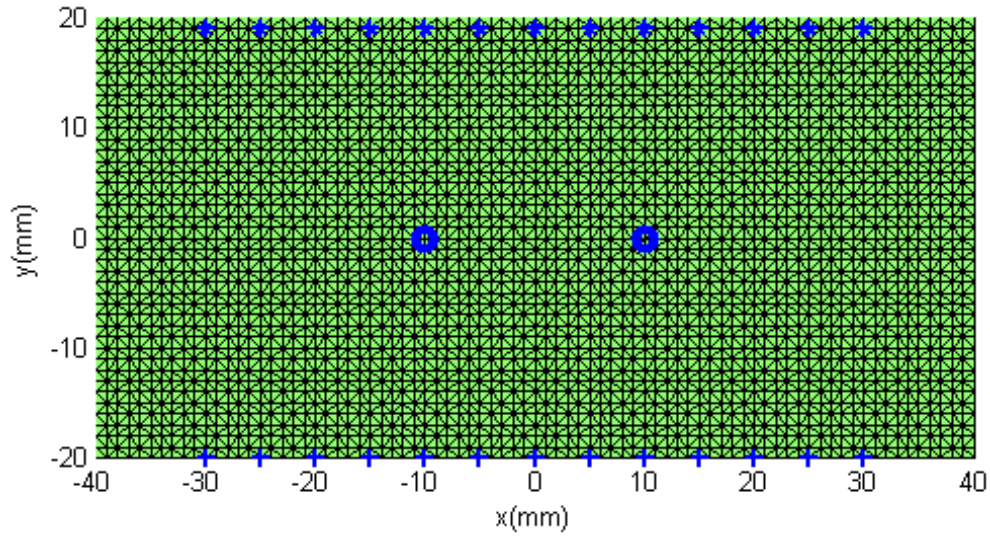
Fig. 4(a). Sample mesh and source/detector/target positions

The mesh of the sample with the source (*), detector (+) and target (o) positions is shown in Fig. 4(a). Frequency-domain data is generated with modulation frequency 100 MHz, and 1% random noise was added and compared to the situation with no noise.

NIRFAST was then run using the forward model data. The reconstructed images using the absorption and scattering property maps are shown in Fig. 4(b).

Fig.4(b). Reconstructed absorption and scattering properties

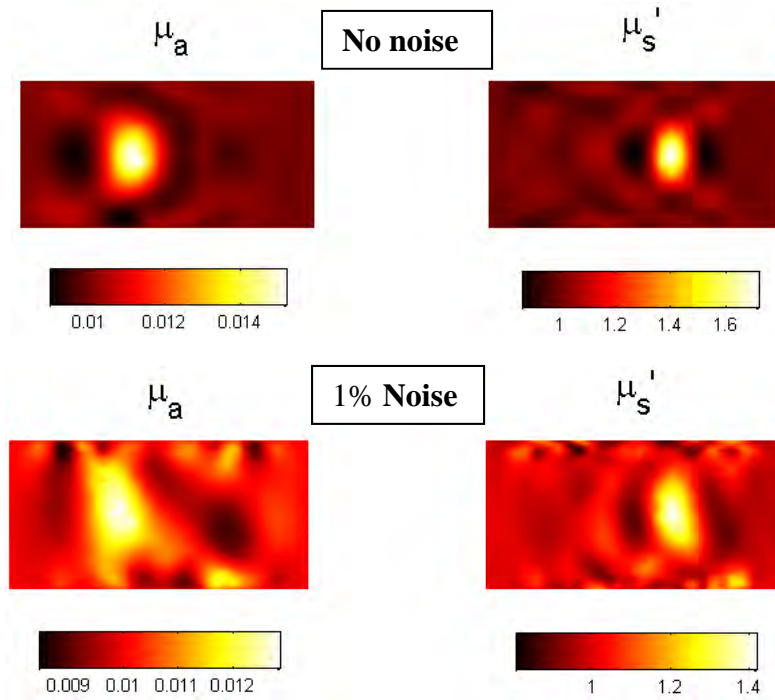As shown in Fig. 4(b), both absorptive and scattering targets were detected, and both absorption and scattering properties were reconstructed. The reconstructed target sizes are comparable to the actual sizes when no noise is added. While 1% random noise is present, the reconstructed size is larger. When no noise was added, the error in the reconstructed optical properties is about 25% for the absorptive target, and about 15% for the scattering target. When 1% random noise was added, the error in reconstructed properties is about 35% for the absorptive target, and about 30% for the scattering target.

Three-dimensional problems

Next we considered three-dimensional absorptive and scattering targets. The first sample was a cylinder of diameter 86 mm, and height 60 mm, $\mu_a = 0.01$ mm^{-1}, $l_t = 1$ mm ($\mu_{s'} = 1$ mm^{-1}). 240 source and detector pairs were used, and located in a manner similar to the 2-D circular problem discussed in the previous section in the cross-section of the middle plane (z = 0 mm) of the cylinder. One absorptive (scattering) spherical target was embedded at (x, y, z) = (20, 0, 0) mm. A discretized mesh of the cylindrical sample is shown in Fig. 5, along with the positions of the target (dark red), sources (green circle) and detectors (blue plus). Frequency-domain forward model data was generated with modulation frequency 100MHz and 1% random noise added compared with no noise present using NIRFAST, and then fed back into to reconstruct the absorption and scattering property maps of the sample.
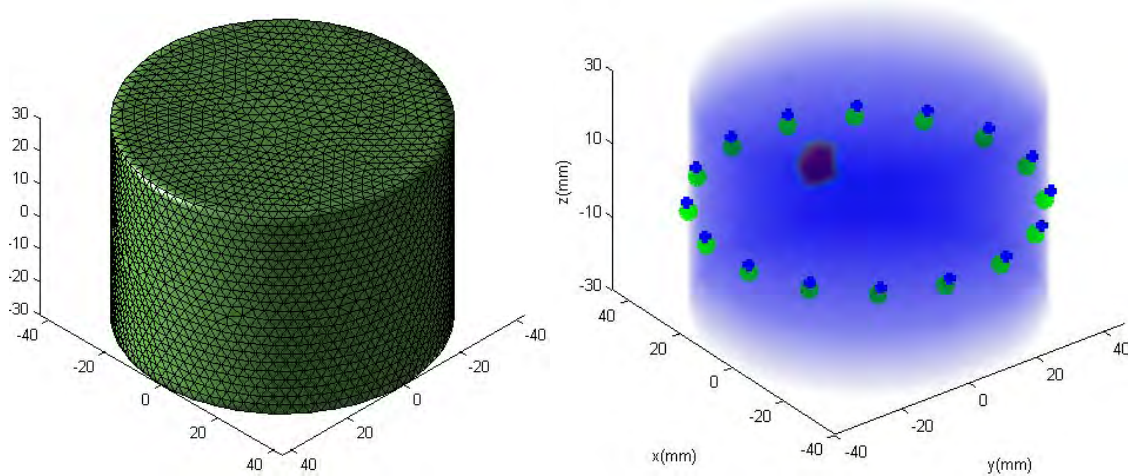
Fig.5. Sample mesh (left pane) and source/detector/target positions (right pane)

Absorptive target

An absorptive target is embedded, with $\mu_a = 0.1$ mm^{-1}, μ_s the same as background, and radius 5 mm. Reconstructed 3D image and a cross-section through the middle of the target are shown in Fig. 6(a) when there is no noise, and in Fig. 6(b) with 1% noise.

No noise:

μ_a

μ_a

μ_s'

Figure 6(a). Reconstructed images (absorption and scattering properties) of an absorptive target under no background noise condition: (top) 3-D distribution of absorption coefficient; (bottom left) absorption coefficient distribution, and (bottom right) reduced scattering coefficient distribution through the cylinder center (z = 0) plane.

1% noise:

$$\mu_a$$

$$\mu_a \qquad\qquad \mu_s{}'$$

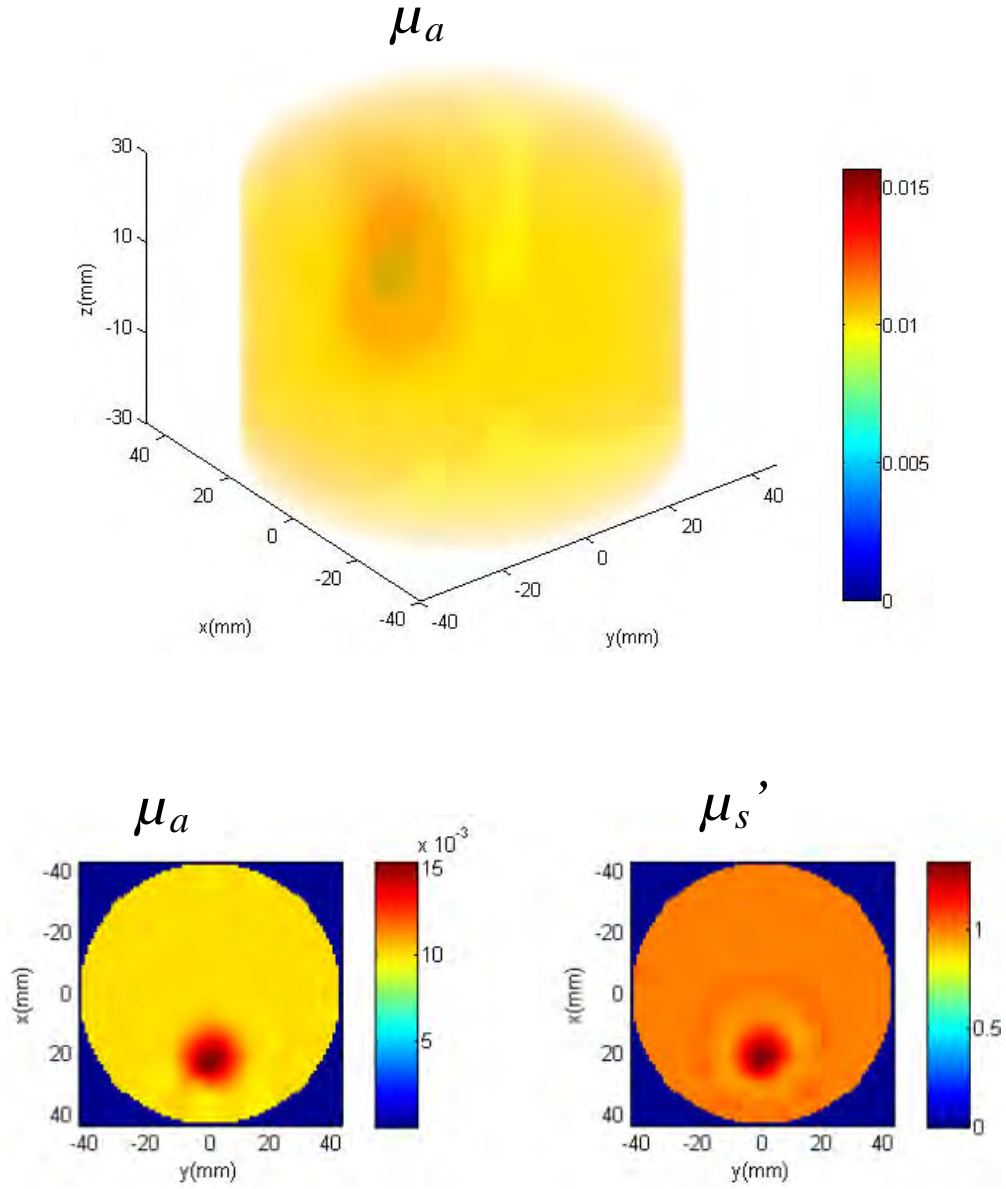Figure 6(b). Reconstructed images (absorption and scattering properties) of an absorptive target with 1% background noise: (top) 3-D distribution of absorption coefficient; (bottom left) absorption coefficient distribution, and (bottom right) reduced scattering coefficient distribution through the cylinder center (z = 0) plane.

Both absorptive and scattering properties are reconstructed simultaneously. Even though it is an absorptive target, and the scattering property of the target is the same as that of the background, the target is also seen in the reconstructed scattering property map. The reconstructed target size is comparable to the actual size in the lateral direction, while much bigger in the *z* direction for both no noise and 1% noise level cases. The reconstructed absorptive property of the target is about 15% of the actual value. The results can be improved by using higher modulation frequency, and more source-detector pairs etc.

Scattering target

A scattering target of radius 5 mm with $\mu_{s'} = 10$ mm^{-1}, and μ_a the same as background is embedded and radius 5 mm. The 3D absorption and scattering characteristics maps were reconstructed in a manner similarly to that used for the absorptive target.   The reconstructed 3D image and a cross-section through the middle of the target are shown in Fig. 7(a) when the background noise level is considered to be 0 and in Fig. 7(b) when 1% noise is assumed to be present.

No noise

Fig. 7(a). Reconstructed scattering and absorption properties of the single scattering target assuming 0 background noise (top) 3-D distribution of reduced scattering coefficient; (bottom left) absorption coefficient distribution, and (bottom right) reduced scattering coefficient distribution through the cylinder center ($z = 0$) plane.
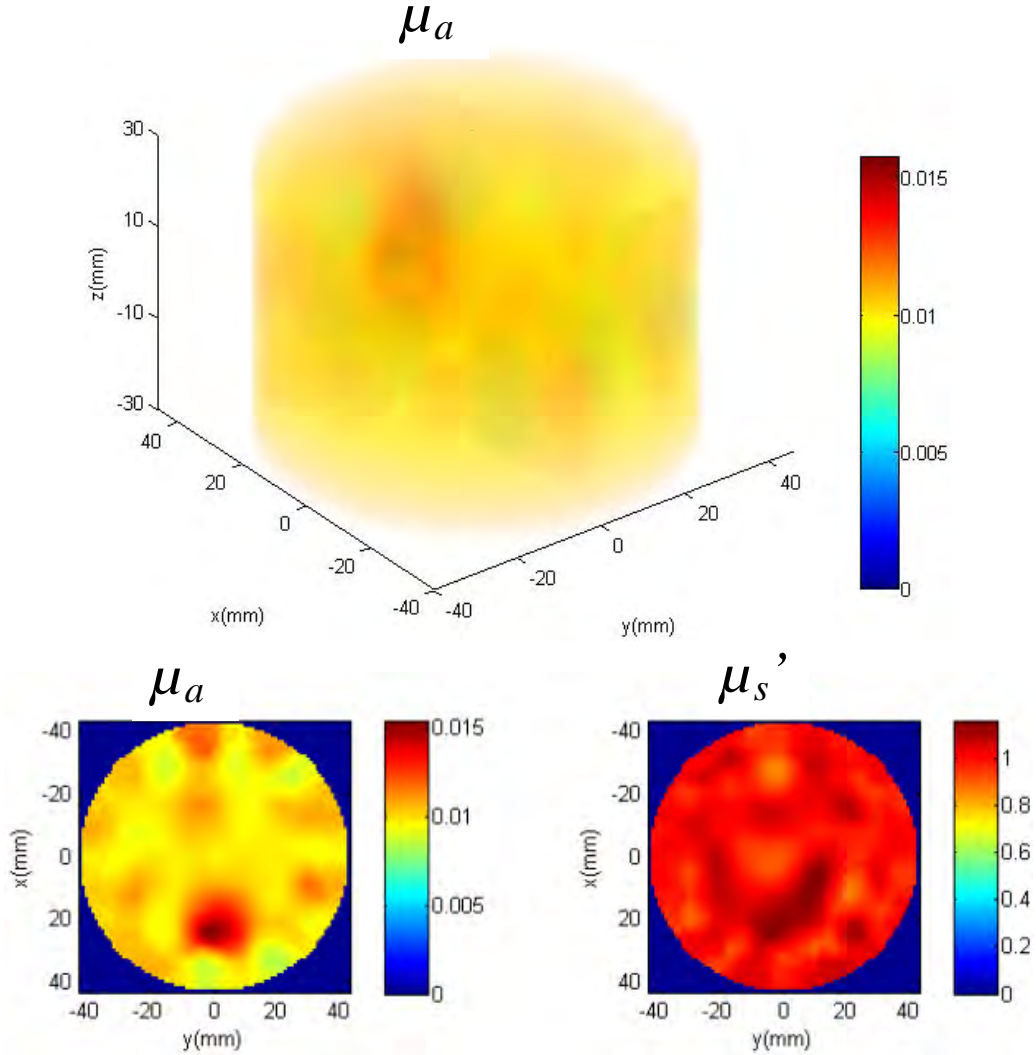
1% noise:

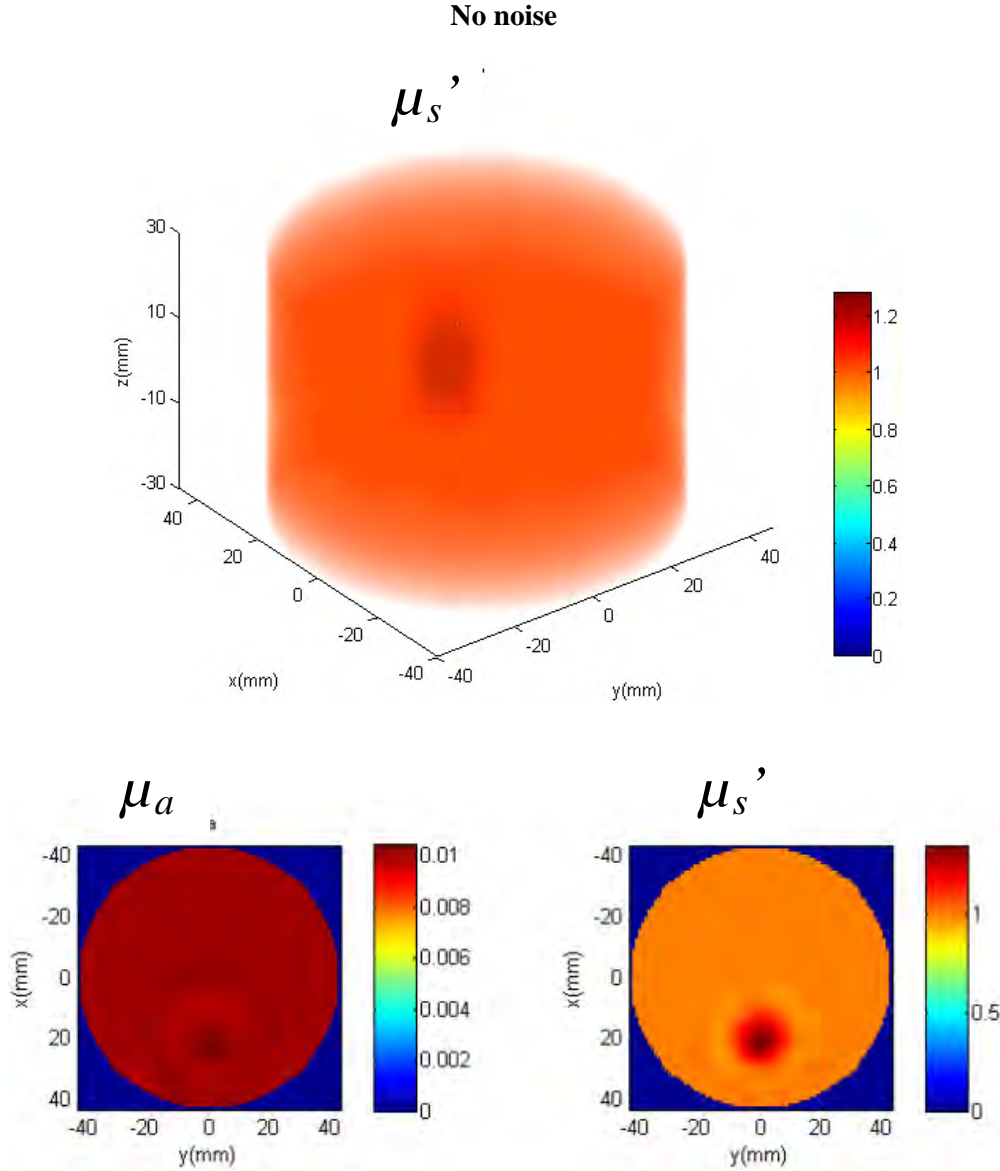$$\mu_s{}'$$

$$\mu_a$$

$$\mu_s{}'$$

Fig 7(b) Reconstructed scattering and absorption properties of the single scattering target assuming 1% background noise: (top) 3-*D* distribution of reduced scattering coefficient; (bottom left) absorption coefficient distribution, and (bottom right) reduced scattering coefficient distribution through the cylinder center (z = 0) plane.

Both absorptive and scattering properties were reconstructed simultaneously in this simulation. Even though it is a scattering target, it appears in the reconstructed absorption property map as well, especially for no-noise case. The reconstructed target size is comparable to the actual size in the lateral direction for both no noise and 1% noise level cases. The reconstructed scattering property of the target is about 11-12% of the actual value for no noise and 1% noise level cases.

Two targets

The next situation involved two absorptive spherical targets embedded at (-20, 0, 0) mm and (20, 0, 0) mm of the sample volume. Each of the spheres has a radius of 5 mm, $\mu_a = 0.1$ mm^{-1} and μ_s is the same as background. The cylinder mesh and the source/detector positions and background optical characteristics

of the sample are the same as in the single target case reported above. Frequency-domain data were generated with modulation frequency of 100 MHz. Figure 8(a) shows the reconstructed absorption and scattering coefficient maps of the target for 0 background noise, while Figure 8(b) shows those when 1% background noise is assumed. A cross-section image through the center of the cylinder is also shown.

No noise:

$$\mu_a$$

$$\mu_a \qquad\qquad \mu_s{}'$$

Fig. 8(a) Reconstructed scattering (and absorption) properties of the targets assuming 0 background noise: (top) 3-D distribution of absorption coefficient; (bottom left) absorption coefficient distribution, and (bottom right) scattering coefficient distribution through the cylinder center ($z = 0$) plane.
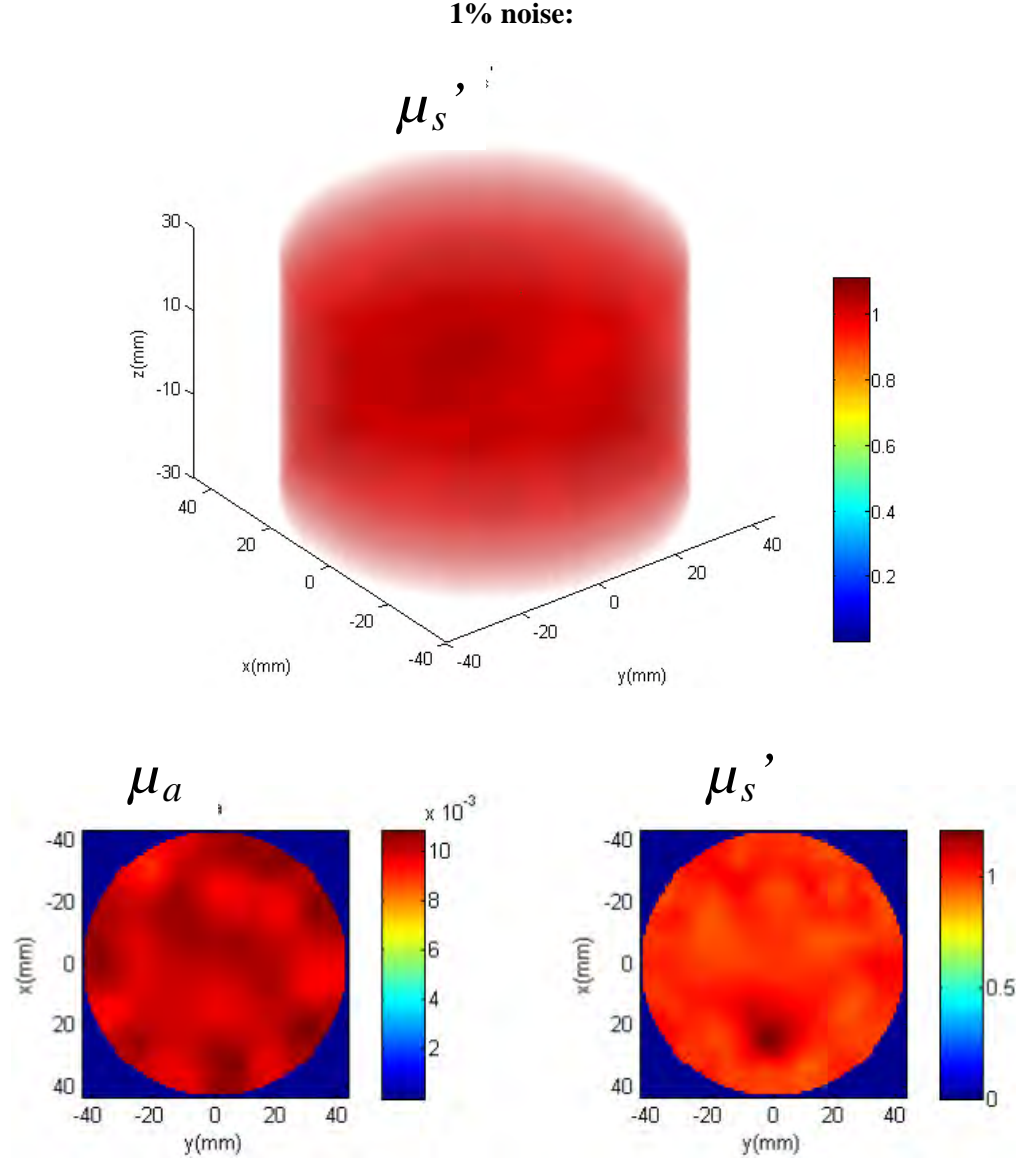
1% noise:

$$\mu_a$$
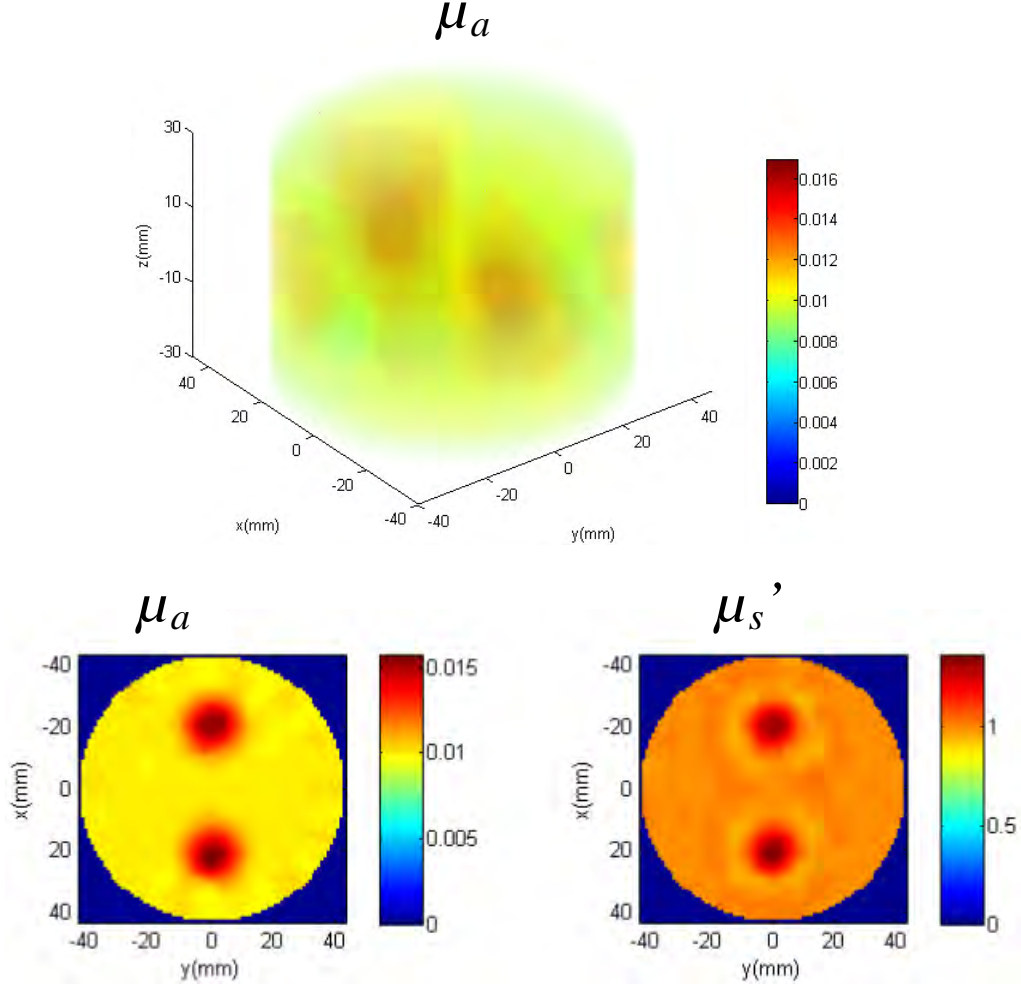

$$\mu_a \qquad\qquad \mu_s{'}$$
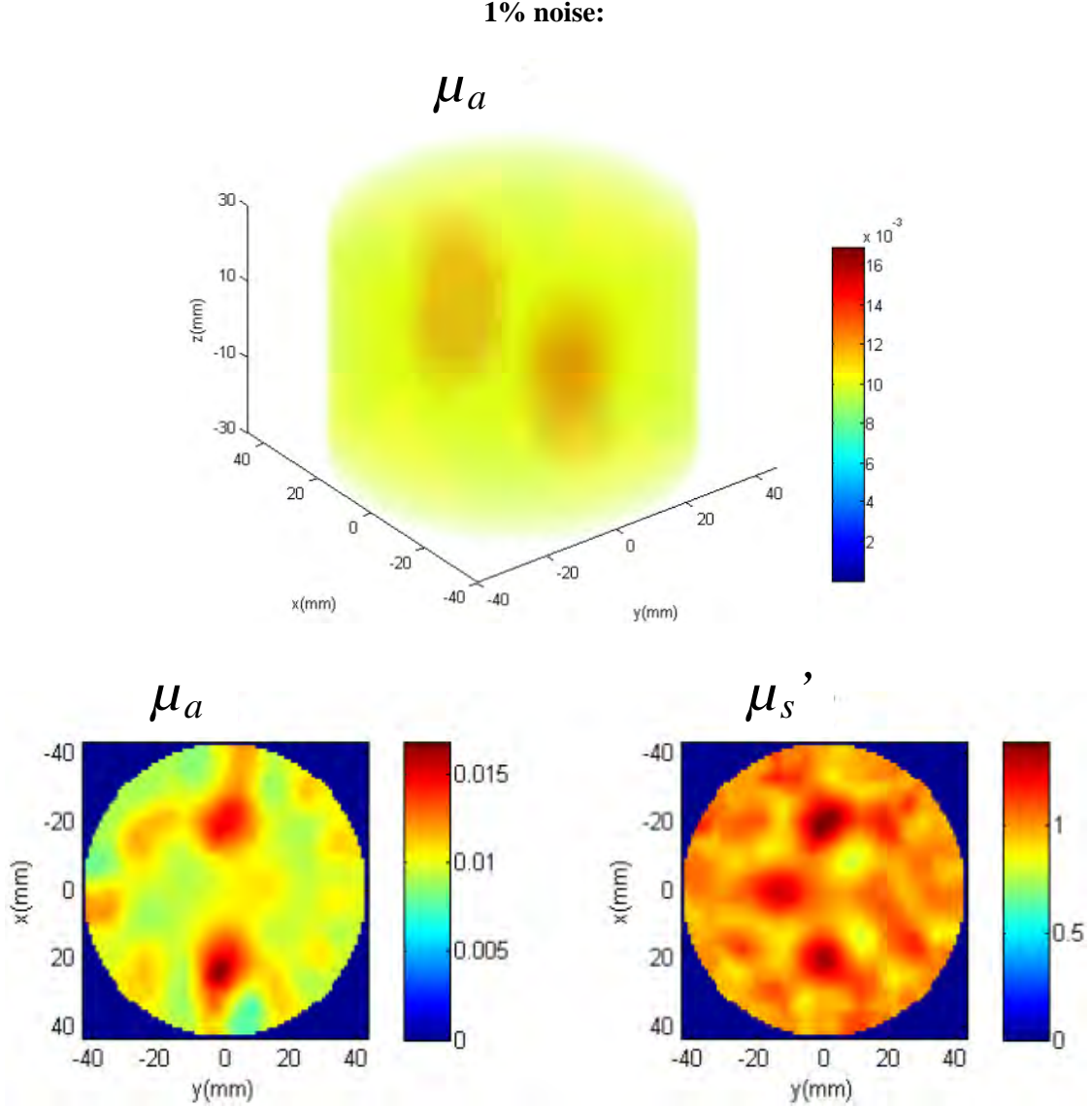
Fig. 8(b). Reconstructed scattering (and absorption) properties of the targets assuming 1% background noise: (top) 3-D distribution of absorption coefficient; (bottom left) absorption coefficient distribution, and (bottom right) scattering coefficient distribution through the cylinder center (z = 0) plane.

Overall, the target size can be reconstructed with values comparable to the actual value for both $2D$ and $3D$ cases. It is much more difficult to reconstruct optical property of the target(s) accurately. What is even more noteworthy is that even for an absorptive (scattering) target a reduced scattering (absorption) coefficient map was obtained in addition to the desired absorption (reduced scattering) coefficient map. This is not desirable and needs to be addressed. Higher modulation frequency and more source-detector pairs may be used to improve the results.

The program is now being tested for slab geometry which is used in our project. We plan to pursue the FEM approach further for $3D$ image reconstruction and estimation of target optical properties.

5.4 Magnetic Resonance Spectroscopic Imaging Training

The CCNY researchers pursued receiving training (*Specific Aim 0, Tasks 2, 3 and 5*) on magnetic resonance spectroscopic imaging (MRSI) in primary collaborating mentor (PCM) Dr. Koutcher's lab at MSKCC. The thrust of the effort was to adapt MRSI approach for detection of lactate, which is expected to provide a window to explore tumor aggressiveness (Specific Aim 1). Once MRSI is established as a reference technique, the aim is to develop optical spectroscopic techniques for lactate detection and validate the measurements against MRSI results. Since lactate level is associated with tumor aggressiveness, metastasis and treatment response [16], dependable and noninvasive means for detecting lactate in tumors is of immense interest.

Conventional MRSI is not adequate for effective lactate detection since the overlapping lipid and adjacent water signals obscure lactate signal. The double frequency-selective multiple quantum coherence transfer (SelMQC) technique shows promise to detect lactate [17], and the trainees got involved in developing instrumentation and testing those for lactate detection using phantom in Year 3 of the project. They pursued their training further during this reporting period. We plan to undertake correlated MRSI with SelMQC and optical spectroscopic measurements to investigate the glycolytic activity of tumors, and explore their potential for tumor aggressiveness assessment.

5.5 Research Proposal Development

One of the proposed tasks (*Specific Aim 0, Task# 7*) involves developing at least one research proposal and submitting it to NIH or USAMRMC for funding. We submitted a pre-proposal entitled, "*Multi-functional tumor-targeting nanocomposites and time-reversal optical imaging for early detection of breast cancer and prevention of micro-metastases*" to the Idea Award (Collaborative Option) category of the 2011 Breast Cancer Research Program of CDMRP. S. K. Gayen (PI of this proposal) is the Initiating PI of the above-mentioned proposal. The Collaborative PI is Valeria Balogh-Nair of the CCNY Chemistry Department. A brief overview of the pre-proposal follows:

    Research Idea

    The objective of the proposed research is to develop multi-functional, tumor-targeting nanocomposites and near-infrared (NIR) optical imaging approaches for early detection of breast cancer, and prevention of micro-metastases that are responsible for majority of breast cancer mortality. The nanocomposite synthesis will use a multivalent dendrimer (a class of organic macromolecules) platform to incorporate fluorescent moieties (e.g., semiconductor quantum dots, or gold/silver nanoparticles) as contrast agents for imaging, and chemokine mimics for selective targeting of cancer cells and prevention of metastases. The high affinity of chemokine mimic's ligands for chemokine CXCR4 receptors will ensure selective delivery of the nanocomposite to the target. A multi-source NIR probing and multi-detector signal acquisition arrangement along with a time-reversal image reconstruction algorithm will be used for fast detection of tumor and determination of its location in three dimensions.

Impact and Innovation

The major impact of the proposed research is that it has the potential to provide a modality for early detection of breast cancer, and for prevention of metastases, the major cause of mortality. A broader potential impact is that the approach could be extended to other cancers using chemokine mimics directed to other chemokine receptors.

The project is highly innovative in many ways. First, the synthesis process brings together the concept of multivalency, the idea of chemokine mimics for prevention of cancer cell migration, and use of dendrimers as stabilizers and nanoreactors for contrast agent synthesis. A combination of these novel ideas is proposed, to the best of our knowledge for the first time, as a multi-prong approach to fight the menace of breast cancer. Second, the affinity of the chemokine mimics to seven helix chemokine CXCR4 receptors obviates the need for a targeting vector. The chemokine mimics will play the dual role of: (1) "homing devices" for selective delivery of the nanocomposite to the tumor sites; and (2) "prevention agents" interacting with the chemokine receptor sites to inhibit metastases. Third, the efficacy of noninvasive NIR imaging approach for early detection and potential diagnosis will be significantly enhanced through design of efficient contrast agent. Fourth, the idea of time-reversal optical tomography (TROT) is a new paradigm in diffusive optical tomographic (DOT) imaging. While currently pursued DOT approaches are iterative and computation time intensive, TROT is non-iterative and will be faster, which is a necessary condition for real-time imaging. TROT is designed for detecting and locating small targets and will be suited for early detection when tumors are small. Finally, the dendrimer platform with multivalent surface will enable incorporation of moieties that enhance other imaging modalities, such as, magnetic resonance imaging, enabling development of sought-after dual or multimodal imaging modules.

6. KEY ACCOMPLISHMENTS

- Key research accomplishments include: (a) development of Time Reversal Optical Tomography (TROT) (which is fast and minimally iterative), and demonstration of its efficacy in detecting small targets in a tissue simulating turbid medium; (b) adaptation of decomposition methods, such as, Principal Component Analysis (PCA) and nonnegative matrix factorization (NMF) for study of the diffuse optical imaging problem and comparing those with previously developed OPTICA (optical tomography using Independent Component Analysis); (c) exploring lactate detection using magnetic resonance spectroscopic imaging as a potential method for assessing tumor aggressiveness; (d) publication of several papers and presentation of research results in major conferences including *Era of Hope* (2011) (detailed in Section 7 below); and (e) investigating finite element method with the aim of using it as a complement to TROT for retrieval of optical parameters at the localized target sites.

- The key training accomplishment includes the successful participation of physical scientists and engineers of CCNY research team in cancer biology research involving magnetic resonance spectroscopic imaging at the MRI research facility of MSKCC.

- Development and submission of an independent research pre-proposal to BCRP 2011 is indicative of the CCNY team's progress towards developing a sustainable breast cancer research program at CCNY.

7. REPORTABLE OUTCOMES

Publications

(1) B. Wu, W. Cai, M. Alrubaiee, M. Xu and S. K. Gayen, "*Three-dimensional time-reversal optical tomography*," in Multimodal Biomedical Imaging VI. Proceeding of SPIE, vol. 7892, pp. 78920G-1 – 78920G-6 (2011). (*Attached as Appendix* 1)

(2) M. Alrubaiee, B. Wu, M. Xu, W. Cai, and S. K. Gayen, "Multi-wavelength diffusive optical tomography using Independent Component Analysis and Time Reversal algorithms", in Diffuse Optical Imaging III Proceeding of SPIE-OSA, vol. 8088, pp. 80880Y-1 – 80880Y-5 (2011). (*Attached as Appendix* 2)

(3) Binlin Wu, M. Alrubaiee, W. Cai, M. Xu and S. K. Gayen, "Diffuse Optical Imaging using Decomposition Methods." *International Journal of Optics* (Accepted for publication) (*Attached as Appendix 3*)

(4) Binlin Wu, W. Cai, M. Alrubaiee, M. Xu, and S. K. Gayen, "Time reversal optical tomography: locating targets in a highly scattering turbid medium," *Opt. Express* **19**, 21956-21976 (2011). (*Attached as Appendix 4*)

Conference Presentations

(1) M. Alrubaiee, Binlin Wu, W. Cai, M. Xu and S. K. Gayen, "Multi-wavelength diffusive optical tomography using independent component analysis and time reversal algorithms." Paper 8088-33 presented at the SPIE/OSA European Conference on Biomedical Optics, 22-26 May, 2011, Munich, Germany.

(2) Binlin Wu, W. Cai, M. Alrubaiee, M. Xu and S. K. Gayen, "Three dimensional time reversal optical tomography," Paper 7892-15 presented at the SPIE's International Symposium on Biomedical Optics, BiOS '11/ Photonics West, 22-27 January, San Francisco, California.

(3) Binlin Wu, W. Cai, M. Alrubaiee, M. Xu, and S. K. Gayen, "Time reversal optical tomography for breast tumor detection", Paper BC060114-2962 presented at the 6th *Era of Hope* 2011 conference of Department of Defense (DOD) Breast Cancer Research Program (BCRP), 2 – 5 August, Orlando, Florida.

Research Proposal

(1) S. K. Gayen (Initiating PI), V. Balogh-Nair (Collaborating PI), "*Multi-functional tumor-targeting nanocomposites and time-reversal optical imaging for early detection of breast cancer and prevention of micro-metastases,*" submitted to the Idea Award (Collaborative Option) category of the 2011 Breast Cancer Research Program of CDMRP.

Research Personnel Development

Xiaohui Ni, a researcher trained and supported in part by this grant has moved to the Department of Chemistry and Chemical Biology of Harvard University as a research associate.

8. CONCLUSION

The work carried out during this reporting period: (a) culminated in CCNY research trainees' participation in magnetic resonance spectroscopic imaging breast cancer research at MSKCC;

and (b) shows the potential for noninvasive detection and three-dimensional localization of a tumor within a breast with significant accuracy. The contrast is based on the differences in the light scattering and absorption characteristics of the tumor and normal breast tissue.

"*So What Section*"

- The National Cancer Institute (NCI) has identified the development of imaging methodologies as an extraordinary opportunity for advancement in cancer research. Since the background of the CCNY team is in physical sciences and engineering, the training they received has provided them with necessary laboratory background in the biology of cancer research, and helping develop a knowledgeable multidisciplinary research force in the fight against breast cancer.

- A recent study involving 35,319 patients underscores the influence of primary tumor location on breast cancer prognosis [18], and makes it imperative that breast cancer detection modalities to obtain three-dimensional (3-D) location of the tumor relative to the axilla be developed. The optical imaging techniques (TROT, OPTICA and other decomposition methods) being developed are an important steps in obtaining 3-D location of a tumor within the breast. The methods are minimally iterative, fast, and designed for locating small targets, which make those suitable for detecting tumors in early stages of development when those are more amenable to treatment.

- The study involving lactate detection holds promise for tumor aggressiveness assessment.

9. REFERENCES

1. Annual Report Dated August 2008 covering the period 15 June 2007 – 14 June 2008, Award Number W81XWH-07-1-0454, on file at USAMRMC. (1)
2. Annual Report Dated August 2009 covering the period 15 June 2008 – 14 June 2009, Award Number W81XWH-07-1-0454, on file at USAMRMC.
3. Annual Report Dated September 2010 covering the period 15 June 2009 – 14 June 2010, Award Number W81XWH-07-1-0454, on file at USAMRMC. (3)
4. M. Xu, M. Alrubaiee, S. K. Gayen and R. R. Alfano, "Optical diffuse imaging of an ex vivo model cancerous human breast using independent component analysis," IEEE J. Select. Topics Quantum Electron. 14, 43 (2008).
5. J. F. Cardoso, "Blind signal separation: statistical principle," Proc IEEE **86**, 2009-2025 (1998).
6. I. T. Jolliffe, *Principal Component Analysis* (Springer, New York, 1986).
7. M. W. Berry, M. Browne, A. N. Langville, V. P. Pauca, and R. J. Plemmons, "Algorithms and applications for approximate nonnegative matrix factorization," Comp. Stat. Data Anal. **52**, 155-173 (2007).
8. H. J. van Staveren, C. J. M. Moes, J. van Marle, S. A. Prahl, and M. J. C. van Gemert, "Light scattering in Intralipid-10% in the wavelength range of 400--1100 nm," Appl. Opt. **31**, 4507-4514 (1991).
9. C. Bordier, C. Andraud, J. Lafait, E. Charron, M. Anastasiadou, and A. de Martino, "Illustration of a bimodal system in Intralipid 20% by polarized light scattering: experiments and modelling," Appl. Phys. A **94**, 347-355 (2009).
10. M. Fink, D. Cassereau, A. Derode, C. Prada, P. Roux, M. Tanter, J. L. Thomas, and F. Wu, "Time-reversed acoustics," Rep. Prog. Phys. **63**(12), 1933–1995 (2000).

11. A. J. Devaney, E. A. Marengo, and F. K. Gruber, "Time-reversal-based imaging and inverse scattering of multiply scattering point targets," J. Acoust. Soc. Am. **118**(5), 3129–3138 (2005).
12. S. K. Lehman and A. J. Devaney, "Transmission mode time-reversal super-resolution imaging," J. Acoust. Soc. Am. 113(5), 2742–2753 (2003).
13. S. R. Arridge and M. Schweiger, "Photon measurement density functions. Part 2: Finite element calculations", Appl. Opt. 34, 8026 (1995), and references therein.
14. Website address: http://www.dartmouth.edu/~nir/nirfast/
15. Michael S. Patterson, B. Chance, and B. C. Wilson, "Time resolved reflectance and transmittance for the non-invasive measurement of tissue optical properties," Appl. Opt. 28, 2331-2336 (1989).
16. A. Le, C. R. Cooper, A. M. Gouw, R. Dinavahi, A. Maitra, L. M. Deck, R. E. Royer, J. D. L. Vander, G. L. Semenza, C. V. Dang, "Inhibition of lactate dehydrogenase A induces oxidative stress and inhibits tumor progression," Proc. Natl. Acad. Sci. USA 107, 2037 (2010).
17. M. Muruganandham, J. A. Koutcher, G. Pizzorno, and Q. He, "*In vivo* tumor lactate relaxation measurements by selective multiple-quantum-coherence (Sel-MQC) transfer," Magn. Reson. Med. 52, 902 (2004).
18. 16. N. Kroman, J. Wohlfahrt, H. T. Mouridsen, and M. Melbye, "Influence of tumor location on breast cancer prognosis," Int. J. Cancer 105, 542 -545 (2003).

10. APPENDICES

Appendix 1. A *reprint* of: B. Wu, W. Cai, M. Alrubaiee, M. Xu and S. K. Gayen, "*Three-dimensional time-reversal optical tomography*," in Multimodal Biomedical Imaging VI. Proceeding of SPIE, vol. 7892, pp. 78920G-1 – 78920G-6 (2011).

Appendix 2. A reprint of: M. Alrubaiee, B. Wu, M. Xu, W. Cai, and S. K. Gayen, "*Multi-wavelength diffusive optical tomography using Independent Component Analysis and Time Reversal algorithms,*" in Diffuse Optical Imaging III Proceeding of SPIE-OSA, vol. 8088, pp. 80880Y-1 – 80880Y-5 (2011).

Appendix 3. A pre-print of an in-press article: Binlin Wu, M. Alrubaiee, W. Cai, M. Xu and S. K. Gayen, "*Diffuse Optical Imaging using Decomposition Methods.*" International Journal of Optics (Accepted for publication)

Appendix 4. Binlin Wu, W. Cai, M. Alrubaiee, M. Xu, and S. K. Gayen, "*Time reversal optical tomography: locating targets in a highly scattering turbid medium,*" Opt. Express 19, 21956-21976 (2011).

Appendix 5. A copy of the technical abstract of a proposal: S. K. Gayen (Initiating PI), V. Balogh-Nair (Collaborating PI), "*Multi-functional tumor-targeting nanocomposites and time-reversal optical imaging for early detection of breast cancer and prevention of micro-metastases,*" submitted to the Idea Award (Collaborative Option) category of the 2011 Breast Cancer Research Program of CDMRP.

Three dimensional time reversal optical tomography

Binlin Wu*[a], W. Cai[a], M. Alrubaiee[a], M. Xu[b] and S. K. Gayen[a]

[a]The City College and the Graduate Centre of The City University of New York, New York, NY, USA 10031;

[b]Physics Department, Fairfield University, Fairfield, CT, USA 06824

ABSTRACT

Time reversal optical tomography (TROT) approach is used to detect and locate absorptive targets embedded in a highly scattering turbid medium to assess its potential in breast cancer detection. TROT experimental arrangement uses multi-source probing and multi-detector signal acquisition and Multiple-Signal-Classification (MUSIC) algorithm for target location retrieval. Light transport from multiple sources through the intervening medium with embedded targets to the detectors is represented by a response matrix constructed using experimental data. A TR matrix is formed by multiplying the response matrix by its transpose. The eigenvectors with leading non-zero eigenvalues of the TR matrix correspond to embedded objects.

The approach was used to: (a) obtain the location and spatial resolution of an absorptive target as a function of its axial position between the source and detector planes; and (b) study variation in spatial resolution of two targets at the same axial position but different lateral positions. The target(s) were glass sphere(s) of diameter ~9 mm filled with ink (absorber) embedded in a 60 mm-thick slab of Intralipid-20% suspension in water with an absorption coefficient μ_a ~ 0.003 mm^{-1} and a transport mean free path l_t ~ 1 mm at 790 nm, which emulate the average values of those parameters for human breast tissue. The spatial resolution and accuracy of target location depended on axial position, and target contrast relative to the background. Both the targets could be resolved and located even when they were only 4-mm apart. The TROT approach is fast, accurate, and has the potential to be useful in breast cancer detection and localization.

Keywords: Time reversal, MUSIC, diffusive optical imaging, optical tomography, biomedical imaging, breast cancer imaging, scattering medium, diffusion approximation

1. INTRODUCTION

Optical imaging of targets embedded in turbid media, such as a tumor in a breast, has attracted much attention in the last two decades. When a beam of light propagates through a highly scattering medium, photons are scattered and diffused into a broad area; phase coherence and polarization of light deteriorate; short pulses broaden; and consequently sharp images of the targets cannot be formed directly. Various algorithms have been developed to perform image reconstruction[1-4]. Inverse image reconstruction (IIR) is an ill-posed problem and search of reliable and fast approaches is an important and formidable task for optical imaging of human tissue such as breast. Recent inverse algorithms, such as Newton-Raphson-Marquart algorithms[5] and direct linear inversion of 3-D matrices[6], are time consuming. The iterative methods[6, 7] may not ensure that the obtained result arrives at a "global minimum" or converge to a "local minimum".

Time reversal optical tomography (TROT)[9,10] was introduced as a reconstruction method for imaging targets in turbid media non-invasively using light, following the development of TR imaging using multistatic radar signal[8]. Compared to other inverse methods which usually require iterations[4], TROT is fast since there is no iteration involved. The signals and noise are separated into orthogonal subspaces. A method similar to L-curve regularization is used to select the signal subspace. Then a pseudo spectrum is calculated directly for all voxels in the sample using the vector subspace method, MUltiple SIgnal Classification (MUSIC)[8-10]. Tomographic pseudo images can be generated using pseudo values. Locations and characteristics of targets are determined by the global maximum (or local maximum in low signal-to-noise (SNR) cases) components in the pseudo spectrum.

*bwu@sci.ccny.cuny.edu; phone 1 212 650-5556

This paper is organized as follows. In section 2, the formalism of the TROT approach is presented. In section 3, the experimental arrangement, materials and parameters are described. In section 4, the TROT analysis on the experimental data and results are presented. Section 5 serves as discussion and summary.

2. FORMALISM

Using diffusion approximation of the radiative transfer equation (RTE), the scattered light due to small weak inhomogeneities (targets) embedded in a homogeneous medium to the first order Born approximation can be written as[4]

$$\phi_{sca}(\boldsymbol{r}_d, \boldsymbol{r}_s) = -\int G(\boldsymbol{r}_d, \boldsymbol{r})\delta\mu_a(\boldsymbol{r})cG(\boldsymbol{r}, \boldsymbol{r}_s)d^3\boldsymbol{r} - \int \delta D(\boldsymbol{r})c\nabla_r G(\boldsymbol{r}_d, \boldsymbol{r}) \cdot \nabla_r G(\boldsymbol{r}, \boldsymbol{r}_s)d^3\boldsymbol{r} \ , \tag{1}$$

where $\boldsymbol{r}_s$, $\boldsymbol{r}_d$, and $\boldsymbol{r}$ are the positions of a point-like source of unit power, detector and target, respectively; $G(\boldsymbol{r}, \boldsymbol{r}_s)$ and $G(\boldsymbol{r}_d, \boldsymbol{r})$ are the Green functions that describe light propagations from the source to the target and from the target to the detector, respectively; $\delta\mu_a$ and δD describe the differences of absorption and scattering properties between the targets and the background medium, respectively; and c is the light speed in the medium. For an absorptive target, a matrix form of the response matrix K is constructed as $\{K_{ij}\} = \{\sum_{m=1}^{M} G^d(\boldsymbol{r}_i, \boldsymbol{X}_m)\tau_m G^s(\boldsymbol{X}_m, \boldsymbol{r}_j)\}$, ($i = 1,2, \cdots N_d$; $j = 1,2, \cdots, N_s$), where $\boldsymbol{r}_i$, $\boldsymbol{r}_j$ and $\boldsymbol{X}_m$ are locations of the ith detector, j^{th} source and m^{th} target, respectively; N_s, N_d and M are the numbers of sources, detectors and targets, respectively. It is assumed the number of targets is less than the number of sources and detectors, $M < min(N_d, N_s)$.

A multi-source interrogation and multi-detector acquisition scheme is used to acquire multistatic transillumination data, from which the scattered light due to the targets is found, $\phi_{sca} = \phi - \phi_0$, where ϕ is the light intensity measured on the boundary with targets embedded in the scattering medium and ϕ_0 is the background image without targets embedded, which can be approximated by an "average" of all acquired images. Thus, the response matrix K is constructed with perturbations of spatial intensity distributions on the boundary.[11]

A time reversal matrix T is then constructed as $T = KK^\dagger$ (or $T = KK^T$ for continuous wave (CW)), which is similar to the time reversal matrix used in the time reversal by Devaney[8-11]. Eigenvalues λ_j and eigenvectors u_j of T are found, where $j = 1,2, \cdots min(N_d, N_s)$. The leading eigenvalues correspond to the targets. The vector subspace method, MUSIC is used to determine the locations of hidden objects. A Green's function vector on the detector array $g_d(\boldsymbol{X}_p)$ associated with a test target position $\boldsymbol{X}_p$ at p^{th} voxel is calculated using diffusion model, where $g_d(\boldsymbol{X}_p) = [G^d(\boldsymbol{r}_1, \boldsymbol{X}_p), G^d(\boldsymbol{r}_2, \boldsymbol{X}_p), \cdots, G^d(\boldsymbol{r}_{N_d}, \boldsymbol{X}_p)]^T$ and the Green's functions $G^d(\boldsymbol{r}_j, \boldsymbol{X}_p)$, $j = 1,2, \cdots N_d$, describe light propagation from the test target position $\boldsymbol{X}_p$ to detectors at $\boldsymbol{r}_j$. Then the eigenvectors u_j corresponding to the leading eigenvalues are used to calculate the MUSIC type pseudo spectrum using the following formula[8,9]:

$$P(\boldsymbol{X}_p) = \frac{|g_d(\boldsymbol{X}_p)|^2}{\left||g_d(\boldsymbol{X}_p)|^2 - \sum_{\lambda_j \le \epsilon}|u_j^\dagger g_d(\boldsymbol{X}_p)|^2\right|}, \tag{2}$$

where ϵ is the threshold determined using an L-curve method to separate the signal and noise subspaces. When both absorption and scattering properties are considered[12], one Green's function vector associated with absorption property and constructed with Green's functions G^d and three Green's function vectors associated with scattering property constructed with $\partial G^d/\partial x$, $\partial G^d/\partial y$ and $\partial G^d/\partial z$, respectively are used to calculate the pseudo spectrum at each voxel. Hence, four pseudo values are obtained at each voxel, one for absorption, and three for scattering.

A maximum value of $P(\boldsymbol{X}_p)$ is obtained when $\boldsymbol{X}_p$ is the position of one of the hidden objects. By sorting pseudo values $P(\boldsymbol{X}_p)$, the positions of the embedded objects are determined. At the same time, absorptive and scattering objects are distinguished according to the type of the Green's function vector $g_d(\boldsymbol{X}_p)$ associated with maximum pseudo value.

In this MUSIC procedure, only a single run for calculating the pseudo spectrum over voxels is required, without iterative procedure used in the traditional inverse approach.

3. EXPERIMENTAL METHODS AND MATERIALS

Two different samples were used to test the efficacy of the TROT approach in two different experiments. Both samples used a 250 mm × 250 mm × 60 mm transparent plastic container filled with Intralipid-20% suspension in water. The concentration of Intralipid-20% was adjusted to provide an absorption coefficient $\mu_a \sim 0.003$ mm^{-1} at 790 nm, and a transport mean free path $l_t \sim 1$ mm, which were similar to values of those parameters for human breast tissue. In the first sample, the depth (position along z-axis) of an absorptive target was varied to explore how the accuracy of position estimate depended on depth. In the second sample, the separation between two absorptive targets was varied to test how close those could be and yet be resolved as separate objects. The target(s) were glass sphere(s) of diameter 8-9 mm filled with ink dissolved in Intralipid suspension in water (μ_s was adjusted to be the same as that of the background medium, μ_a =0.013 mm^{-1} which was about 3 times higher than that of background medium).

A multi-source interrogation and multi-detector acquisition scheme was used to acquire data. A 100-mW 790-nm diode laser beam was used to illuminate the samples and scan the source plane with a 5 mm step-size. A charge coupled device (CCD) camera was used on the other side of the sample to detect the transmitted light on the boundaries of the slab samples (detector plane). The first sample was scanned with the laser beam in an array of 9×9 grid points, and the second sample was scanned in an array of 11×15 grid points. The scanning and acquisition process was controlled by a computer (PC). A schematic diagram of the experimental setup is shown in Fig. 1.
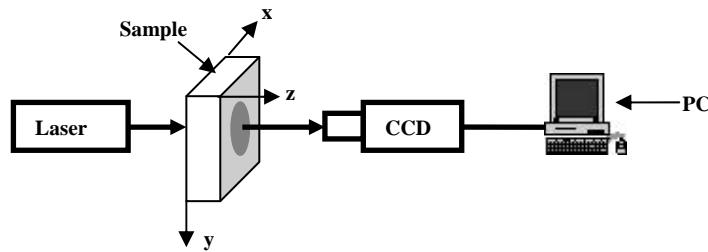

Fig. 1. A schematic diagram of the experimental arrangement used for imaging objects embedded in a turbid medium.

4. ANALYSIS AND RESULTS

One whole dataset for each experiment is of order 10^8 source-detector pairs, considering each pixel in a CCD camera as a detector. From each image, a region of interest was cropped out and then every 5×5 pixels in the cropped image were binned to one pixel. Light intensity perturbation due to targets in each image was found by subtracting the background image from each individual image. The response matrix was constructed using the light intensity perturbations. The TR matrix was generated by multiplying the response matrix by its adjoint matrix (transpose for continuous-wave (CW) illumination). The eigenvalue equation was solved and signal subspace was selected and separated from the noise subspace. MUSIC was then used to calculate the pseudo spectrum for every voxel in the 3D space of the sample. For each voxel, one absorption and three scattering components were calculated. The voxel size was 0.77 mm × 0.77 mm × 1 mm. By sorting the pseudo spectrum, the object(s) were located.

In the first experiment using only one target, the lateral (x, y) position of the target was kept the same at (25.5 mm, 24.7 mm), while five different depths (position along z-axis) of 15 mm, 20 mm, 25 mm, 30 mm, 35 mm, 40 mm and 45 mm were used. A cross-sectional pseudo image was generated using the pseudo spectrum for all voxel positions in the sample. The spatial profiles in the x, y and z directions of the images through the targets (a typical image and profiles for the two-target case are shown in Fig. 2) are used to assess target location. The retrieved target positions are compared with known positions in Table 1.

Table 1. Positions of one target located at different depths

Known Positions $[x, y, z$ (mm)]	Retrieved Positions $[x, y, z$ (mm)]	Error (mm)
25.5, 24.7, 15	24.9, 24.4, 17.5	0.6, 0.3, 2.5
25.5, 24.7, 20	25.7, 24.4, 21.5	0.2, 0.3, 1.5
25.5, 24.7, 25	25.7, 24.4, 26.5	0.2, 0.3, 1.5
25.5, 24.7, 30	25.7, 24.4, 30.5	0.2, 0.3, 0.5
25.5, 24.7, 35	25.7, 25.2, 33.5	0.2, 0.5, 1.5
25.5, 24.7, 40	24.9, 25.2, 36.5	0.6, 0.5, 3.5
25.5, 24.7, 45	24.9, 25.2, 39.5	0.6, 0.5, 5.5

The TROT assessed positions were in good agreement with the known positions. The accuracy of the z-position was found to be optimal when the target was located in the middle plane of the sample, and deteriorated when the target was closer to the source plane or the image plane.

In the second experiment using two targets the depth was kept fixed ($z = 30$ mm), while the separation between them separated with distances of ~ 11.8 mm, 16.8 mm, and 26.8 mm, in the x direction. A cross-sectional pseudo image of the targets when separated by a center-to-center distance of 11.8 mm (separation between nearest edges ~4 mm), generated using the pseudo spectrum are shown in the left pane of Fig. 2. Similar images for other target separations were also obtained. The profiles in the x, y and z directions through the right target are shown in the right pane of Fig. 2. These profiles were used to assess locations of the targets, and the separation between the two targets. In all cases, the targets were determined to be absorptive, because peaks occurred in the pseudo spectrum with the test Green's function vector corresponding to absorption property.
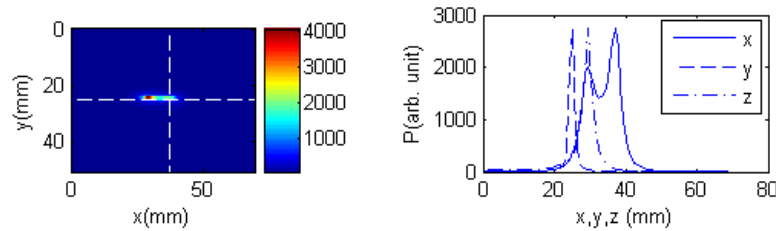

Fig. 2. TROT generated cross-section pseudo image when the targets are separated by 11.8 mm is shown in the left pane and pseudo-value profiles through the target along x, y and z directions are shown in the right pane.

The known and retrieved positions and separations Δx between of the two targets appear in Table 2. In all the cases, the two targets were resolved, even when their center-to-center separation was 11.8 mm apart, nearest sides separated by only ~4 mm. For all retrieved positions, the maximum error in the lateral positions is 3.0 mm, and the maximum error in the axial positions is 1.5 mm. The errors in the lateral positions increase as the targets get closer.

Table 2. Positions of two targets separated with different distances

Known Separation [Δx (mm)]	Obj. #	Known Position [x, y, z (mm)]	Retrieved Position [x, y, z (mm)]	Error (mm)	Retrieved Separation [Δx (mm)]
11.8	1	27.6, 26.0, 30	30.3, 24.4, 28.5	2.7, 1.6, 1.5	6.9
	2	40.2, 26.0, 30	37.2, 25.2, 29.5	3.0, 0.8, 0.5	
16.8	1	25.1, 26.0, 30	26.4, 24.4, 28.5	1.3, 1.6, 1.5	14.6
	2	42.7, 26.0, 30	41.0, 25.2, 29.5	1.7, 0.8, 0.5	
26.8	1	20.1, 26.0, 30	19.5, 25.2, 29.5	0.6, 0.8, 0.5	27.6
	2	47.7, 26.0, 30	47.1, 25.2, 30.5	0.6, 0.8, 0.5	

Similar experiments were also done when the target had a higher concentration of ink corresponding to a greater absorption coefficient. In that case, smaller errors occurred in the retrieved position which should be due to higher signal-to-noise ratio.

5. SUMMARY AND DISCUSSIONS

The work presented above demonstrate that TROT is effective in obtaining three-dimensional location information of a single absorptive target at different axial locations, and two absorptive targets separated by different distances along a lateral direction. The known lateral positions of the targets were retrieved within ~2 mm for breast tissue simulating samples. The accuracy for assessing the axial position (depth) depended on the target location. High accuracy was obtained for target in the mid-plane, while the accuracy deteriorated as the target was moved towards the source plane or the detector plane. Breast tumors commonly grow further from the breast surface, and the TROT approach is expected to be effective in locating those even at an early stage.

The experiments presented in this article were carried out for samples in slab geometry. The approach can be adapted to cylindrical geometry as well. While the results presented here are for absorptive target(s), our preliminary work show that TROT will be effective for scattering targets as well, and we are in the process of developing it for scattering targets, as well as, for targets that are both scattering and absorptive in nature. Our experiments used continuous-wave light, but the approach would work with frequency domain and time-resolved data as well.

One important difference between the sample used in our experiments and human breast is that in our sample the intervening medium can be treated as uniform, while human breast is not uniform. The pseudo spectrum is calculated using the known Green's function of the background medium. When the medium is non-uniform, Green's function for a uniform medium is used as an approximation.[13]

The approach is fast as no iteration is involved. The code used to perform the computation is written in Matlab. With pre-processed data, a typical time to perform the 3D image reconstruction (5 cm $\times$ 5 cm $\times$ 6 cm) with a sub-millimeter resolution using a Pentium 2GHz CPU processor and 2GB memory, is approximately 10 minutes. The computation time can be further reduced by improving our algorithm, and using C/C++ code.

In summary, the TROT approach based on the concept of time reversal and using MUSIC shows promise to locate objects in turbid media, such as a tumor in human breast with useful accuracy.

REFERENCES

[1] O'Leary, M. A., Boas, D. A., Chance, B. and Yodh, A. G., "Experimental images of heterogeneous turbid media by frequency-domain diffusing-photon tomography," Opt. Lett. 20, 426-428 (1995).

[2] Pogue, B. W., Testorf, M., McBride, T., Osterberg, U. and Paulsen, K. D., "Instrumentation and design of a frequency-domain diffuse optical tomography imager for breast cancer detection," Opt. Express 1, 391-403 (1997)

[3] Cai, W., Gayen, S. K., Xu, M., Zevallos, M., Alrubaiee, M., Lax, M. and Alfano, R. R., "Optical tomographic image reconstruction from ultrafast time-sliced transmission measurements," Appl. Opt. 38, 4237– 4246 (1999).

[4] Arridge, S. R. and Schotland, J. C., "Optical Tomography: forward and inverse problems," Inverse Probl., 25(12), 123010 (2009).

[5] Brooksby, B. A., Dehghani, H., Pogue, B. W. and Paulsen, K. D., "Near-Infrared (NIR) Tomography Breast Image Reconstruction with A Priori Structural Information From MRI: Algorithm Development for Reconstructing Heterogeneities," IEEE J. Sel. Top. Quantum Electron. 9, 199-209 (2003).

[6] Tao, Y., Wang, Y., Pei, Y., Zhu, W. and Barbour, R. L., "Frequency-domain optical imaging of absorption and scattering distributions by a Born iterative method," J. Opt. Soc. Am. A. 14, 325-342 (1997).

[7] Arridge, S. R., Schweiger, M., Hiraoka, M. and Delpy, D. T., "A Finite Element approach to modeling photon transport in tissue," Med. Phys. 20, 299-309 (1993).

[8] Devaney, A. J., "Time reversal imaging of obscured targets from multistatic data," IEEE Trans. Antenn. Propag. 53, 1600-1610 (2005).

[9] Cai, W., Alrubaiee, M., Gayen, S. K., Xu, M. and Alfano, R. R., "Three-dimensional optical tomography of objects in turbid media using the round-trip matrix, " Proc. SPIE 5693, 4 (2005).

[10] Wu, B., Alrubaiee, M., Cai, W., Xu, M. and Gayen, S. K., "Optical Imaging of Objects in Turbid Media Using Principal Component Analysis and Time Reversal Matrix Methods," in Computational Optical Sensing and Imaging, OSA Technical Digest (CD), paper JTuC10 (2009).

[11] Lehman, S. K. and Devaney, A. J., "Transmission mode time-reversal super-resolution imaging," J. Acoust. Soc. Am. 113, 2742-2753 (2003).

[12] Xu, M., Alrubaiee, M., Gayen, S. K. and Alfano, R. R., "Optical imaging of turbid media using independent component analysis: Theory and simulation," J. Biomed. Opt. 10 (5), 051705 (2005).

[13] Borcea, L., Papanicolaou, G. C., Tsogka, C. and Berryman, J., "Imaging and time reversal in random media," Inverse Probl., 18(5), 1247-1279 (2002).

Multi-wavelength diffusive optical tomography using Independent Component Analysis and Time Reversal algorithms

M. Alrubaiee[1], Binlin Wu[1], M. Xu[2], W. Cai[1], J. A. Koutcher[3], and S. K. Gayen[1]

[1]*Physics Department, The City College and Graduate Center of the City University of New York, 160 Convent Avenue, New York, New York 10031*
[2]*Department of Physics, Fairfield University, Fairfield, CT 06824, USA*
[3]*Memorial Sloan Kettering Cancer Center, 1275 York Avenue, New York, NY 10021, USA*

ABSTRACT

Optical imaging using independent component analysis (OPTICA) and time reversal optical tomography (TROT) approaches are used to detect, locate, and obtain cross-section images of two tumor pieces inside a model human breast assembled using *ex vivo* human breast tissues and configured as a semi-cylindrical slab of uniform thickness. The experimental arrangement realized a multi-source probing scheme to illuminate an end face (source plane) of the slab sample using 750 nm, 800 nm and 830 nm beams of laser light. A multi-detector signal acquisition scheme measured transmitted light intensity distribution on the other end face (detection plane). This combined multi-source probing and multi-detector sensing approach culminated in multiple spatial and angular views of the sample necessary for target localization. The perturbations in light intensity distribution in the detection plane were analyzed using both the OPTICA and the TROT approaches to obtain locations of the tumor pieces. A back-projection technique with OPTICA provided cross-section images and estimates of cross section of the targets within the sample. The estimated locations and dimensions of targets are in good agreement with the results of a corroborating magnetic resonance imaging experiment and known values.

Keywords: Medical and biological imaging, Image reconstruction techniques, Light propagation in tissues, Inverse problems, Three-dimensional image processing, Tomography, Breast cancer, Magnetic resonance imaging, Independent component analysis.

1. INTRODUCTION

Optical detection of targets in a turbid medium makes use of the difference in optical properties, such as, scattering coefficient, absorption coefficient, index of refraction, and fluorescence between the targets of interest and the intervening medium [1]. Multiple scattering of light by the turbid medium produces a noise background that blurs the image, and in severe cases makes direct imaging impossible. Inverse image reconstruction approaches that are commonly used to retrieve image information have to deal with the fact that inverse problems are ill posed, and attain different measures of success [2].

We are developing the optical tomography using independent component analysis (OPTICA) [3-5], and time reversal optical tomography (TROT) [6-8] approaches for detecting and obtaining three-dimensional location information of target(s) in highly scattering turbid media in general, and of tumor(s) in human breast, in particular. In this paper we present the results of our study of a "realistic model cancerous breast" formed using *ex vivo* human breast tissues with two pieces of tumors embedded within. We use a multi-source, multi-wavelength probing and multi-detector signal acquisition scheme, and analyze the resulting data using both OPTICA and TROT approaches to obtain images and locations of the tumor pieces. These results are compared with magnetic resonance imaging measurements as reference.

2. EXPERIMENTAL METHODS AND MATERIALS

The experimental arrangement for detecting and locating tumors in the realistic model breast using OPTICA and TROT is shown schematically in Fig. 1. The model breast was assembled using two pieces of normal *ex vivo* female human breast tissues. Two pieces of cancerous tissues were sandwiched at different locations within the two normal pieces. The normal breast tissue specimens weighed 119 grams and 127 grams and consisted primarily of adipose tissue, while each tumor (infiltrating ductal carcinoma) piece weighed approximately 1 gram. The sample was placed inside a cylindrical

transparent plastic container of diameter 110 mm with a movable end, which was moved to slightly compress the tissue along the z-axis and hold it in place. The tumor piece located at the left side of the sample ('left tumor') was of the size of 8 mm × 5 mm × 3 mm and that located on the right side ('right tumor') was of the size 10 mm × 10 mm × 5 mm. The axial orientation of the plastic container and sample within it was preserved for magnetic resonance imaging (MRI) experiments following the optical measurements.

The optical imaging experiments were carried out using a beam of light collimated to a 1-mm spot size. Light of three different wavelengths 750 nm, 800 nm, and 830 nm from a Ti:sapphire laser were used in the measurement. The average beam power was maintained at 10 mW for every wavelength. Multiple source illumination was realized in practice by scanning the sample in a 26 × 16 array of *x-y* grid points with a step size of 2.5 mm, while the CCD camera imaged the entire detection plane. Each illuminated pixel of the 1024 × 1024 pixels of the CCD camera could be regarded as a detector. For illumination of every scanned point on the source plane, the CCD camera recorded the diffusely transmitted intensity pattern on the detection plane.

For MRI experiments, the breast model sample in the plastic container was taken to Memorial Sloan-Kettering Cancer Center (MSKCC) small animal MRI facility. The facility currently utilizes a 4.7-T 33-cm (Bruker BioSpin). MR images of the sample were recorded in 2.0-mm slice thick sagittal slices.
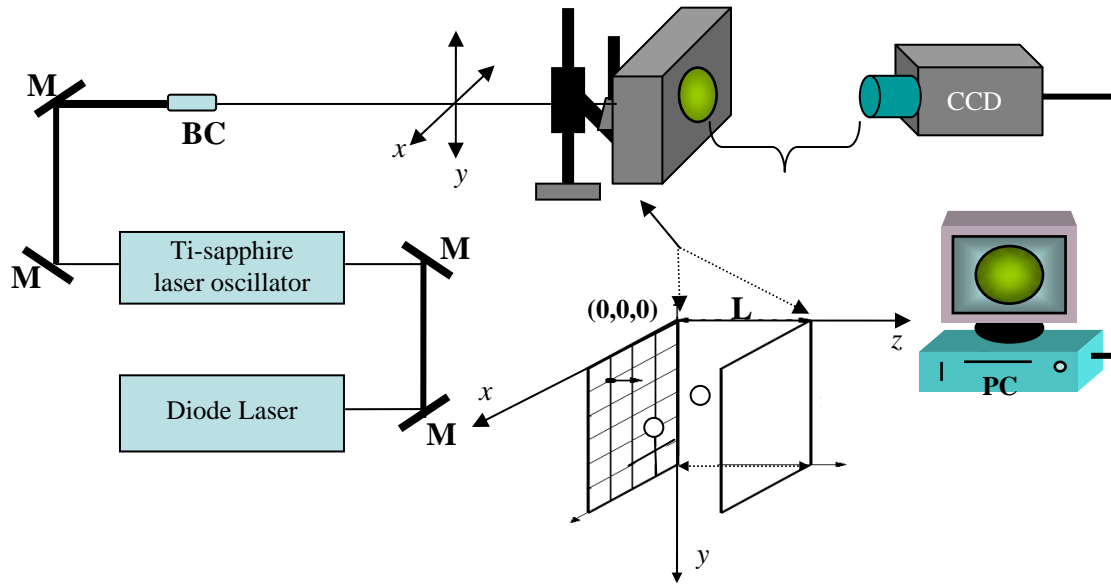

Figure 1. Schematic diagram of the experimental arrangement (M = mirror, BC= beam collimator, CCD = charge-coupled device, PC = personal computer)

3. THEORETICAL FORMALISM

The perturbation of the detected light intensities on the boundaries of the medium, the scattered wave field, due to scattering inhomogeneities is given, in Diffusion Approximation (DA), by [3-5]

$$-\Delta I(\mathbf{r}_d, \mathbf{r}_s; \lambda) = \int d^3 r \delta\mu_a(\mathbf{r}, \lambda) c G(\mathbf{r}_d, \mathbf{r}; \lambda) G(\mathbf{r}, \mathbf{r}_s; \lambda)$$

$$+ \int d^3 r \delta D(\mathbf{r}, \lambda) c \nabla_r G(\mathbf{r}_d, \mathbf{r}; \lambda) \cdot \nabla_r G(\mathbf{r}, \mathbf{r}_s; \lambda)$$

(1)

in the first-order Born approximation assuming that light diffuses inside the medium. In Eq.(1), $\mathbf{r}_s$ and $\mathbf{r}_d$ are the positions of the source and the detector on the boundary, respectively; $\delta\mu_a(\mathbf{r}, \lambda) = \mu_\alpha(\mathbf{r}, \lambda) - \mu_{a0}(\lambda)$ and $\delta D(\mathbf{r}, \lambda) = D(\mathbf{r},$

$\lambda) - D_0(\lambda)$ are the differences in absorption coefficient and diffusion coefficient, respectively, between the target at **r** and the background; c is the speed of light in the medium; and $G(\mathbf{r}, \mathbf{r}'; \lambda)$ is the Green's function describing light propagation from **r'** to **r** inside the background turbid medium of absorption and diffusion coefficients $\mu_{a0}(\lambda)$ and $D_0(\lambda)$ where λ is the wavelength of the probing beam. OPTICA Formalism has been detailed elsewhere [3-5]. For TROT algorithm, the experimental data obtained using the multiple-source and multiple-detector arrangement, were as a response matrix K, expressed as[6-7]

$$K = \{K_{l,j}\} = \sum_{m=1}^{M} G^d(\mathbf{R}_l, \mathbf{X}_m)\tau_m G^s(\mathbf{X}_m, \mathbf{R}_j) \equiv \sum_{m=1}^{M} g_m^d \tau_m g_m^s \qquad (2)$$

$$K = \{K_{j,l}\} = \sum_{m=1}^{M} G^s(\mathbf{X}_m, \mathbf{R}_j)\tau_m G^d(\mathbf{R}_l, \mathbf{X}_m) = \sum_{m=1}^{M} g_m^s \tau_m g_m^d$$

where $j = 1, 2, \ldots, N$ and $l = 1, 2, \ldots, N$ are indices of sources and detectors, respectively; $m = 1, 2, \ldots, M$ is the index of the targets with $M < N$; $\mathbf{R}_j$, $\mathbf{R}_l$ and $\mathbf{X}_m$ are the positions of a source, a detector and a target respectively; τ_m is the difference in the optical parameters (absorption and scattering) of the target from that of the background medium (the background medium may be uniform or non-uniform); $G_s(\mathbf{X}_m, \mathbf{R}_j)$ and $G_d(\mathbf{R}_l, \mathbf{X}_m)$ are the Green's functions in the background medium. The vector $g_m^d = [G^d(\mathbf{X}_m, \mathbf{R}_1), G^d(\mathbf{X}_m, \mathbf{R}_2), \cdots, G^d(\mathbf{X}_m, \mathbf{R}_N)]$ in Eq. (2) has N components [6-7]. From K a time reversal matrix $T = K^T K$ is constructed, and its eigenvalues and eigenvectors are determined. Leading eigenvalues lead to the targets.

4. RESULTS

4.1 OPTICA

OPTICA-generated independent intensity distributions on the detector plane for the two tumors using 750-nm probing are shown in Figure 2(a). Similar intensity distributions were obtained for probing using light of other two wavelengths as well. The x-y-z locations of the left tumor and the right tumor determined from fitting these ICA profiles to the Green's function for all three wavelengths are shown in Table I. The average of the probed tumor positions from all wavelengths is shown in bold. The cross-section images of the two tumors constructed using Back-projection Fourier transform [5] are shown in Figure 2(b).

Table I. The coordinates (x, y, z) of the left tumor and right tumor

Wavelength (nm)	Left Tumor			Right Tumor		
	y (mm)	x (mm)	z (mm)	y (mm)	x (mm)	z (mm)
750	50.3	54.9	20	26.1	48.7	20.2
800	50.5	55.4	17.9	27.1	49.4	19.5
830	49.6	54.2	17.2	27.1	47.2	21.5
Average	**50.1**	**54.8**	**18.4**	**26.8**	**48.4**	**20.4**

4.2 TROT

The TROT algorithm-generated cross-section image of the tumors for $\lambda = 750$ nm is shown in Figure 3(a). Similar images were obtained using other two wavelengths. The locations were found to be (11.5mm, 33.1mm, 22.5 mm) for the left tumor and (42.6 mm, 38.6 mm, 20.5 mm) for the right tumor. Since the tumors depth location is at the mid plane ~ 20-mm, we compare the horizontal separation between the two tumors and find it to be 35.8-mm using OPTICA and 31.1-mm using TROT. The optical results are in good agreement with the MR images at depth 22.5 mm shown 3(b) and 3(c) and separation of 35 mm.
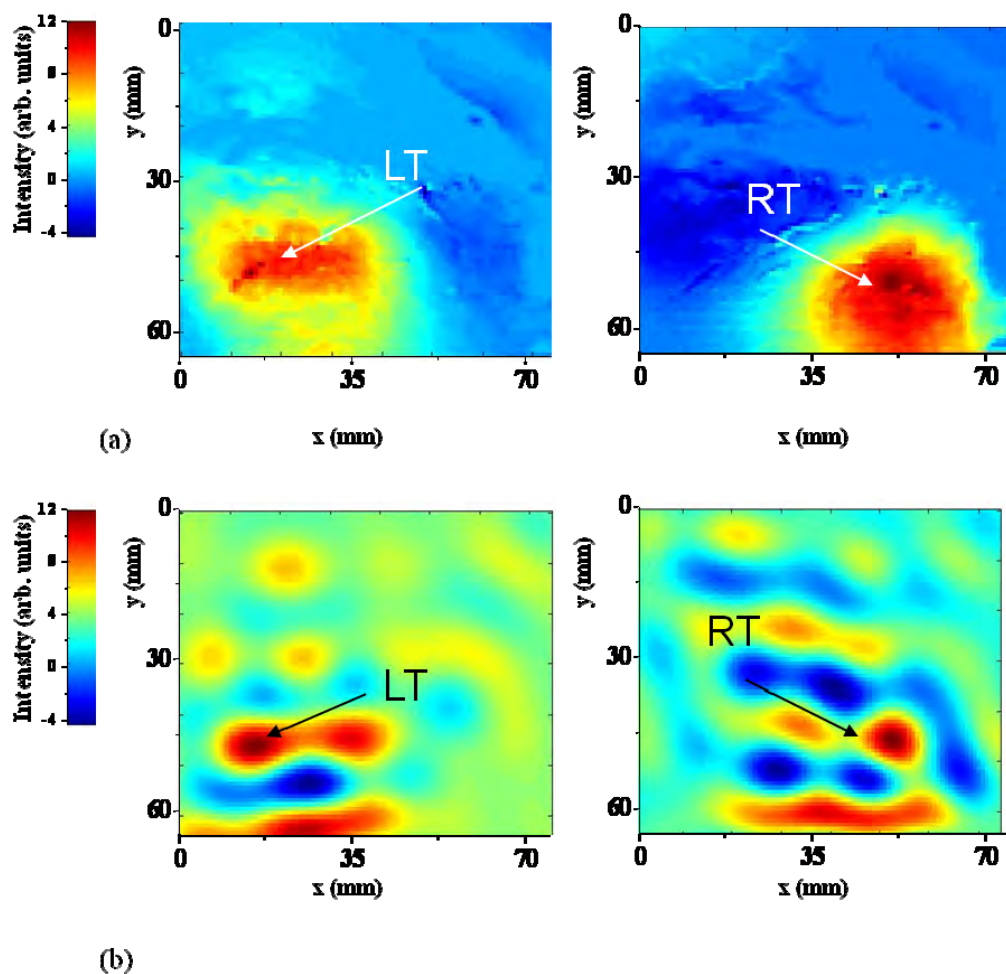
Figure 2. (a) OPTICA generated intensity distributions pertaining to the left tumor (LT) and right tumor (RT) for 750-nm probing. (b) Cross-section images formed by Back-projection Fourier transform.
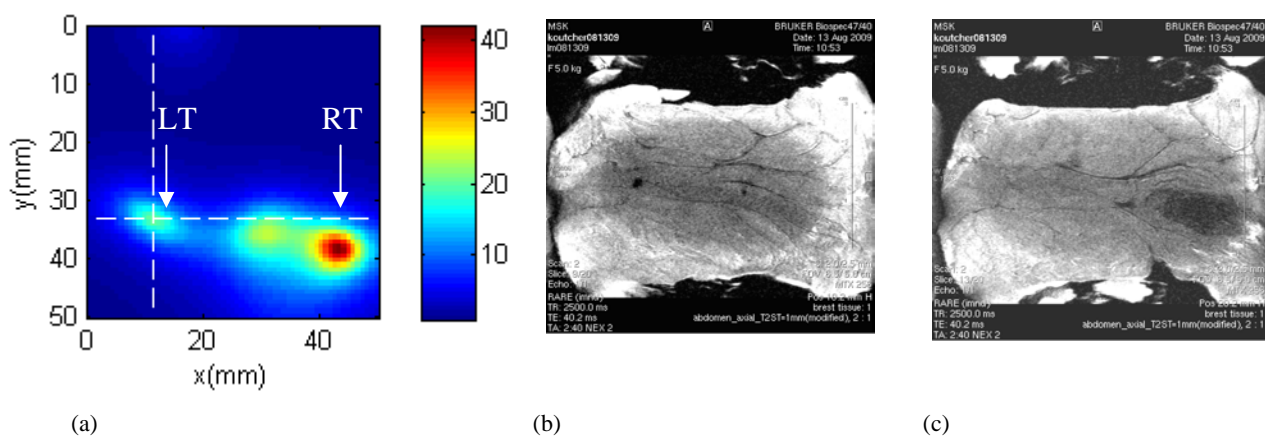

Figure 3. (a) TROT generated cross-section image. (b) Left tumor LT at slice depth $z = 18.5$-mm, and (c) Right tumor RT at slice depth $z = 22.5$-mm

5. SUMMARY

The two approaches provided comparable information, and successfully detected and located the two tumors. The use of multi-wavelength method eliminated some artifacts. The implementation time was under 1 minute. Although we have used the DA in this case, the approach can use other light propagation models. It can be used with continuous wave, frequency-domain and time-resolved experimental data. Future work on this approach will be directed towards estimating the optical properties, as well as, size and shape of targets.

ACKNOWLEDGEMENTS

REFERENCES

[1] S. K. Gayen and R. R. Alfano, "Emerging optical biomedical imaging techniques," *Opt. Photon. News* **7**(3), 22 (1996).

[2] S. R. Arridge, "Optical tomography in medical imaging," *Inverse Probl.* **15**, R41–R93 (1999).

[3] M. Xu, M. Alrubaiee, S. K. Gayen, and R. R. Alfano, "Optical diffuse imaging of an ex vivo model cancerous human breast using independent component analysis", *IEEE J. Sel. Top. Quantum Electron.* **14**, 43-49 (2008).

[4] M. Alrubaiee, M. Xu, S. K. Gayen, M. Brito, and R. R. Alfano, "Three-Dimensional Optical Tomographic Imaging of Scattering Objects in Tissue-Simulating Turbid Media Using Independent Component Analysis", *Appl. Phys. Lett.* **87**, 191112-1 (2005)

[5] M. Alrubaiee, M. Xu, S. K. Gayen, and R. R. Alfano, "Localization and Cross Section Reconstruction of Fluorescent Targets in Ex Vivo Breast Tissue Using Independent Component Analysis", *Appl. Phys. Lett.* **89**, 133902-1 (2006).

[6] A. J. Devaney, "Time reversal imaging of obscured targets from multistatic data," *IEEE Trans. Antenn. Propag.* **53**, 1600-1610 (2005).

[7] W. Cai, M. Alrubaiee, S. K. Gayen, M. Xu, R. R. Alfano, "Three-dimensional optical tomography of objects in turbid media using the round-trip matrix, " *Proc. SPIE* **5693**, 4 (2005).

[8] Binlin Wu, W. Cai, M. Alrubaiee, M. Xu and S. K. Gayen, "Three dimensional time reversal optical tomography", *Proc. SPIE* **7892**, 78920G (2011).

Diffuse Optical Imaging using Decomposition Methods

Binlin Wu, M. Alrubaiee, W. Cai, M. Xu[*] and S. K. Gayen

Physics Department, The City College and The Graduate Center of The City University of New York

160 Convent Ave, New York, NY 10031, USA

Email: bwu@sci.ccny.cuny.edu

* Physics Department, Fairfield University

1073 North Benson Road, Fairfield, CT 06824, USA

Abstract

Diffuse optical imaging (DOI) for detecting and locating targets in a highly scattering turbid medium is treated as a Blind Source Separation (BSS) problem. Three matrix decomposition methods, Independent Component Analysis (ICA), Principal Component Analysis (PCA) and Non-negative Matrix Factorization (NMF) were used to study the DOI problem. The efficacy of resulting approaches was evaluated and compared using simulated and experimental data. Samples used in the experiments included Intralipid-10% or Intralipid-20% suspension in water as the medium with absorptive or scattering targets embedded.

1. Introduction

Diffuse optical imaging (DOI) for detection and retrieval of location information of targets in a highly scattering turbid medium may be treated as a blind source separation (BSS) problem [1, 2]. Various matrix decomposition methods, such as, Independent Component Analysis (ICA) [3], Principal Component Analysis (PCA) [4] and Non-negative Matrix Factorization (NMF) [5, 6] have been developed for solving the BSS problem and retrieving desired information.

Min Xu *et al.* adapted ICA of information theory to develop Optical Tomography using Independent Component Analysis (OPTICA) and demonstrated its application for diffuse imaging of absorptive, scattering and fluorescent targets [7-11]. ICA assumes the signals from different targets to be *independent* of each other, and optimizes a relevant measure of independence to obtain the ICs associated with different targets. The position co-ordinates of targets in three dimensions are determined from the individual components separately.

PCA assumes that the PCs contributing to the signal are *uncorrelated* and explain the most variance in the signal. PCA has been widely used in various applications, such as spectroscopy [12], face recognition [13] and neuroimaging [14]. NMF seeks to factorize a matrix into two non-negative matrices (component signals and weights) and requires the contributions to signal and the weights of the components to be *non-negative*. It does not imply any relationship between the components. NMF has also been widely used in biological analysis [15], and spectral analysis [16].

The objective of this study is to test and compare the efficacy of these algorithms when used to solve the DOI problem. Results are presented and compared using simulative data and

1

experimental data using absorptive and scattering targets embedded in model scattering media. Our interest in solving the DOI problem derives from the need for a non-invasive modality for detecting, locating, and diagnosing breast tumors in early stages of growth.

The remainder of the article is organized as follows. In Section 2, the formalisms of the three methods are introduced. Section 3 evaluates the resulting imaging approaches using simulated data. The approaches are further examined in Section 4 for experimental data acquired using absorptive and scattering targets embedded in model scattering media. Section 5 summarizes and discusses the results.

2. Formalism

2.1 Blind Source Separation problem

Blind source separation (BSS), also known as blind signal separation is a general problem in information theory that seeks to separate different individual signals from the measured signals, which are weighted mixtures of those individual signals. Assuming M individual signals, $s_j(t); j = 1, \cdots M$, are linearly mixed instantaneously, the BSS problem is modeled as following. The dimension of $s_j(t)$ is N_s, the number of sampling times. In this presented study, t will be replaced by spatial positions of the excitation light sources. A total of N_d detectors sense N_d different mixtures of $s_j(t)$. The mixture measured by the ith detector can be presented as $x_i(t) = \sum_{j=1}^{M} a_{ij} s_j(t)$, or $X = AS$, in a matrix notation, where $A \in R^{N_d \times M}$ is a mixing or weighting matrix, $S \in R^{M \times N_s}$, $X \in R^{N_d \times N_s}$, and $M < \min(N_s, N_d)$. The objective of BSS is to retrieve the signals $s_j(t)$ and their weights, a_{ij}. ICA, PCA and NMF are statistical analysis methods, used to solve the BSS problem.

2.2 Diffuse optical imaging problem

In DOI one measures the signal at the sample boundary, which includes a weighted mixture of contributions from embedded targets. One uses the diffusion approximation [17-19] of the radiative transfer equation [20, 21] as the forward model to describe light propagation in a highly scattering turbid medium. The perturbation in the light intensity distribution measured on the boundary of the sample due to the presence of the targets (which are localized inhomogeneities in the optical properties within the sample volume) may be written, in the first order Born approximation, as [22, 23]

$$\Delta\phi(\boldsymbol{r}_d, \boldsymbol{r}_s) = -\int G(\boldsymbol{r}_d, \boldsymbol{r})\delta\mu_a(\boldsymbol{r})cG(\boldsymbol{r}, \boldsymbol{r}_s)d^3\boldsymbol{r}$$
$$-\int \delta D(\boldsymbol{r})c\nabla_r G(\boldsymbol{r}_d, \boldsymbol{r}) \cdot \nabla_r G(\boldsymbol{r}, \boldsymbol{r}_s)d^3\boldsymbol{r}, \tag{1}$$

where $\boldsymbol{r}_s$, $\boldsymbol{r}_d$, and $\boldsymbol{r}$ are the positions of a source of unit power, detector and target, respectively; $G(\boldsymbol{r}, \boldsymbol{r}_s)$ and $G(\boldsymbol{r}_d, \boldsymbol{r})$ are the Green's functions that describe light propagation from the source to the target and from the target to the detector, respectively; $\delta\mu_a$ and δD are the differences in absorption coefficient and diffusion coefficient between the targets and the background medium, respectively; and c is the light speed in the medium.

A multi-source illumination and multi-detector signal acquisition scheme is used to acquire light transmitted through a scattering medium. For small absorptive targets, a perturbation data matrix is constructed using $-\Delta\phi$ for all sources. The elements of the data matrix pertaining to absorptive targets represented by the first term in Eq. (1) may be written in a discrete form as:

2

$$X_{ij} = \sum_{m=1}^{M} G^d(\boldsymbol{r}_i, \boldsymbol{r}_m) \tau_m G^s(\boldsymbol{r}_m, \boldsymbol{r}_j), (i = 1,2, \cdots N_d; j = 1,2, \cdots, N_s), \tag{2}$$

where $\boldsymbol{r}_i$, $\boldsymbol{r}_j$ and $\boldsymbol{r}_m$ are the locations of the ith detector, j^{th} source and m^{th} target, respectively; N_s, N_d and M are the numbers of sources, detectors and targets, respectively; $\tau_m = \delta\mu_a(\boldsymbol{r}_m)c\delta V_m$ is the optical absorption strength of the mth target, δV_m is the volume of the target; $G^s(\boldsymbol{r}_m, \boldsymbol{r}_j)$ and $G^d(\boldsymbol{r}_i, \boldsymbol{r}_m)$ are the Green's functions that describe light propagation from j^{th} source to m^{th} target and from m^{th} target to i^{th} detector, respectively. The number of targets is assumed to be less than that of sources and detectors, $M < \min(N_d, N_s)$.

The mth target may be considered to be a virtual source of strength $\tau_m G^s(\boldsymbol{r}_m, \boldsymbol{r}_j)$ excited by the real light source located at $\boldsymbol{r}_j$. The data matrix $X = \{X_{ij}\}$, may be considered to be a set of combinations of light signals from all virtual sources mixed by a mixing matrix $\{G^d(\boldsymbol{r}_i, \boldsymbol{r}_m)\}$. Therefore, this problem can be treated as a BSS problem.

As the second term in Eq. (1) suggests, each scattering target is represented by three co-located virtual sources of strength: $\tau_m \partial_p G^s(\boldsymbol{r}_m, \boldsymbol{r}_j)$, where $\partial_p = \frac{\partial}{\partial p}, (p = x, y, z)$, and $\tau_m = \delta D(\boldsymbol{r}_m)c\delta V_m$, is the optical scattering strength of the mth target [8]. The mixing matrices become $\{\partial_p G^d(\boldsymbol{r}_i, \boldsymbol{r}_m)\}$, $(p = x, y, z)$, for the three virtual sources generated by the mth target. The elements of the data matrix for scattering targets may be written as

$$X_{ij} = \sum_{m=1}^{M} \sum_{p=\{x,y,z\}} \partial_p G^d(\boldsymbol{r}_i, \boldsymbol{r}_m) \tau_m \partial_p G^s(\boldsymbol{r}_m, \boldsymbol{r}_j). \tag{3}$$

Since one absorptive target is represented by one centrosymmetric virtual source, while three virtual sources (one centrosymmetric and two dumb-bell shaped) represent one scattering target [7, 8], the number and patterns of virtual sources may be used, in favorable situations, to identify the target as absorptive or scattering in nature. In this paper, only small targets are considered since all three algorithms are suited for small targets, and early detection, when the tumors are more amenable to treatment, is of practical interest.

2.3 DOI as a BSS problem

The data matrix for the DOI problem may be written as

$$X = AS = \sum_{m=1}^{M} A_{im} S_{mj}, \tag{4}$$

where $A \in R^{N_d \times M}$, $S \in R^{M \times N_s}$, and $X \in R^{N_d \times N_s}$. For absorptive targets,

$$A_{im} = \beta_m G^d(\boldsymbol{r}_i, \boldsymbol{r}_m) \text{ and } S_{mj} = \alpha_m G^s(\boldsymbol{r}_m, \boldsymbol{r}_j), \tag{5a}$$

while for scattering targets,

$$A_{im} = \beta_m \partial_p G^d(\boldsymbol{r}_i, \boldsymbol{r}_m) \text{ and } S_{mj} = \alpha_m \partial_p G^s(\boldsymbol{r}_m, \boldsymbol{r}_j). \tag{5b}$$

$\{S_{mj}\}$ $(j = 1,2, \cdots, N_s)$ and $\{A_{im}\}$ $(i = 1,2, \cdots N_d)$ are two-dimensional intensity distributions on the source and detector planes, respectively. Source and detector planes are the boundaries of the sample through which light enters and exits the sample volume, respectively. The scaling factors β_m and α_m are related to the target optical strength, $\tau_m = \alpha_m \beta_m$. The location of the target and the scaling factors can be retrieved using a least squares fitting via

$$\text{argmin}_{\alpha_m, \beta_m, \boldsymbol{r}_m} \{ \sum_j [\alpha_m^{-1} S_{mj} - G^s(\boldsymbol{r}_m, \boldsymbol{r}_j)]^2$$

$$+ \sum_i [\beta_m^{-1} A_{im} - G^d(\boldsymbol{r}_i, \boldsymbol{r}_m)]^2 \}, \text{ or} \tag{6a}$$

$$\text{argmin}_{\alpha_m, \beta_m, r_m} \{\Sigma_p \{\Sigma_j [\alpha_m^{-1} S_{mj} - \partial_p G^s(\boldsymbol{r_m}, \boldsymbol{r_j})]^2$$
$$+ \Sigma_i [\beta_m^{-1} A_{im} - \partial_p G^d(\boldsymbol{r_i}, \boldsymbol{r_m})]^2\}\}, \tag{6b}$$

for absorptive and scattering targets, respectively. However, when a scattering target is embedded deep in a turbid medium, only the $\tau_m \, \partial_z G^s(\boldsymbol{r_m}, \boldsymbol{r_j})$ virtual source remains significant. So only $p = z$ may be used for fitting in Eq. (6b) [8].

2.3.1 ICA

OPTICA assume that the virtual sources are *independent* of each other [8]. So they can be retrieved through an iterative process which seeks to maximize the independence among the components. In practice, the independent components are found by maximizing some measure of non-Gaussianity, such as kurtosis (the fourth-order cumulant), of the unmixed components. A Matlab program for ICA was adopted from http://sccn.ucsd.edu/eeglab/. The location of the target can be retrieved by fitting the independent component intensity distributions (ICIDs) to Green's functions or derivatives of Green's functions using Eqs. 6(a) and 6(b).

2.3.2 PCA

PCA assumes that the virtual sources are uncorrelated so that the correlation (covariance) between them is ideally zero, and minimal in practice. The covariance matrix of S, $cov(S)$ should be diagonal. The general process of PCA is as follows. The data matrix $X = AS + N$, where N is random noise added to the data, A and S the same as defined in Eq. (4). When S is mean centered, elements of the mean-centered matrix S' are defined as

$$S'_{mj} = S_{mj} - \frac{1}{N_s} \Sigma_{j=1}^{N_s} S_{mj}. \tag{7a}$$

Similarly

$$X'_{ij} = X_{ij} - \frac{1}{N_s} \Sigma_{j=1}^{N_s} X_{ij}. \tag{7e}$$

PCA looks for a matrix P that decomposes X into virtual sources, $S = PX$. It also holds that $S' = PX'$, since P is just a rotation matrix which does not change the center of the data.

$$cov(S) = S'S'^T = (PX')(PX')^T = PX'X'^T P^T = \Lambda, \tag{8}$$

where $\Lambda = \text{diag}\{\lambda_1, \lambda_2, \cdots\}$. The eigenvalues λ_m are variances in the covariance matrix. Therefore, $X'X'^T P^T = P^T \Lambda$, where P^T is orthonormal. PCA is realized by eigenvalue decomposition (EVD) of the covariance matrix of X. The eigenvectors with leading eigenvalues (largest variances) are selected to be the PCs using the L-curve [24].

Since, $X = P^T S \approx AS$, A is determined as a matrix including only PCs. S is calculated as $S \approx (A^T A)^{-1} A^T X$. Rows of S and columns of A represent principal component intensity distributions (PCIDs) on the source plane and detector plane, respectively, and are proportional to the images of the virtual sources projected on the source and detector planes. The target positions are determined using Eq. (6).

2.3.3 NMF

NMF is a group of multivariate analysis algorithms that factorize a matrix X into A and S: $X = AS$, A and S are non-negative [6]. Unlike ICA and PCA, NMF does not imply any relationship between the retrieved components; instead, it just enforces non-negativity constraints on A and S.

4

There are various algorithms developed to solve NMF, such as the multiplicative update method [5] and alternating least squares method [25, 26].

In the multiplicative update implementation of NMF, A and S can be found by minimizing the square of Euclidean distance $\|X - AS\|^2$ as the cost function, where $A \geq 0$ and $S \geq 0$, using the multiplicative update rule

$$A_{ik} \leftarrow A_{ik} \frac{(XS^T)_{ik}}{(ASS^T)_{ik}}, \tag{9a}$$

$$S_{kj} \leftarrow S_{kj} \frac{(A^T X)_{kj}}{(A^T AS)_{kj}}. \tag{9b}$$

The alternating least squares implementation of NMF uses alternate least squares steps to estimate A (or S), and use that estimate to optimize S (or A), and keep repeating the alternative steps until the desired optimization is obtained. Non-negativity is ensured by setting any negative element of A or S equal to 0.

A NMF toolbox was obtained from http://cogsys.imm.dtu.dk/toolbox/ to perform NMF computation. A built-in command *nnmf* is also available in Matlab (R2011a).

NMF algorithm requires that the non-negativity assumption must hold in the problem. In particular, for absorptive targets, when X is constructed with $-\Delta\phi$, τ_m should be positive, i.e. the targets should be more absorbing than the background. If the targets have weaker attenuation properties than the background, X needs to be constructed with $+\Delta\phi$ instead. For scattering targets, X should be treated similarly to keep its elements positive.

When NMF is applied to a scattering target, only the centrosymmetric component shows up properly, since the other two components have dumb-bell shape which includes negative values [8]. So without any prior knowledge or some other experimental means to assess if the target is absorptive or scattering, NMF may not distinguish between the two possibilities.

The decomposition methods can be applied with different sample geometries such as slab and cydrindrical geometries, and different measurement domains such as time-resolved domain, frequency domain and continuous wave (CW). In this article, Green's functions for slab geometry [23] with CW measurement were used for simulation and experiments.

3. Simulation

The sample was considered to be a 40-mm thick uniform scattering slab with lateral dimension of 80 mm × 80 mm, as shown in Fig. 1. Its absorption and diffusion coefficients were taken to be $\mu_a = 0.003$ mm^{-1} and $D = \frac{1}{3}$ mm (transport mean free path, $l_t = 1$ mm), respectively, which are similar to the average value of those parameters for human breast tissue. An absorptive and a scattering point target were placed at (50, 60, 15) mm and (30, 30, 25) mm, respectively. The index of refraction n of the medium was taken to be 1.33. The speed of light is 2.998×10^8 m/s, or 299.8 mm/ns in vacuum, and 225.4 mm/ns in the medium. The absorption coefficient of the absorptive target was set to be higher than the background with $\Delta\mu_a = 0.001$ mm^{-1}, while the diffusion coefficient was taken to be the same as that of background. The diffusion coefficient of the scattering target was set to be lower than the background (higher scattering coefficient) with $\Delta D = -0.1$ mm ($l_t = 0.7$ mm), while the absorption coefficient was taken to be the same as the

background. The volumes of both targets are set to be 8 mm^3. The optical strengths of the absorptive and scattering targets were $\Delta\mu_a c \Delta V$ = 1.803 mm^3/ns, and $\Delta D c \Delta V$ = -180.3 mm^5/ns, respectively. The incident CW beam step scanned the sample at 21 × 21 grid points covering an 80 × 80 mm^2 area, with a step size of 4 mm. Light on the opposite side was recorded at 41 × 41 grid points covering the same area. Multiplicative Gaussian noise of 5% was added to the simulated data. The data matrix X was then obtained using Eq. (2) directly, and analyzed using the three different algorithms.
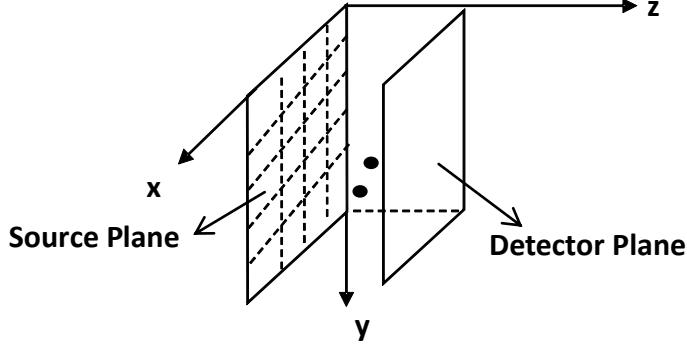

Fig. 1: Light intensity distribution on the detector plane is recorded when a point source scans on the source plane.

3.1 ICA Analysis

One independent component for the absorptive target and three independent components for the scattering target were retrieved by ICA. The independent component intensity distributions (ICIDs) on the detector plane are shown in Figs. 2(a), 2(c), 2(d), and 2(e). Similar ICIDs were obtained on the source plane. Fig. 2(g) shows the centrosymmetric ICID for the scattering target, and Fig. 2(i) shows the ICID for the absorbing target.

The components in either the detector plane or the source plane can, in principle, be used to extract position and optical strength of the target(s). However, in our experimental arrangement signal is collected by a 1024 × 1024 pixels CCD camera, while the source plane is scanned in an *x-y* array of points, which is much smaller than the number of pixels in the CCD camera. Consequently, the resolution in the detector plane is much better, and the data set more robust than the source side. So, we used the images on the detector plane for retrieving target information using experimental data. While it would not matter in simulation, to be consistent with experimental situations, we employed detector plane images when using simulated data as well for all three algorithms. Table I lists the locations and strengths of the absorptive and scattering targets retrieved by fitting the spatial intensity profile of the centrosymmetric components on the detector plane to Green's functions and derivatives of Green's functions using Eq. 6(a) and Eq. 6(b), respectively, as shown in Fig. 2(b) and Fig. 2(f). Fig. 2(h) and Fig. 2(j) show the corresponding fits to the profiles on the source plane.

6

Detector Plane Images and Profiles

(a)

(b)

(c)

(d)

(e)

(f)

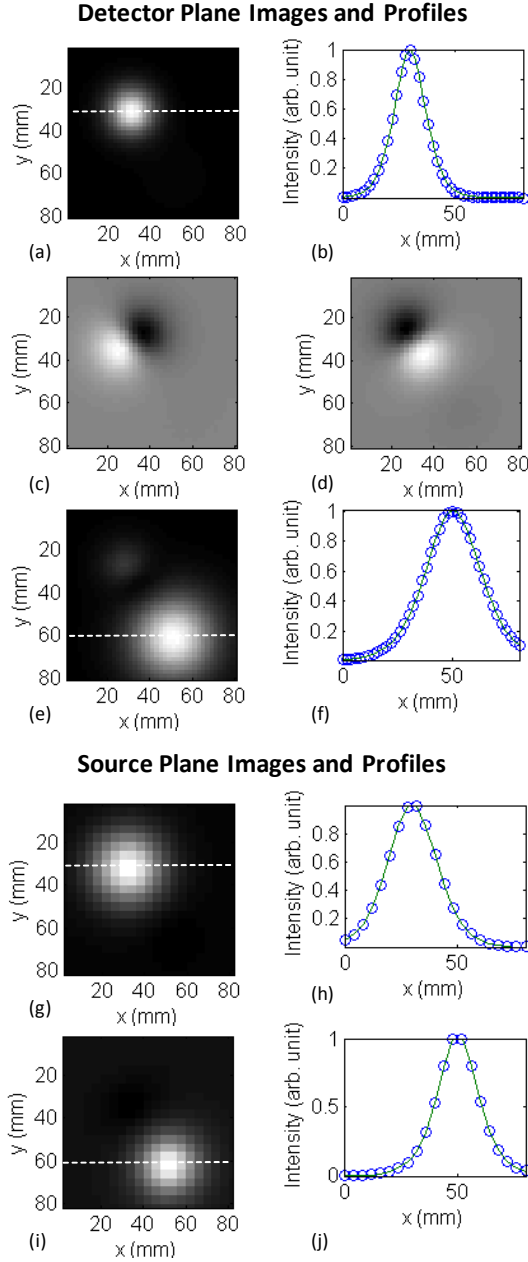**Source Plane Images and Profiles**

(g)

(h)

(i)

(j)

Fig. 2: ICA extracted two-dimensional intensity distribution on the detector plane of: (a) the centrosymmetric component, (c), (d) dumb-bell shaped components of the scattering target; and (e) the absorptive target. Similar intensity distribution on the source plane of: (g) the centrosymmetric component of the scattering target, and (i) the absorptive target for comparison. Fits to the spatial intensity profile on the detector plane along the white dashed line (shown in figures) of the centrosymmetric component of the scattering target is shown in (b), and that of the absorptive target is shown in (f). Corresponding fits to spatial profiles on the source plane are displayed in (h) and (j), respectively.

3.2 PCA Analysis

Eigenvalue equation of the covariance matrix of X was solved. The eigenvalues found by PCA were sorted in descending order. Fig. 3 shows a plot of leading 20 eigenvalues on a logarithmic scale.
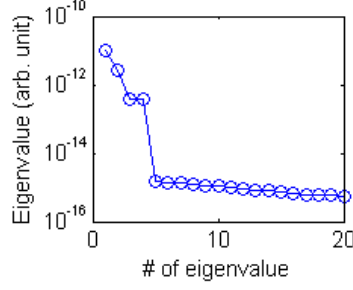
7

Fig. 3: A logarithmic plot of the first 20 PCA eigenvalues

First four leading eigenvalues were selected for PCs. The corresponding PCIDs were calculated. The PCIDs on the detector plane are shown in Fig. 4. Similar images for PCIDs on the source plane were obtained. The scattering target has one centrosymmetric (Fig. 4(a)) component and two dumb-bell shaped (Fig. 4(c) and Fig. 4(d)) components, while the absorptive target has only one component (Fig. 4(e)).
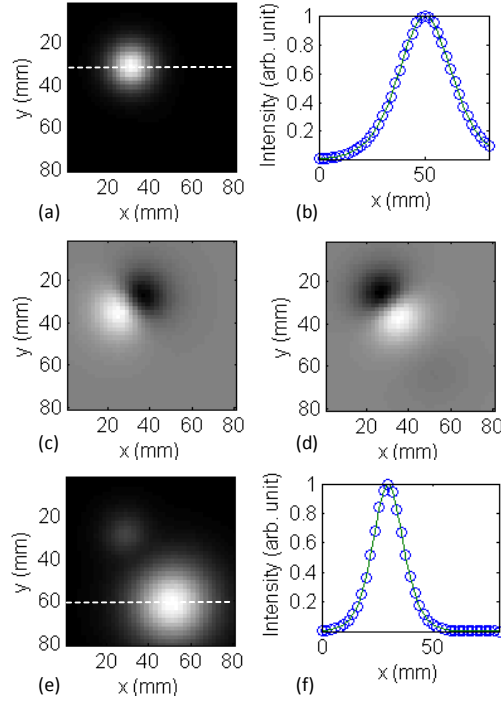

Fig. 4: PCA-extracted two dimensional intensity distribution on the detector plane of: (a) the centrosymmetric component, and (c), (d) dumb-bell shaped components of the scattering target; (e) the absorptive target. Green's function fits to the spatial intensity profiles along the dashed line (shown in figures) of the (b) centrosymmetric component of the scattering target and (f) absorptive target, respectively, to retrieve the locations of the two targets.

Fig. 4(b) and Fig. 4(f) show fits to the spatial intensity profile of the centrosymmetric component of the scattering target and that of the absorptive target, respectively, to retrieve the locations of the two targets. The locations and optical strengths of the targets retrieved by PCA are also shown in Table I.

3.3 NMF Analysis

The mixing matrix and virtual sources were retrieved from the data matrix X using NMF as explained in Section 2.3.3. As in the other two approaches, only one component is extracted for

8

the absorptive target. Since NMF has a non-negativity constraint, only the centrosymmetric component for the scattering target is obtained. Non-negative component intensity distributions (NCIDs) on detector planes are shown in Fig. 5. Similar images for NCIDs on source plane were also obtained using the virtual sources in S. The results are also shown in Table I.
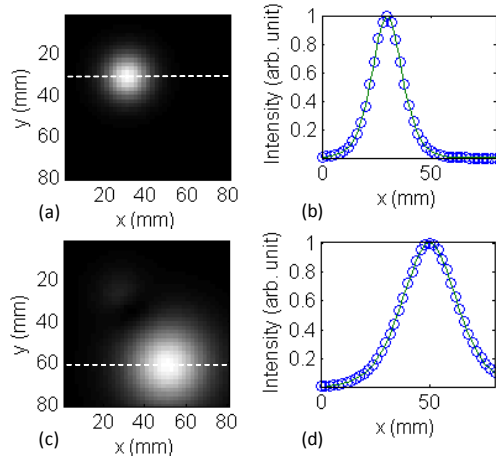

Fig. 5: NMF-extracted two dimensional intensity distribution on the detector plane of: (a) the centrosymmetric component of the scattering target; (c) the absorptive target. Fits to the corresponding spatial intensity profiles along the dashed line (shown in figures) are shown in (b) and (d), respectively.

3.4 Results and discussion

The positions and optical strengths of the targets retrieved by ICA, PCA and NMF algorithms are shown in Table I, and compared to the known values. The retrieved results using all three algorithms from this simulated data are in excellent agreement with the known values.

Table I. Positions and optical strengths retrieved using simulated data and ICA, PCA and NMF algorithms

Target	Known position (mm)	Algorithm	Fitted position (mm)	Error (mm)	Known* strength	Fitted* strength	Error (%)
Sca.	(30, 30, 25)	ICA	(29.9, 30.0, 25.1)	(0.1, 0, 0.1)	-180.3	-179.9	0.22
		PCA	(30.0, 30.0, 25.0)	(0, 0, 0)	-180.3	-180.1	0.11
		NMF	(30.0, 30.0, 25.0)	(0, 0, 0)	-180.3	-178.5	1
Abs.	(50, 60, 15)	ICA	(50.1, 60.2, 15.0)	(0.1, 0.2, 0)	1.803	1.826	1.28
		PCA	(50.1, 60.1, 14.9)	(0.1, 0.1, 0.1)	1.803	1.812	0.5
		NMF	(50.1, 60.1, 15.0)	(0.1, 0.1, 0)	1.803	1.803	0

* The unit for absorption strength of the target is mm^3/ns and for scattering strength is mm^5/ns.

9

4. Experiments

4.1 Experimental materials and methods

In this Section, the algorithms are evaluated using experimental data for absorptive and scattering targets embedded in model scattering media whose absorption and scattering properties are adjusted to mimic the average values of those parameters for human breast tissues. Two different experiments were carried out with two different samples. The first sample used a 250 mm × 250 mm × 50 mm transparent plastic container filled with Intralipid-10% suspension in water as the background medium. The concentration of Intralipid-10% was adjusted to provide [27, 28] an absorption coefficient of $\mu_a \sim 0.003$ mm^{-1}, and a transport mean free path $l_t \sim 1.43$ mm at 785 nm. The second sample used a similar container with dimension of 250 mm × 250 mm × 60 mm filled with Intralipid-20% suspension in water. The concentration of Intralipid-20% was adjusted to provide [27, 28] $\mu_a \sim 0.003$ mm^{-1}, and $l_t \sim 1$ mm at 785 nm. These optical parameters of the medium were selected to be similar to the average values of those parameters for human breast tissue. The thickness of the samples was also comparable to that of a typical compressed female human breast.

In the first experiment, two absorptive targets were embedded in the medium. The targets were ~ 10-mm diameter glass spheres filled Indocyanine green (ICG) dye dissolved in Intralipid-20% suspension in water to obtain an absorption coefficient $\mu_a = 1.15$ mm^{-1} at 785 nm, and to match the background scattering coefficient of 2.11 mm^{-1}. The targets were placed at (57.2, 18.1, 20.0) mm and (19.9, 48.1, 25.0) mm, respectively.

In the second experiment, two scattering targets were embedded, which were also ~ 10 mm diameter glass spheres, filled with Intralipid-20% suspension in water. The transport mean free path, l_t was adjusted to be 0.25 mm, with scattering coefficient $\mu_s \approx 11$ mm^{-1}, and absorption coefficient μ_a same as the background medium. The targets were placed in the middle plane ($z = 30$ mm) in the container with a lateral distance of 40 mm from each other (center to center).

The experimental setup is schematically shown in Fig. 6. A 10-mW 785-nm diode laser beam was used to illuminate the first sample, while a 100-mW 790-nm diode laser beam was used for the second sample. The input surface (source plane) of the samples was scanned across the laser beam in an x-y array of grid points to realize the multi-source interrogation of the samples. The transmitted light from the exit surface (detector plane) was recorded by a 1024 pixel ×1024 pixel (pixel size = 24 μm) CCD camera (Photometrics CH350) equipped with a 60-mm focal-length camera lens. Each pixel of the CCD camera can be considered to be a detector implementing the multi-detector signal acquisition arrangement. A set of 16-bit 1024 pixel ×1024 pixel images were acquired. The two samples were scanned in an array of 11×12 and 11×15 grid points, respectively, with a step size of 5 mm in both cases. The processes of scanning and data acquisition were controlled by a personal computer. At all scan positions, raw transillumination images of the samples were recorded by the computer for further analysis.
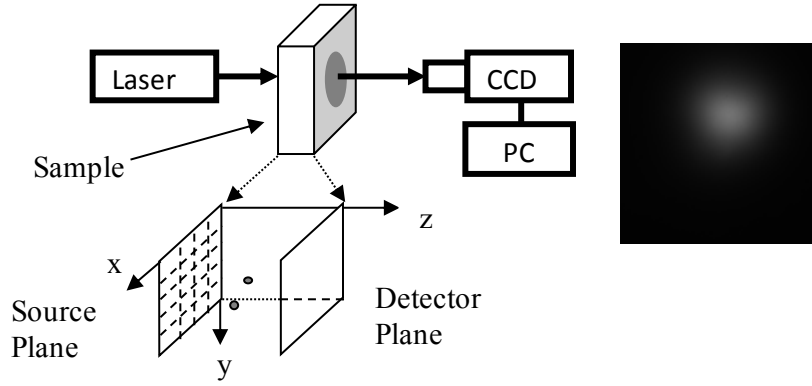
Fig. 6: A schematic diagram of the experimental arrangement used for imaging objects embedded in a turbid medium. The inset at the bottom shows the 2D array in the input plane that was scanned across the incident laser beam; and the inset to the right shows a typical raw image recorded by the CCD. (CCD = charge coupled device, PC = personal computer)

4.2 Analysis and Results

A region of interest (ROI) was cropped out from each image. Then every 5×5 pixels in each cropped image were binned to one pixel to enhance signal-to-noise ratio. A background image was generated by calculating an average image for all scan positions to approximate the transillumination image without target(s) embedded.

This averaging method for generating background image is suitable for small targets used in our experiments, as the ratio of the volume of the sample to that of the target was quite high (~500:1). For *in vivo* imaging of tumors in early stages of growth, the breast-to-tumor volume ratio will be similarly high and the averaging method will be applicable. Alternative approaches for generating a background image include using image of (a) a phantom that has the same average optical properties as the sample [29]; (b) the healthy contralateral breast for breast imaging [30]; and (c) the sample obtained using light of wavelength for which the target(s) and the background have identical optical properties [31]. Still another approach is to compute the background using an appropriate forward model [32]. A more detailed discussion of this important issue appears in one of our earlier publications [33].

The background image was also cropped and binned corresponding to the ROI for each scan position. Perturbation in the light intensity distribution, $\Delta\phi$ due to targets in each image was found by subtracting the background image from the image. The data matrix X was then constructed using the light intensity perturbations at all scan positions. ICA, PCA, and NMF decomposition algorithms were performed on the data matrix separately. Results are shown and discussed below.

4.2.1 Absorptive targets

The images on the detector plane obtained using the ICA, PCA, and NMF algorithms are shown in Fig. 7, Fig. 8, and Fig. 9, respectively. Similar images on the source plane were also obtained using all three algorithms. The right side of each figure shows the corresponding spatial intensity profile. Locations of the targets are extracted from fits to these spatial intensity profiles, as described in Section 2.3 using Eq. (6). The results are presented in Table II. In Fig. 7, images on

the source plane are shown in (e) and (g), and Green's function fits to their spatial profiles are shown in (f) and (h) for comparison.
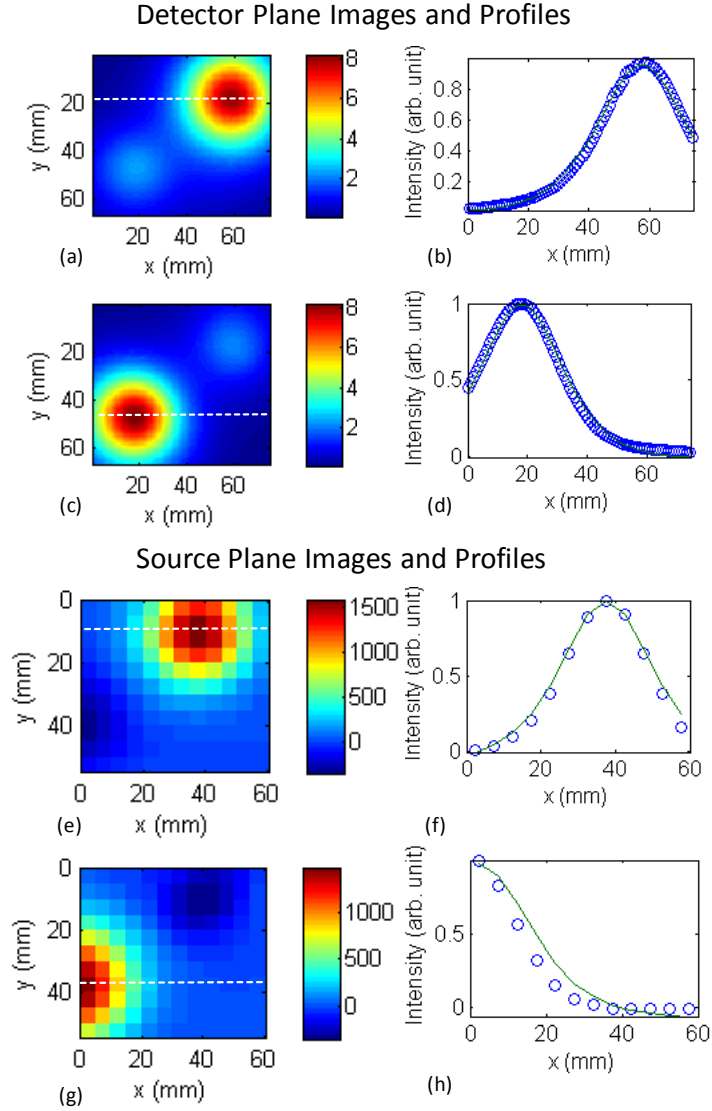

Fig. 7: ICA-generated ICIDs on the detector plane are shown in (a) and (c); corresponding Green's function fits to the horizontal spatial profiles through the dashed lines are shown in (b) and (d). ICIDs on the source plane are shown in (e) and (g); corresponding Green's function fits to the horizontal spatial profiles through the dashed line are shown in (f) and (h).

12

Fig. 8: PCIDs on the detector plane are shown in (a) and (c); and corresponding Green's function fits to the horizontal spatial profiles through the dashed line are shown in (b) and (d).

Fig. 9: NCIDs on the detector plane are shown in (a) and (c); corresponding Green's function fits to the horizontal spatial profiles through the dashed line are shown in (b) and (d).
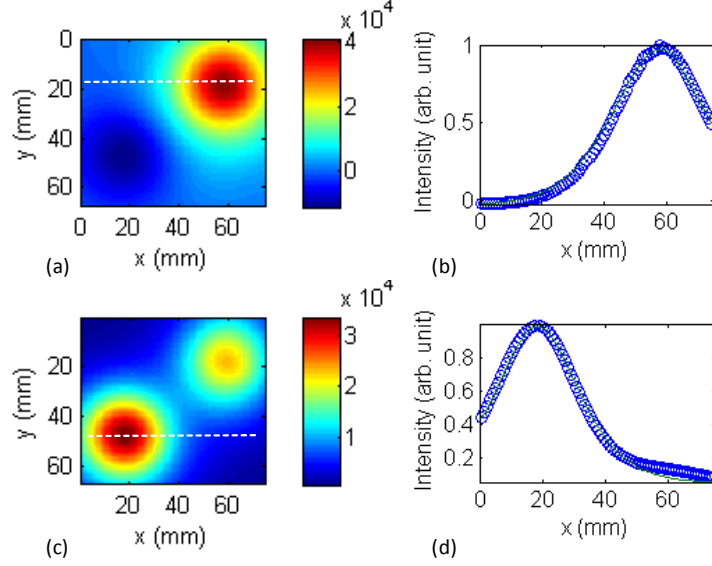
It follows from the comparison of in Table II that the positions retrieved by all three algorithms are in good agreement with the known positions. The errors in the retrieved locations (x, y, z) of the two targets were within 1.7 mm. The PCIDs were not totally separated. Some "residue" was observed in one PCID from the other. ICA and NMF separated two components from this dataset more clearly.

13

Table II. Known positions vs. retrieved positions of the absorptive targets using ICA, PCA and NMF algorithms

Target	Known position (mm)	Algorithm	Fitted position (mm)	Error (mm)
1	(57.2, 18.1, 20)	ICA	(57.4, 18.2, 21.5)	(0.2, 0.1, 1.5)
		PCA	(57.4, 18.2, 20.6)	(0.2, 0.1, 0.6)
		NMF	(57.4, 18.2, 19.5)	(0.2, 0.1, 0.5)
2	(19.9, 48.1, 25)	ICA	(18.2, 46.7, 24.7)	(1.7, 1.4, 0.3)
		PCA	(18.2, 47.6, 25.9)	(1.7, 0.5, 0.9)
		NMF	(18.2, 47.6, 23.3)	(1.7, 0.5, 1.7)

4.2.2 Scattering targets

The "images" corresponding to the centrosymmetric components of the virtual sources (targets) on the detector plane obtained using the ICA, PCA, and NMF algorithms are shown in Fig. 10, Fig. 11, and Fig. 12, respectively. Similar images on the source plane were also obtained. The right side of each figure shows the corresponding spatial intensity profile. Locations of the targets are extracted from fits to these spatial intensity profiles, as described in Section 2.3 using Eq. (6). The results are presented in Table III.

Fig. 10: ICA-generated ICIDs on the detector plane are shown in (a) and (c); corresponding Green's function fits to the horizontal spatial profiles through the dashed line are shown in (b) and (d).
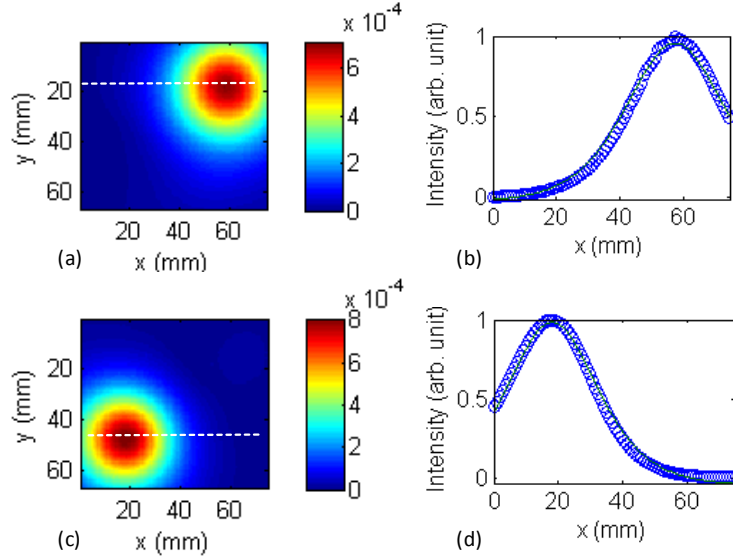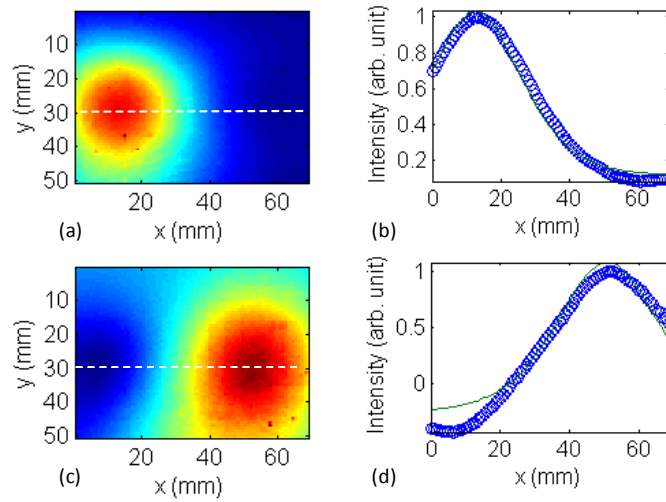
14

Fig. 11: PCIDs on the detector plane are shown in (a) and (c); corresponding Green's function fits to the horizontal spatial profiles through the dashed line are shown in (b) and (d).

Fig. 12: NCIDs on the detector plane are shown in (a) and (c); corresponding Green's function fits to the horizontal spatial profiles through the dashed line are shown in (b) and (d).
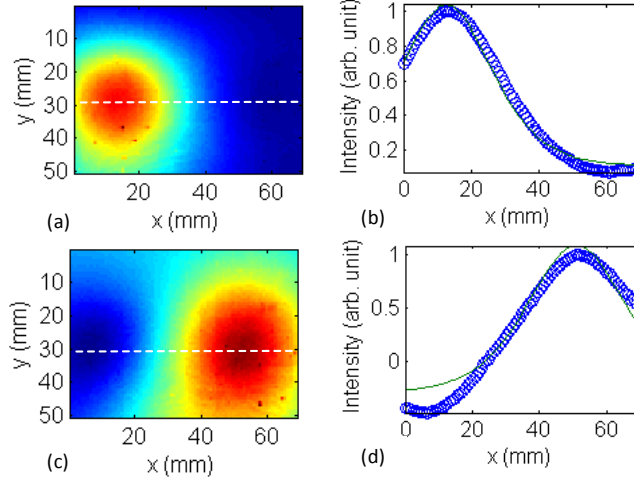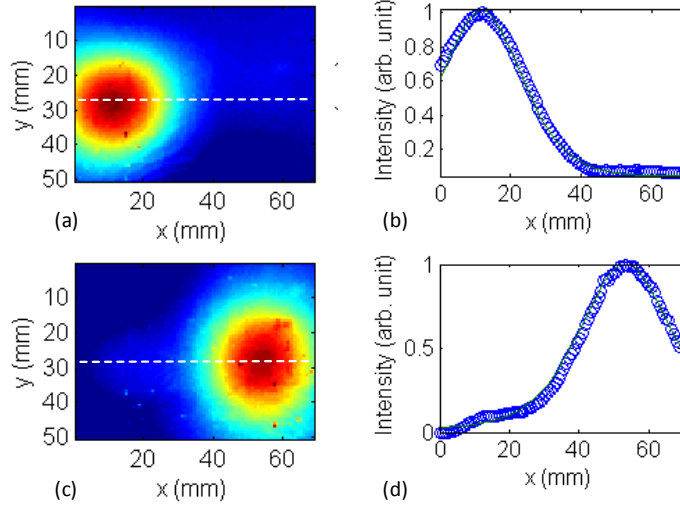
Both targets were detected by all three algorithms. The target locations retrieved by three algorithms are shown in Table III, and compared with known locations. Overall, all three algorithms detect and locate the scattering and the absorptive targets with good accuracy, the maximum deviation of any one coordinate from the known value being ~3 mm. Since the maximum difference between the known and retrieved position coordinates was larger for the scattering targets, we calculated the squared correlation coefficient γ to assess the fitting quality. NMF retrieves the position coordinates better (within 0.5 mm) for the scattering target #2 than done by ICA and PCA (deviation from known values being between 2-3 mm). NMF retrieved the position coordinates for target #1 with 3.0 mm error in z direction, which is not as good as that done by ICA and PCA. But γ is 0.783 and 0.778 in the fittings for ICA and PCA, respectively, as compared to 0.993 for NMF, indicating that the quality of the fitting is better for NMF. The quality of fitting is presumably affected by the efficacy of decomposition. The decomposed NCIDs by NMF were more "clean" than those decomposed by ICA and PCA. We ascribe the observed higher errors in ICA and PCA estimates of the position coordinates of the

15

scattering target #2 than the NMF estimates to the interference from the other virtual source (corresponding to target #1) in ICA (Fig. 10(c)) and PCA (Fig. 11(c)) images. It is commonly believed that errors in locating a scattering target are higher than that for locating an absorptive target, and the results of this study conform to that notion.

Table III: Known positions vs. retrieved positions of the scattering targets using ICA, PCA and NMF algorithms

Target #	Known position (mm)	Algorithm	Fitted position (mm)	Error (mm)
1	(13.0, 28.0, 30.0)	ICA	(12.6, 28.7, 29.1)	(0.4, 0.7, 0.9)
		PCA	(12.6, 28.7, 28.6)	(0.4, 0.7, 1.4)
		NMF	(12.0, 28.5, 33.0)	(1.0, 0.5, 3.0)
2	(53.3, 28.5, 30.0)	ICA	(51.0, 31.8, 26.8)	(2.3, 3.3, 3.2)
		PCA	(50.9, 31.8, 26.7)	(2.4, 3.3, 3.3)
		NMF	(53.3, 28.0, 30.3)	(0.0, 0.5, 0.3)

5. Summary and Discussion

Diffusive optical imaging was modeled as a BSS problem. ICA, PCA and NMF were used to decompose the data matrix, and locate the targets embedded in a highly scattering turbid medium. Only the components corresponding to the targets were extracted from a large dataset for target detection and localization.

It may be instructive to compare the objectives, scope and computational complexity of these decomposition methods with model-based reconstruction methods. Decomposition methods obtain the 3-D locations of targets (the number of targets are generally small). Based on the retrieved locations, the methods may then be further extended to retrieve size and optical property information of the targets [9]. The common practice of model-based inverse reconstruction methods is to discretize the sample volume into $N \times N \times N$ voxels, and estimate absorption and/or scattering coefficient in each voxel iteratively. Voxels with significantly different optical properties than the surrounding are regions of interest, and may be identified as targets. While estimating the optical properties, the forward model is solved repeatedly to calculate the intensity of the multiply-scattered light on the sample boundary. The difference between the intensity of the multiply scattered light predicted by the forward model and the experimental measurements is minimized by seeking an optimal set of the optical properties of every voxel in the sample volume. The number of variables thus is on the order N^3. To determine location(s) of target(s) in three dimensions, the decomposition methods process the data matrix to retrieve the main components (A and S). Here A and S are two-dimensional matrices with the number of unknowns on the order of N^2. The number of unknowns is, hence, reduced N times in the decomposition methods compared to the model-based approaches, which leads to a substantial saving in the computational time when N is large. No repeated solution of the forward model is involved in decomposition methods. Consequently, decomposition methods are considerably faster.

16

A comparison of the computational complexity of these two types of approaches may shed further light on their relative computation economy. For a model-based iterative reconstruction method, an equation of the form $b = Wx$ is solved to find the targets, where W is a weight matrix of *size* $N_dN_s \times N_v$, N_d, N_s, and N_v are the numbers of detectors, sources and voxels, respectively, b is an $N_dN_s \times 1$ vector describing the perturbation in the detected light intensity due to the presence of targets, and x is the perturbation in the optical properties from the background values with dimension of $N_v \times 1$. The computational complexity is typically $O(N_dN_sN_v^2)$ for a single iteration. For the decomposition approach, b is written as a 2-D matrix X with dimension $N_d \times N_s$. To decompose matrix X, the computational complexity per iteration is typically of order $O(N_dN_k)$ for ICA [34], and $O(N_dN_sN_k)$ for NMF [35], where N_k is the number of components that relates to the number of targets and is usually a small number. For PCA using SVD, the complexity is $O(N_s^2N_k)$ [34]. The computational complexity of the intrinsic iterative process involved in the matrix decomposition algorithms is much lower than that in the model-based inverse reconstruction methods.

All three matrix decomposition methods presented in this manuscript can potentially be used in *in-vivo* real-time breast cancer imaging. The three algorithms have different assumptions, which may lead to different favored conditions. In this study, the algorithms were evaluated using simulative and experimental data using model scattering media and absorptive and scattering targets. The (x, y, z) positions of the targets were retrieved with good accuracy. The decomposition provided by ICA is "cleaner" than that of the PCA. PCA did not clearly separate the two absorptive targets used in the first experiment. NMF decomposition seems to provide residue-free "cleaner" images than the other two methods in this study. However, since NMF is based on non-negativity assumption, the results might deteriorate when such a non-negativity assumption does not hold well. While continuous wave measurements were used in the work presented in this article, the approaches could be used with frequency domain and time-domain measurements as well.

The work presented here focuses on detecting and locating small targets, which derive impetus from the need to detect tumors in early stages of growth when those are more amenable to treatment. All three methods are applicable for extended targets as well, and are expected to provide the "center of optical strength" as the location of the target.

All three approaches are applicable for both scattering and absorbing targets, and may be used in clinical setting. The contrast between a tumor and surrounding normal tissue can be due to differences in absorption, scattering, or both absorption and scattering properties and may depend significantly on the wavelength of light used. However, *a priori* knowledge of the optical characteristics (absorptive or scattering) is not crucial. As has been shown [Eq. (2) and Eq. (3)] the expression for elements of the data matrix for absorptive targets involves Green's Functions G, while that for scattering targets involves $\partial G/\partial z \approx -\kappa G$, where $\kappa = \sqrt{\mu_a/D}$ in CW [9]. This relationship with G provides basis for detection and localization of target(s), whether contrast is due to absorption, scattering, or both. We are using transillumination geometry, which is one of the approaches used by other researchers, and adequate signal for *in vivo* breast imaging is obtained [29, 36-39].

In this article, we presented results when the approaches were used to detect and obtain three-dimensional location information of the targets. We have demonstrated, while developing OPTICA [11] that a back-projection formalism can be further implemented to get a cross-section

image of the target [11], or the retrieved target locations can be fed into other DOI methods as *a priori* information to get three-dimensional tomographic images. Since the approaches are suited for small targets, these hold promise for detecting and locating breast tumors in early stages of growth, which is crucially important for effective treatment. Further work involving *ex vivo* (model) and *in vivo* imaging of cancerous breast will be needed to establish the full potential of these approaches.

Acknowledgement

References

1. X. R. Cao, and R.-W. Liu, "General approach to blind source separation," IEEE Trans. Signal Process. **44**, 562-571 (1996).
2. J. F. Cardoso, "Blind signal separation: statistical principle," Proc IEEE **86**, 2009-2025 (1998).
3. A. Hyvärinen, J. Karhunen, and E. Oja, *Independent Component Analysis* (Wiley, New York, 2001).
4. I. T. Jolliffe, *Principal Component Analysis* (Springer, New York, 1986).
5. D. D. Lee, and H. S. Seung, "Learning the parts of objects by non-negative matrix factorization," Nature **401**, 788-791 (1999).
6. M. W. Berry, M. Browne, A. N. Langville, V. P. Pauca, and R. J. Plemmons, "Algorithms and applications for approximate nonnegative matrix factorization," Comp. Stat. Data Anal. **52**, 155-173 (2007).
7. M. Xu, M. Alrubaiee, S. K. Gayen, and R. R. Alfano, "Optical imaging of turbid media using independent component analysis: theory and simulation," J. Biomed. Opt. **10**, 051705 (2005).
8. M. Xu, M. Alrubaiee, S. K. Gayen, and R. R. Alfano, "Three-dimensional localization and optical imaging of objects in turbid media with independent component analysis," Appl. Opt. **44**, 1889-1897 (2005).
9. M. Xu, M. Alrubaiee, S. K. Gayen, and R. R. Alfano, "Optical diffuse imaging of an *ex vivo* model cancerous human breast using independent component analysis," IEEE J. Select. Topics Quantum Electron. **14**, 43-49 (2008).
10. M. Alrubaiee, M. Xu, S. K. Gayen, M. Brito, and R. R. Alfano, "Three-dimensional optical tomographic imaging of scattering objects in tissue-simulating turbid media using independent component analysis," Appl. Phys. Lett. **87**, 191112 (2005).
11. M. Alrubaiee, M. Xu, S. K. Gayen, and R. R. Alfano, "Localization and cross section reconstruction of fluorescent targets in *ex vivo* breast tissue using independent component analysis," Appl. Phys. Lett. **89**, 133902 (2006).
12. D. L. Massart, B. G. M. Vandeginste, S. M. Deming, Y. Michotte, and L. Kaufman, *Chemometrics: A Textbook* (Elsevier, Amsterdam, 1988).
13. M. Turk, and A. Pentland, "Eigenfaces for recognition," J. Cogn. Neurosci. **3**, 71-86 (1991).
14. L. K. Hansen, J. Larsen, F. A. Nielsen, S. C. Strother, E. Rostrup, R. Savoy, N. Lange, J. Sidtis, C. Svarer, and O. B. Paulson, "Generalizable patterns in neuroimaging: how many principal components?," Neuroimage **9**, 534-544 (1999).

15. J.-P. Brunet, P. Tamayo, T. R. Golub, and J. P. Mesirov, "Metagenes and molecular pattern discovery using matrix factorization," Proc. Natl. Acad. Sci. **101**, 4164-4169 (2004).
16. V. P. Pauca, J. Piper, and R.J. Plemmons, "Nonnegative matrix factorization for spectral data analysis," Lin. Alg. Appl. **416**, 29-47 (2006).
17. A. Ishimaru, "Diffusion of a pulse in densely distributed scatterers," J. Opt. Soc. Am. **68**, 1045-1050 (1978).
18. K. Furutsu, "Diffusion equation derived from the space-time transport equation," J. Opt. Soc. Am. **70**, 360-366 (1980).
19. M. S. Patterson, B. Chance, and B. C. Wilson, "Time resolved reflectance and transmittance for the non-invasive measurement of tissue optical properties," Appl. Opt. **28**, 2331-2336 (1989).
20. S. Chandrasekhar, *Radiative Transfer* (Clarendon Press, Oxford, 1950).
21. A. Ishimaru, *Wave Propagation and Scattering in Random Media, Volume 1: Single Scattering and Transport Theory* (Academic, New York, 1978).
22. S. R. Arridge, and J. C. Schotland, "Optical tomography: forward and inverse problems," Inverse Probl. **25**, 123010 (2009).
23. S. R. Arridge, "Photon-measurement density functions. part I: analytical forms," Appl. Opt. **34**, 7395-7409 (1995).
24. P. C. Hansen, "Analysis of discrete ill-posed problems by means of the L-curve," SIAM (Soc. Ind. Appl. Math.) Rev. **34**, 561-580 (1992).
25. P. Paatero, and U. Tapper, "Positive matrix factorization: a non-negative factor model with optimal utilization of error estimates of data values," Environmetrics **5**, 111–126 (1994).
26. P. Paatero, "The multilinear engine: a table-driven least squares program for solving multilinear problems, including the *n*-way parallel factor analysis model," J. Comp. Graph. Stat. **8**, 854–888 (1999).
27. H. J. van Staveren, C. J. M. Moes, J. van Marle, S. A. Prahl, and M. J. C. van Gemert, "Light scattering in Intralipid-10% in the wavelength range of 400--1100 nm," Appl. Opt. **31**, 4507-4514 (1991).
28. C. Bordier, C. Andraud, J. Lafait, E. Charron, M. Anastasiadou, and A. de Martino, "Illustration of a bimodal system in Intralipid 20% by polarized light scattering: experiments and modelling," Appl. Phys. A **94**, 347-355 (2009).
29. T. Nielsen, B. Brendel, R. Ziegler, M. van Beek, F. Uhlemann, C. Bontus, and T. Koehler, "Linear image reconstruction for a diffuse optical mammography system in a noncompressed geometry using scattering fluid," Appl. Opt. **48**, D1-D13 (2009).
30. Y. Ardeshirpour, N. Biswal, A. Aguirre, and Q. Zhu, "Artifact reduction method in ultrasound-guided diffuse optical tomography using exogenous contrast agents," J. Biomed. Opt. **16**, 046015 (2011).
31. B. W. Pogue, M. S. Patterson, H. Jiang, and K. D. Paulsen, "Initial assessment of a simple system for frequency domain diffuse optical tomography," Phys. Med. Biol. **40**, 1709-1729 (1995).
32. A. Poellinger, J. C. Martin, S. L. Ponder, T. Freund, B. Hamm, U. Bick, and F. Diekmann, "Near-infrared laser computed tomography of the breast first clinical experience," Acad. Radiol. **15**, 1545–1553 (2008).
33. Binlin Wu, W. Cai, M. Alrubaiee, M. Xu, and S. K. Gayen, "Time reversal optical tomography: locating targets in a highly scattering turbid medium," Opt. Express **19**, 21956-21976 (2011).

34. T. Ristaniemi, and J. Joutsensalo, "Advanced ICA-based receivers for block fading DS-CDMA channels," Signal Processing **82**, 417-431 (2002).

35. V. P. Pauca, J. Piper, and R. J. Plemmons, "Nonnegative matrix factorization for spectral data analysis," Linear Algebra Appl. **416**, 29-47 (2006).

36. M. Cutler, "Transillumination as an aid in the diagnosis of breast lesions," Surg. Gynecol. Obstet. **48**, 721–729 (1929).

37. R. Choe, A. Corlu, K. Lee, T. Durduran, S. D. Konecky, M. Grosicka-Koptyra, S. R. Arridge, B. J. Czerniecki, D. L. Fraker, A. DeMichele, B. Chance, M. A. Rosen, and A. G. Yodh, "Diffuse optical tomography of breast cancer during neoadjuvant chemotherapy: a case study with comparison to MRI," Med. Phys. **32**, 1128-1139 (2005).

38. A. Pifferi, P. Taroni, A. Torricelli, F. Messina, R. Cubeddu and G. Danesini, "Four-wavelength time-resolved optical mammography in the 680–980-nm range," Opt. Lett. **28**, 1138-1140 (2003).

39. B. J. Tromberg, B. W. Pogue, K. D. Paulsen, A. G. Yodh, D. A. Boas, and A. E. Cerussi, "Assessing the future of diffuse optical imaging technologies for breast cancer management," Med. Phys. **35**, 2443-2451 (2008).

Time reversal optical tomography: locating targets in a highly scattering turbid medium

Binlin Wu,[1,2,*] W. Cai,[1] M. Alrubaiee,[1] M. Xu,[3] and S. K. Gayen[1,2]

[1]*Physics Department, The City College of the City University of New York, 160 Convent Ave, New York, NY 10031, USA*

[2]*Physics Department, The Graduate Center of the City University of New York, 365 5th Ave, New York, NY 10016, USA*

[3]*Physics Department, Fairfield University, 1073 North Benson Road, Fairfield, CT 06824, USA*

*bwu@sci.ccny.cuny.edu

Abstract: A time reversal optical tomography (TROT) method for near-infrared (NIR) diffuse optical imaging of targets embedded in a highly scattering turbid medium is presented. TROT combines the basic symmetry of time reversal invariance and subspace-based signal processing for retrieval of target location. The efficacy of TROT is tested using simulated data and data obtained from NIR imaging experiments on absorptive and scattering targets embedded in Intralipid-20% suspension in water, as turbid medium. The results demonstrate the potential of TROT for detecting and locating small targets in a turbid medium, such as, breast tumors in early stages of growth.

©2011 Optical Society of America

OCIS codes: (110.0113) Imaging through turbid media; (110.6955) Tomographic imaging; (110.3080) Infrared imaging; (170.3880) Medical and biological imaging; (170.3010) Image reconstruction techniques; (170.3830) Mammography; (170.0170) Medical optics and biotechnology; (170.6510) Spectroscopy, tissue diagnostics.

References and links

1. A. P. Gibson, J. C. Hebden, and S. R. Arridge, "Recent advances in diffuse optical imaging," Phys. Med. Biol. **50**(4), R1–R43 (2005).
2. M. A. O'Leary, D. A. Boas, B. Chance, and A. G. Yodh, "Experimental images of heterogeneous turbid media by frequency-domain diffusing-photon tomography," Opt. Lett. **20**(5), 426–428 (1995).
3. S. R. Arridge and J. C. Hebden, "Optical imaging in medicine: II. Modelling and reconstruction," Phys. Med. Biol. **42**(5), 841–853 (1997).
4. S. R. Arridge, "Optical tomography in medical imaging," Inverse Probl. **15**(2), R41–R93 (1999).
5. W. Cai, S. K. Gayen, M. Xu, M. Zevallos, M. Alrubaiee, M. Lax, and R. R. Alfano, "Optical tomographic image reconstruction from ultrafast time-sliced transmission measurements," Appl. Opt. **38**(19), 4237–4246 (1999).
6. B. A. Brooksby, H. Dehghani, B. W. Pogue, and K. D. Paulsen, "Near-infrared (NIR) tomography breast image reconstruction with *a priori* structural information from MRI: algorithm development for reconstructing heterogeneities," IEEE J. Sel. Top. Quantum Electron. **9**(2), 199–209 (2003).
7. Y. Yao, Y. Wang, Y. Pei, W. Zhu, and R. L. Barbour, "Frequency-domain optical imaging of absorption and scattering distributions by a Born iterative method," J. Opt. Soc. Am. A **14**(1), 325–342 (1997).
8. S. R. Arridge, M. Schweiger, M. Hiraoka, and D. T. Delpy, "A finite element approach for modeling photon transport in tissue," Med. Phys. **20**(2), 299–309 (1993).
9. N. Kroman, J. Wohlfahrt, H. T. Mouridsen, and M. Melbye, "Influence of tumor location on breast cancer prognosis," Int. J. Cancer **105**(4), 542–545 (2003).
10. D. S. Kepshire, S. C. Davis, H. Dehghani, K. D. Paulsen, and B. W. Pogue, "Subsurface diffuse optical tomography can localize absorber and fluorescent objects but recovered image sensitivity is nonlinear with depth," Appl. Opt. **46**(10), 1669–1678 (2007).
11. P. Mohajerani, A. A. Eftekhar, and A. Adibi, "Object localization in the presence of a strong heterogeneous background in fluorescent tomography," J. Opt. Soc. Am. A **25**(6), 1467–1479 (2008).
12. A. Godavarty, A. B. Thompson, R. Roy, M. Gurfinkel, M. J. Eppstein, C. Zhang, and E. M. Sevick-Muraca, "Diagnostic imaging of breast cancer using fluorescence-enhanced optical tomography: phantom studies," J. Biomed. Opt. **9**(3), 488–496 (2004).
13. Q. Zhao, L. Ji, and T. Jiang, "Improving depth resolution of diffuse optical tomography with a layer-based sigmoid adjustment method," Opt. Express **15**(7), 4018–4029 (2007).
14. M. Alrubaiee, M. Xu, S. K. Gayen, M. Brito, and R. R. Alfano, "Three-dimensional optical tomographic imaging of scattering objects in tissue-simulating turbid medium using independent component analysis," Appl. Phys. Lett. **87**(19), 191112 (2005).

15. M. Alrubaiee, M. Xu, S. K. Gayen, and R. R. Alfano, "Localization and cross section reconstruction of fluorescent targets in *ex vivo* breast tissue using independent component analysis," Appl. Phys. Lett. **89**(13), 133902 (2006).
16. M. Xu, M. Alrubaiee, S. K. Gayen, and R. R. Alfano, "Three-dimensional localization and optical imaging of objects in turbid media with independent component analysis," Appl. Opt. **44**(10), 1889–1897 (2005).
17. M. Xu, M. Alrubaiee, S. K. Gayen, and R. R. Alfano, "Optical diffuse imaging of an *ex vivo* model cancerous human breast using independent component analysis," IEEE J. Sel. Top. Quantum Electron. **14**(1), 43–49 (2008).
18. A. Poellinger, J. C. Martin, S. L. Ponder, T. Freund, B. Hamm, U. Bick, and F. Diekmann, "Near-infrared laser computed tomography of the breast first clinical experience," Acad. Radiol. **15**(12), 1545–1553 (2008).
19. V. Ntziachristos, A. G. Yodh, M. Schnall, and B. Chance, "Concurrent MRI and diffuse optical tomography of breast after indocyanine green enhancement," Proc. Natl. Acad. Sci. U.S.A. **97**(6), 2767–2772 (2000).
20. Q. Zhu, M. Huang, N. G. Chen, K. Zarfos, B. Jagjivan, M. Kane, P. Hedge, and S. H. Kurtzman, "Ultrasound-guided optical tomographic imaging of malignant and benign breast lesions: initial clinical results of 19 cases," Neoplasia **5**(5), 379–388 (2003).
21. A. Li, E. L. Miller, M. E. Kilmer, T. J. Brukilacchio, T. Chaves, J. Stott, Q. Zhang, T. Wu, M. Chorlton, R. H. Moore, D. B. Kopans, and D. A. Boas, "Tomographic optical breast imaging guided by three-dimensional mammography," Appl. Opt. **42**(25), 5181–5190 (2003).
22. W. Cai, M. Alrubaiee, S. K. Gayen, M. Xu, and R. R. Alfano, "Three-dimensional optical tomography of objects in turbid media using the round-trip matrix," Proc. SPIE **5693**, 4–9 (2005).
23. B. Wu, M. Alrubaiee, W. Cai, M. Xu, and S. K. Gayen, "Optical imaging of objects in turbid media using principal component analysis and time reversal matrix methods," in *Computational Optical Sensing and Imaging*, OSA Technical Digest (CD) (Optical Society of America, 2009), paper JTuC10. http://www.opticsinfobase.org/abstract.cfm?uri=COSI-2009-JTuC10
24. B. Wu, W. Cai, M. Alrubaiee, M. Xu, and S. K. Gayen, "Three dimensional time reversal optical tomography," Proc. SPIE **7892**, 78920G (2011).
25. C. Prada, F. Wu, and M. Fink, "The iterative time reversal mirror: a solution to self-focusing in the pulse echo mode," J. Acoust. Soc. Am. **90**(2), 1119–1129 (1991).
26. M. Fink, C. Prada, F. Wu, and D. Cassereau, "Self-focusing in inhomogeneous media with time-reversal acoustic mirrors," in *IEEE Ultrasonics Symposium Proceedings* (Montreal, Que., Canada, 1989), vol. 2, pp. 681–686.
27. M. Fink, "Time reversal of ultrasonic fields. I. Basic principles," IEEE Trans. Ultrason. Ferroelectr. Freq. Control **39**(5), 555–566 (1992).
28. M. Fink, "Time reversal mirrors," J. Phys. D Appl. Phys. **26**(9), 1333–1350 (1993).
29. C. Prada, L. Thomas, and M. Fink, "The iterative time reversal process: analysis of the convergence," J. Acoust. Soc. Am. **97**(1), 62–71 (1995).
30. A. J. Devaney, E. A. Marengo, and F. K. Gruber, "Time-reversal-based imaging and inverse scattering of multiply scattering point targets," J. Acoust. Soc. Am. **118**(5), 3129–3138 (2005).
31. M. Fink, D. Cassereau, A. Derode, C. Prada, P. Roux, M. Tanter, J. L. Thomas, and F. Wu, "Time-reversed acoustics," Rep. Prog. Phys. **63**(12), 1933–1995 (2000).
32. W. A. Kuperman, W. S. Hodgkiss, H. C. Song, T. Akal, C. Ferla, and D. R. Jackson, "Phase conjugation in the ocean: experimental demonstration of an acoustic time reversal mirror," J. Acoust. Soc. Am. **103**(1), 25–40 (1998).
33. G. Lerosey, J. de Rosny, A. Tourin, and M. Fink, "Focusing beyond the diffraction limit with far-field time reversal," Science **315**(5815), 1120–1122 (2007).
34. A. J. Devaney, "Super-resolution processing of multi-static data using time reversal and MUSIC" (2000). http://www.ece.neu.edu/faculty/devaney/ajd/preprints.htm.
35. H. Lev-Ari and A. J. Devaney, "The time reversal techniques re-interpreted: subspace-based signal processing for multi-static target location," in *Proceedings of the 1st IEEE Sensor Array and Multichannel Signal Processing Workshop (SAM '00)*, (Cambridge, MA, USA, 2000) pp. 509–513.
36. S. K. Lehman and A. J. Devaney, "Transmission mode time-reversal super-resolution imaging," J. Acoust. Soc. Am. **113**(5), 2742–2753 (2003).
37. F. K. Gruber, E. A. Marengo, and A. J. Devaney, "Time-reversal imaging with multiple signal classification considering multiple scattering between the targets," J. Acoust. Soc. Am. **115**(6), 3042–3047 (2004).
38. C. Prada and J. L. Thomas, "Experimental subwavelength localization of scatterers by decomposition of the time reversal operator interpreted as a covariance matrix," J. Acoust. Soc. Am. **114**(1), 235–243 (2003).
39. P. C. Hansen, "Analysis of discrete ill-posed problems by means of the *L*-curve," SIAM Rev. **34**(4), 561–580 (1992).
40. E. A. Marengo, F. K. Gruber, and F. Simonetti, "Time-reversal MUSIC imaging of extended targets," IEEE Trans. Image Process. **16**(8), 1967–1984 (2007).
41. A. Ishimaru, "Diffusion of a pulse in densely distributed scatterers," J. Opt. Soc. Am. **68**(8), 1045–1050 (1978).
42. K. Furutsu, "Diffusion equation derived from the space-time transport equation," J. Opt. Soc. Am. **70**(4), 360–366 (1980).
43. M. S. Patterson, B. Chance, and B. C. Wilson, "Time resolved reflectance and transmittance for the non-invasive measurement of tissue optical properties," Appl. Opt. **28**(12), 2331–2336 (1989).
44. S. Chandrasekhar, *Radiative Transfer* (Clarendon Press, Oxford, 1950).
45. A. Ishimaru, *Wave Propagation and Scattering in Random Media, Volume 1: Single Scattering and Transport Theory* (Academic, New York, 1978).
46. S. R. Arridge and J. C. Schotland, "Optical tomography: forward and inverse problems," Inverse Probl. **25**(12), 123010 (2009).

47. S. R. Arridge, "Photon-measurement density functions. Part I: Analytical forms," Appl. Opt. **34**(31), 7395–7409 (1995).
48. R. C. Haskell, L. O. Svaasand, T.-T. Tsay, T.-C. Feng, M. S. McAdams, and B. J. Tromberg, "Boundary conditions for the diffusion equation in radiative transfer," J. Opt. Soc. Am. A **11**(10), 2727–2741 (1994).
49. M. Lax, V. Nayaramamurti, and R. C. Fulton, "Classical diffusion photon transport in a slab," in *Laser Optics of Condensed Matter*, J. L. Birman, H. Z. Cummins, and A. A. Kaplyanskii, eds. (Plenum, New York, 1987), pp. 229–237.
50. C. Prada, S. Manneville, D. Spoliansky, and M. Fink, "Decomposition of the time reversal operator: detection and selective focusing on two scatterers," J. Acoust. Soc. Am. **99**(4), 2067–2076 (1996).
51. A. J. Devaney, "Time reversal imaging of obscured targets from multistatic data," IEEE Trans. Antenn. Propag. **53**(5), 1600–1610 (2005).
52. N. Bourbaki, *Topological Vector Spaces* (Springer, 1987).
53. H. J. van Staveren, C. J. M. Moes, J. van Marie, S. A. Prahl, and M. J. C. van Gemert, "Light scattering in Intralipid-10% in the wavelength range of 400-1100 nm," Appl. Opt. **30**(31), 4507–4514 (1991).
54. C. Bordier, C. Andraud, E. Charron, J. Lafait, M. Anastasiadou, and A. Martino, "Illustration of a bimodal system in Intralipid 20% by polarized light scattering: experiments and modelling," Appl. Phys., A Mater. Sci. Process. **94**(2), 347–355 (2009).
55. S. D. Konecky, G. Y. Panasyuk, K. Lee, V. Markel, A. G. Yodh, and J. C. Schotland, "Imaging complex structures with diffuse light," Opt. Express **16**(7), 5048–5060 (2008).
56. M. Xu, Y. Pu, and W. Wang, "Clean image synthesis and target numerical marching for optical imaging with backscattering light," Biomed. Opt. Express **2**(4), 850–857 (2011).
57. T. Nielsen, B. Brendel, R. Ziegler, M. van Beek, F. Uhlemann, C. Bontus, and T. Koehler, "Linear image reconstruction for a diffuse optical mammography system in a noncompressed geometry using scattering fluid," Appl. Opt. **48**(10), D1–D13 (2009).
58. Y. Ardeshirpour, N. Biswal, A. Aguirre, and Q. Zhu, "Artifact reduction method in ultrasound-guided diffuse optical tomography using exogenous contrast agents," J. Biomed. Opt. **16**(4), 046015 (2011).
59. B. W. Pogue, M. S. Patterson, H. Jiang, and K. D. Paulsen, "Initial assessment of a simple system for frequency domain diffuse optical tomography," Phys. Med. Biol. **40**(10), 1709–1729 (1995).
60. S. Hou, K. Solna, and H. Zhao, "Imaging of location and geometry for extended targets using the response matrix," J. Comput. Phys. **199**(1), 317–338 (2004).
61. F. K. Gruber and E. Marengo, "Reinterpretation and enhancement of signal-subspace-based imaging methods for extended scatterers," SIAM J. Imaging Sci. **3**(3), 434–461 (2010).

1. Introduction

Optical imaging of targets embedded in a highly scattering turbid medium, such as, a tumor in a breast, is a challenging problem because light is strongly absorbed and scattered by the medium leading to poor signal-to-noise ratio, as well as, loss of phase coherence and polarization. As a consequence distinct, sharp image of the targets may not be formed directly. Various frequency-domain, time-resolved, and steady-state inverse image reconstruction (IIR) [1–5] approaches are being pursued to form tomographic images using diffusively scattered light measured at the sample boundary. IIR is an ill-posed problem and the development of reliable and fast approaches remains a formidable task. Recent IIR algorithms, such as Newton-Raphson-Marquardt algorithms [6] and direct linear inversion of 3-*D* matrices [7], are time consuming. The iterative methods [7,8] may not ensure that the obtained result arrives at a "global minimum" or converges to a "local minimum". Still the potential for developing non-invasive imaging approaches with diagnostic ability motivates the ongoing diffuse optical tomography (DOT) research using NIR light.

Many applications require rather accurate determination of location of target(s) in three dimensions. For example, a recent study involving 35,319 patients underscores the influence of primary tumor location on breast cancer prognosis [9], and makes it imperative that DOT for breast cancer detection be able to obtain three-dimensional (3-*D*) location of the tumor. While two-dimensional (2-*D*) IIR approaches may provide only lateral positions, 3-*D* IIR approaches attempt to retrieve all three position coordinates of the target(s). Various frequency-domain, time-domain, and steady-state DOT approaches have addressed the target localization problem with different measures of success [1–8]. Several groups have paid particular attention to retrieving target location. Kepshire *et al.* developed a subsurface DOT approach to obtain location information of absorbing and fluorescent targets, but observed the sensitivity to vary nonlinearly with depth [10]. Mohajerani *et al.* reported a fluorescent tomography method for locating fluorescent targets embedded in a heterogeneous medium using partitioning of the fluorophore distribution into an object subspace and a background

subspace [11]. Godavarty *et al.* developed another fluorescent tomography approach that used a hemispherical breast phantom, near-infrared light-induced fluorescence from a contrast agent, and finite element method-based reconstruction algorithms to obtain target information up to a depth of 2 cm from breast phantom surface [12]. Zhao *et al.* introduced a layer-based sigmoid adjustment method to improve depth resolution of DOT and achieved positioning error within 3 mm for depths from 10 to 30 mm [13]. Optical tomography using independent component analysis (OPTICA) approach developed by Xu *et al.* uses multi-source probing and multi-detector signal acquisition scheme and a numerical algorithm based on independent component analysis of information theory to obtain 3-*D* position information of absorbing, scattering and fluorescent targets embedded in highly scattering turbid media, and "model breast" assembled using *ex vivo* human breast tissue [14–17]. Co-registration approaches that use another modality, such as, ultrasound, magnetic resonance imaging, and x-ray mammography for locating suspect areas and DOT for obtaining images have also been introduced [18–21].

In this article we report on the development of a time reversal optical tomography (TROT) [22–24] approach for NIR optical imaging of target(s) in a turbid medium, and present initial results of its efficacy using both simulated and experimental data.

Time reversal (TR) invariance, the basic symmetry that commonly holds in microscopic physics, forms the basis for macroscopic TR imaging. TR imaging using the so-called "time-reversal mirrors" (TRMs) has been used as an experimental tool in acoustics with practical applications in medicine, underwater imaging, and nondestructive testing [25–28]. The theoretical and numerical techniques involved in time reversal have been used for applications involving both acoustic waves and electromagnetic waves (radar) [28–33].

Devaney and associates developed a theoretical framework for a TR imaging method with Multiple Signal Classification (MUSIC) for finding the location of scattering targets whose size is smaller than the wavelength of acoustic waves or electromagnetic waves (radar) used for probing the homogeneous or inhomogeneous background medium in which the targets were embedded [34,35]. While their initial focus was on *back-propagation geometry* that used coincident acoustic or electromagnetic transceiver array for interrogating the targets, they later extended the formalism to *transmission geometry* where sources and detectors were distinct and separated [36]. They also generalized the theory which was based on distorted wave Born approximation (DWBA) to account for multiple scattering between the targets [37]. In its basic form TR-MUSIC found target location from knowledge of the response matrix K, which was constructed from multi-static data collected by the transceiver array [34,35]. TR-MUSIC provided higher spatial resolution than the conventional TR imaging, especially in the case where targets were not well resolved [34,35,38].

We are adapting and extending the TR-MUSIC approach to the optical domain, *i.e.* to diffusive optical imaging for detecting and locating targets embedded in a turbid medium. In this paper, TROT is studied in details using both simulated data and data from transillumination NIR imaging experiments in slab geometry. A TR matrix is obtained by multiplying the response matrix formed using experimental or simulated data to its conjugate matrix. The leading non-zero eigenvalues of the Hermitian TR matrix determine the signal subspace due to presence of the targets. The signal subspace is separated from the noise subspace using an *L*-curve method [5,39,40]. The vector subspace method, MUSIC, along with Green's functions calculated from an appropriate forward model for light propagation through the turbid medium is then used to determine the locations of the targets. The MUSIC algorithm judges if the calculated Green's function vector corresponding to a location in the sample is mapped into the signal subspace or the noise subspace.

Several salient features make TROT attractive and potentially more promising than other IIR methods. First the size of the TR matrix is much smaller than those used in other IIR approaches, which makes solution of the eigenvalue problem easier and faster. Second, to determine locations of targets, TR-MUSIC approach runs the program over all voxels only once, and there is no need to carry out an iterative procedure done by other inverse approaches. Other IIR approaches seek to determine the absorption and scattering parameters

at all voxels into which the sample is divided. The process is iterative, computationally intensive, and leads to a solution of the inverse problem that is not unique because the problem is ill-posed, even when there is no noise. In contrast, TROT seeks to determine the locations of the targets first and thereafter retrieve other information, such as, the size and optical properties of the limited number of targets in the medium, which requires significantly less computation time. The focus of this paper is on finding the locations of targets.

Our result using simulated data shows that without the presence of noise TROT determines the locations of the embedded targets accurately with high resolution. TROT exhibits promise to locate targets both in simulations and experiments even when substantial noise is present. Images of small targets obtained by this approach are sharper than that obtained by other IIR approaches.

This paper is organized as follows. In section 2, the formalism of the TROT approach is presented. In section 3, the numerical algorithm of TROT is described. In section 4, the efficacy of the formalism is tested using simulated data. Section 5 presents the results when the formalism is applied to experimental data using Intralipid-20% suspension in water as the highly scattering turbid medium. Section 6 discusses the results.

2. Formalism

2.1 Diffusion approximation, perturbation method and response matrix

The starting point for the TROT formalism is the diffusion approximation [41–43] of the radiative transfer equation (RTE) [44,45]. The perturbation in the light intensity distribution due to small inhomogeneities (targets) embedded in a homogeneous medium, to the first order Born approximation, can be written as [46,47]

$$
\Delta\phi\left(r_d,r_s\right) = -\int G(r_d,r)\delta\mu_a(r)cG\left(r,r_s\right)d^3r
$$
$$
- \int \delta D(r)c\nabla_r G(r_d,r)\cdot\nabla_r G(r,r_s)d^3r, \qquad (1)
$$

where r_s, r_d, and r are the positions of a point-like source of unit power, detector and target, respectively; $G(r,r_s)$ and $G(r_d,r)$ are the Green's functions that describe light propagations from the source to the target and from the target to the detector, respectively; $\delta\mu_a$ is the difference in absorption coefficient and δD is the difference in diffusion coefficient between the targets and the background medium; and c is the light speed in the medium.

A multi-source interrogation and multi-detector signal acquisition scheme is used to acquire transillumination data, from which the difference in the light intensity distribution due to the targets, $\Delta\phi = \phi - \phi_0$, is found, where ϕ is the light intensity distribution measured on the sample boundary with targets embedded in the scattering medium and ϕ_0 is ideally the light intensity distribution without the targets, which in practice is approximated by an "average" over all the multi-source measurements. A response matrix K is constructed with $-\Delta\phi$, to describe the transport of light from different sources through the embedded objects to the array of detectors [22,36].

For small, point-like absorptive targets, the matrix elements can be rewritten in a discrete form as:

$$
K_{ij} = \sum_{m=1}^{M} G^d\left(r_i,X_m\right)\tau_m G^s\left(X_m,r_j\right), i=1,2,\cdots,N_d; j=1,2,\cdots,N_s, \qquad (2)
$$

where $\tau_m = \delta\mu_a(X_m)c\delta V_m$ is the optical absorption strength of the mth target, δV_m is the volume of mth target, r_i, r_j and X_m are locations of the ith detector, j^{th} source and m^{th} target, respectively. Due to the reciprocity of light propagation in the medium, $G(r,r') = G(r',r)$. Thus,

$$K_{ij} = \sum_{m=1}^{M} G^d \left(\boldsymbol{X}_m, \boldsymbol{r}_i \right) \tau_m G^s \left(\boldsymbol{X}_m, \boldsymbol{r}_j \right), \tag{3}$$

and

$$K = \left\{ K_{ij} \right\} = \sum_{m=1}^{M} g_d \left(\boldsymbol{X}_m \right) \tau_m g_s^{\ T} \left(\boldsymbol{X}_m \right), \tag{4}$$

where $g_s(\boldsymbol{r})$ and $g_d(\boldsymbol{r})$ are Green's function vectors (GFVs) associated with the source array and detector array, respectively. GFVs are defined as

$$g_s \left(\boldsymbol{r} \right) = [G^s \left(\boldsymbol{r}_1, \boldsymbol{r} \right), G^s \left(\boldsymbol{r}_2, \boldsymbol{r} \right), \cdots, G^s \left(\boldsymbol{r}_{N_s}, \boldsymbol{r} \right)]^T, \tag{5a}$$

$$g_d \left(\boldsymbol{r} \right) = [G^d \left(\boldsymbol{r}_1, \boldsymbol{r} \right), G^d \left(\boldsymbol{r}_2, \boldsymbol{r} \right), \cdots, G^d \left(\boldsymbol{r}_{N_d}, \boldsymbol{r} \right)]^T, \tag{5b}$$

where the superscript T denotes transpose; and N_s, N_d and M are the numbers of sources, detectors and targets, respectively. It is assumed the number of targets is less than the number of sources and detectors, $M < \min(N_d, N_s)$. It also holds that $K^T = \{K_{ji}\}$ describes light propagation from the positions of detectors through the medium and targets to sources.

For a homogeneous background medium, the rank R of matrix K, is equal to the dimension of the source array vector space $\mathcal{G}_s$ spanned by $g_s(\boldsymbol{r}_m)$, and also equal to the dimension of the detector array vector space $\mathcal{G}_d$ spanned by $g_d(\boldsymbol{r}_m)$, where $\mathcal{G}_s \subseteq C^{N_s}$ and $\mathcal{G}_d \subseteq C^{N_d}$. For absorptive targets, R is equal to the number of targets M.

Similar forms of the response matrix and GFVs can be obtained for scattering targets. As the dot product in the second term of Eq. (1) implies, each scattering target is represented by three components coexisting at one location. The elements of the K matrix for L scattering target may be written as

$$K_{ij} = \sum_{l=1}^{L} \tau_l \nabla_{\boldsymbol{r}} G^d \left(\boldsymbol{r}_i, \boldsymbol{X}_l \right) \cdot \nabla_{\boldsymbol{r}} G^s \left(\boldsymbol{X}_l, \boldsymbol{r}_j \right)$$

$$= \sum_{l=1}^{L} \tau_l \sum_{\alpha = \{x,y,z\}} \partial_\alpha G^d \left(\boldsymbol{r}_i, \boldsymbol{X}_l \right) \partial_\alpha G^s \left(\boldsymbol{X}_l, \boldsymbol{r}_j \right), \tag{6}$$

where $\tau_l = \delta D(\boldsymbol{X}_l) c \delta V_l$ is the optical scattering strength of the lth target. The K matrix for scattering targets can be written in a manner similar to that for absorptive targets:

$$K = \sum_{l=1}^{L} \sum_{\alpha = \{x,y,z\}} \partial_\alpha g_d \left(\boldsymbol{X}_l \right) \tau_l \partial_\alpha g_s^{\ T} \left(\boldsymbol{X}_l \right). \tag{7}$$

The Green's function for a slab geometry is [16,47]

$$G(\boldsymbol{r}, \boldsymbol{r}') = G(\boldsymbol{r}', \boldsymbol{r}) = \frac{1}{4\pi D} \sum_{k=-\infty}^{\infty} \left(\frac{e^{-\kappa r_k^+}}{r_k^+} - \frac{e^{-\kappa r_k^-}}{r_k^-} \right), \tag{8a}$$

$$r_k^{\pm} = \left[(x-x')^2 + (y-y')^2 + (z \mp z' + 2kd)^2 \right]^{1/2}, \tag{8b}$$

where $\kappa = \left[(\mu_a - i\omega/c)/D \right]^{1/2}$ in frequency domain with amplitude modulation frequency ω, and $k = 0, \pm1, \pm2, \cdots$. The extrapolated boundaries of the slab are located at $z = 0$ and

$z = d = L + 2z_e$, respectively, where L is the physical thickness of the slab and the extrapolation length z_e is determined from the boundary condition of the slab [48,49].

Under ideal conditions, when all three scattering components of each of the L scattering targets are well-resolved, the rank of K contributed by L scattering targets is $3L$. In practice, four components (one for absorption and three for scattering) are calculated for each target, since the targets may have both scattering and absorptive characteristics, or the exact nature may not be known *a priori*. The dominant characteristic is used to label the target as absorptive or scattering in nature.

2.2 Point Spread Functions

If light emitted by a source of unit power at target position X propagates in the sample medium, the signal measured by the detector array at the sample boundary is $G^d(r_i, X)$. The signal is then "time-reversed" and back-propagated with the Green's function of the background medium. TR operation is phase conjugation in Fourier domain [28,50]. So the signal evaluated at r is [34]

$$H_d(r, X) = \sum_{i=1}^{N_d} G^d(r, r_i) G^{d*}(r_i, X) = g_d^T(r) g_d^*(X)$$
$$= g_d^\dagger(X) g_d(r) = \langle g_d(X), g_d(r) \rangle, \tag{9}$$

where $*$ denotes phase conjugate, $\dagger$ denotes adjoint, and $\langle \cdot \rangle$ denotes inner product. $H_d(r, X)$ is the detector array point spread function (PSF). A source array PSF can be similarly formed as

$$H_s(r, X) = g_s(X)^\dagger g_s(r) = \langle g_s(X), g_s(r) \rangle. \tag{10}$$

Due to the time reversal assumption, $H_d(r, X)$ peaks at $r = X$, so it can be considered as an image of the source at X formed by the TR detector array. PSF vanishes when r is far away from X. A similar interpretation can be used for $H_s(r, X)$.

2.3 Time reversal and MUSIC

The TR matrix may be constructed to represent light propagation from sources to detectors and back denoted by T_{SDDS}, or to represent light propagation from detector positions to source positions and back denoted by T_{DSSD}, a consequence of the reciprocity of light propagation [29,34,38,50,51]. For frequency-domain data, $T_{SDDS} = K^\dagger K$, and $T_{DSSD} = (K^T)^? K^T = K\ K^T$, where response data matrix K is formed using modulated intensities, instead of the field with phase information used in the conventional TR. For CW measurements, $T_{SDDS} = K^T K$, and $T_{DSSD} = KK^T$ (K is real and only includes intensity values).

Since T_{SDDS} and T_{DSSD} are Hermitian ($T^\dagger = T$), they have complete sets of orthonormal eigenvectors v_j ($j = 1, \cdots, N_s$) and u_i ($i = 1, \cdots, N_d$), with a common set of non-negative real eigenvalues. For $M < \min(N_s, N_d)$ absorptive targets without the presence of noise, the rank of T_{SDDS} and T_{DSSD} is M. The eigenvalues $\lambda_j > 0$, when $j = 1, \cdots, M$, and $\lambda_j \approx 0$, when $j = M+1, \cdots, N_s$ for T_{SDDS} and $j = M+1, \cdots, N_d$ for T_{DSSD}. The eigen system $\{v_j, u_j, \lambda_j > 0\}$, $j = 1, \cdots, M$, is related to the targets. The TR matrix T_{SDDS} can be written as [22,34]

$$T_{SDDS} = \sum_{m=1}^{M} \sum_{m'=1}^{M} \tau_m^* \tau_{m'} \langle g_d(X_m), g_d(X_{m'}) \rangle g_s^*(X_m) g_s^T(X_{m'}). \tag{11}$$

Subsequent formalism may be different depending on whether the targets are "well resolved" or "poorly resolved."

2.3.1 Well-resolved targets

If the mth and m'^{th} targets ($m \neq m'$) are well resolved, defined by the conditions: $H_s(X_m, X_{m'}) \approx 0$ and $H_d(X_m, X_{m'}) \approx 0$, i.e. the GFVs at X_m and $X_{m'}$ are orthogonal, $< g_d(X_m), g_d(X_{m'}) >= H_d(X_{m'}, X_m) = \|g_d(X_m)\|^2 \delta_{mm'}$. So we have

$$T_{SDDS} = \sum_{m=1}^{M} |\tau_m|^2 \|g_d(X_m)\|^2 g_s^*(X_m) g_s^T(X_m), \tag{12}$$

where $\|\cdot\|$ denotes $L2$ norm [52]. The eigenvectors of T_{SDDS} are proportional to the phase conjugate of the GFVs associated with the M targets [22,34], i.e.

$$T_{SDDS} g_s^*(X_m) = |\tau_m|^2 \|g_d(X_m)\|^2 \|g_s(X_m)\|^2 g_s^*(X_m). \tag{13}$$

The eigenvectors are

$$v_j = \frac{g_s^*(X_j)}{\|g_s(X_j)\|}, \tag{14}$$

with eigenvalues $\lambda_j = |\tau_j|^2 \|g_d(X_j)\|^2 \|g_s(X_j)\|^2$, $j = 1, \cdots, M$. Thus T_{SDDS} is a projection operator that projects a vector onto the conjugate of the source array vector space $\mathcal{G}_s$. The jth non-zero eigenvalue λ_j is directly related to the optical strength τ_j of the jth target. Similar equations can be derived for T_{DSSD}, which is a projection operator for the conjugate of the detector array vector space $\mathcal{G}_d$. The eigenvectors of T_{DSSD} are

$$u_j = \frac{g_d^*(X_j)}{\|g_d(X_j)\|}, \tag{15}$$

$j = 1, \cdots, M$, with the same eigenvalues as T_{SDDS}.

Therefore, for well-resolved targets, the target locations can be determined by the inner product [22,34,36,51]

$$\psi_j^s = \langle v_j^*, g_s(X_p) \rangle = v_j^T g_s(X_p) = \frac{g_s^\dagger(X_j)}{\|g_s(X_j)\|} g_s(X_p)$$

$$= \frac{1}{\|g_s(X_j)\|} H_s(X_p, X_j), \tag{16a}$$

or

$$\psi_j^d = \langle u_j^*, g_d(X_p) \rangle = u_j^T g_d(X_p) = \frac{g_d^\dagger(X_j)}{\|g_d(X_j)\|} g_d(X_p)$$

$$= \frac{1}{\|g_d(X_j)\|} H_d(X_p, X_j), \tag{16b}$$

where X_p is a test target position, which is the position of any voxel in the sample space. ψ_j^s and ψ_j^d peak when X_p is the position of the jth target. In the classical TR imaging

[25,29,38,50], for ideally resolved targets, each eigenvector of the TR operator can be used to focus on one particular target. Here ψ_j^s and ψ_j^d represent focusing of signals from the source and detector planes on to the target position, respectively. Use of the eigenvectors v_j and u_j, $j = 1, \cdots, M$, ensures that the jth target is sorted out. When T_{SDDS} and source array vector space (T_{DSSD} and detector array vector space) are used, we call the scheme SDDS (DSSD). Both source and detector arrays can be considered simultaneously to locate the target by calculating

$$\psi_j = \psi_j^d \psi_j^{s\dagger} = \frac{1}{\left\| g_s\left(X_j\right)\right\| \cdot \left\| g_d\left(X_j\right)\right\|} H_d\left(X_p, X_j\right) H_s^*\left(X_j, X_p\right), \qquad (17)$$

$j = 1, \cdots, M$, which is computationally equivalent to a process that light emitted from a virtual source of unit power at a test target position X_p, propagates to the TR source array and back to a true target position X_j; then it is re-emitted and further propagates to the TR detector array and back to the original position X_p. ψ_j peaks when the test target position X_p coincides with the true target position X_j associated with the jth eigenvector.

2.3.2 Poorly-resolved Targets and MUSIC

When the targets are too close to each other or the sources and/or detectors are significantly sparse, the targets are considered to be poorly resolved and the GFVs at X_m and $X_{m'}$ are not orthogonal. In such cases, the eigenvectors v_j and u_j do not correspond one-to-one with the GFVs associated with target positions X_m ($j, m = 1, \cdots, M$). The image resolution degrades because of contributions from multiple targets. To solve this problem, the subspace-based method, MUSIC was implemented with TR [34,36,51]. MUSIC algorithm is based on the idea that although the vectors characterizing the targets are no longer orthogonal with each other, they are all located in the signal subspace, which is orthogonal to the noise subspace.

The orthonormal sets $\{v_j^*\}$ ($j = 1, \cdots, N_s$) and $\{u_j^*\}$ ($j = 1, \cdots, N_d$) span the spaces C^{N_s} and C^{N_d} associated with the source and detector arrays, respectively. While $\{v_j^*\}$ and $\{u_j^*\}$, with $\lambda_j > 0$, form the signal subspaces on the source and detector arrays, $\mathcal{S}^s = \{v_j^*\}$ and $\mathcal{S}^d = \{u_j^*\}$ ($j = 1, \cdots, M$), respectively; $\{v_j^*\}$ and $\{u_j^*\}$, with $\lambda_j \approx 0$, form the noise subspaces, $\mathcal{N}^s = \{v_j^*\}$ ($j = M+1, \cdots, N_s$) and $\mathcal{N}^d = \{u_j^*\}$ ($j = M+1, \cdots, N_d$), respectively. Thus $C^{N_s} = \mathcal{S}^s \oplus \mathcal{N}^s$ and $C^{N_d} = \mathcal{S}^d \oplus \mathcal{N}^d$ [36,51]. Since the dimensions of the signal subspaces $\mathcal{S}^s$ and $\mathcal{S}^d$ and of the GFV spaces $\mathcal{G}_s$ and $\mathcal{G}_d$ are all equal to M, $\mathcal{G}_s \equiv \mathcal{S}^s$ and $\mathcal{G}_d \equiv \mathcal{S}^d$ [51]. The GFVs, $g_s(X_m)$ and $g_d(X_m)$, $m = 1, \cdots, M$, are linear combinations of v_j^* and u_j^*, $j = 1, \cdots, M$, respectively. Therefore, $g_s(X_m) \in \mathcal{S}^s$ and $g_d(X_m) \in \mathcal{S}^d$, $m = 1, \cdots, M$, associated with m^{th} target are orthogonal to $v_j^* \in \mathcal{N}^s$ ($j = M+1, \cdots, N_s$) and $u_j^* \in \mathcal{N}^d$ ($j = M+1, \cdots, N_d$), respectively:

$$\left\langle v_j^*, g_s\left(X_m\right)\right\rangle = v_j^T g_s\left(X_m\right) \approx 0, \, j = M+1, \cdots, N_s, \qquad (18a)$$

$$\left\langle u_j^*, g_d\left(X_m\right)\right\rangle = u_j^T g_d\left(X_m\right) \approx 0, \, j = M+1, \cdots, N_d. \qquad (18b)$$

The locations of targets can be determined by calculating the following squared sum of inner products:

$$Q_s(X_p) = \sum_{j=M+1}^{N_s} \left| v_j^T g_s\left(X_p\right)\right|^2, \qquad (19a)$$

$$Q_d(\boldsymbol{X}_p) = \sum_{j=M+1}^{N_d} \left| u_j^T g_d(\boldsymbol{X}_p) \right|^2 . \tag{19b}$$

$Q_s(\boldsymbol{X}_p)$ and $Q_d(\boldsymbol{X}_p)$ vanish when the test target position $\boldsymbol{X}_p$ is a true target position. Similar to Eq. (17), $Q = Q_s Q_d$ can be calculated with both source and detector arrays considered simultaneously. An alternative approach to accentuate a target position is to plot a pseudo spectrum defined as

$$P_s(\boldsymbol{X}_p) = \left\| g_s(\boldsymbol{X}_p) \right\|^2 \Big/ \left| Q_s(\boldsymbol{X}_p) \right| \tag{20a}$$

associated with the source array, or

$$P_d(\boldsymbol{X}_p) = \left\| g_d(\boldsymbol{X}_p) \right\|^2 \Big/ \left| Q_d(\boldsymbol{X}_p) \right| \tag{20b}$$

associated with the detector array, or

$$P(\boldsymbol{X}_p) = P_s(\boldsymbol{X}_p) P_d(\boldsymbol{X}_p) \tag{20c}$$

associated with both source and detector arrays [22,34,36,51], where $\left\| g_s(\boldsymbol{X}_p) \right\|^2$ and $\left\| g_d(\boldsymbol{X}_p) \right\|^2$ are used for normalization. The poles of the pseudo spectrum correspond to target locations. These MUSIC pseudo spectra can also be used to locate well-resolved targets.

Since the dimension of the signal subspace is generally much smaller than that of the noise subspace, it is preferred that in Eq. (19) and Eq. (20), the signal subspace is used rather than the noise subspace for ease of computation. Using the properties of the projection operators associated with the source and detector arrays [22,34,36,51], $Q_s(\boldsymbol{X}_p)$ and $Q_d(\boldsymbol{X}_p)$ can be calculated as

$$Q_s(\boldsymbol{X}_p) = \left\| g_s(\boldsymbol{X}_p) \right\|^2 - \sum_{j=1}^{M} \left| v_j^T g_s(\boldsymbol{X}_p) \right|^2 , \tag{21a}$$

$$Q_d(\boldsymbol{X}_p) = \left\| g_d(\boldsymbol{X}_p) \right\|^2 - \sum_{j=1}^{M} \left| u_j^T g_d(\boldsymbol{X}_p) \right|^2 . \tag{21b}$$

When the targets are embedded in a non-uniform medium, or when there is significant noise present, the noise or false targets contribute significantly to the eigenvalues. The near-zero and non-zero eigenvalues are not as well separated as when there are no noise. In this case, the rank of the TR matrix is larger than the number of targets M. The TR matrix may even be full rank. However, as long as M is less than $\min(N_s, N_d)$ and eigenvalues contributed by the noise and false targets are smaller than those contributed by the real targets with a threshold ϵ, the target positions can be obtained using a pseudo spectrum [36,51] associated with the source array,

$$P_s(\boldsymbol{X}_p) = \left\| g_s(\boldsymbol{X}_p) \right\|^2 \Big/ \left| Q_s(\boldsymbol{X}_p)_{\lambda_j \le \epsilon} \right| , \tag{22}$$

where $Q_s(\boldsymbol{X}_p)_{\lambda_j \le \epsilon} = \left\| g_s(\boldsymbol{X}_p) \right\|^2 - \sum_{\lambda_j > \epsilon} \left| v_j^T g_s(\boldsymbol{X}_p) \right|^2$. Pseudo spectra associated with the detector array or with both source and detector arrays can also be obtained similarly. In practice, the threshold is selected to separate the signal and noise subspaces using a method similar to L-curve regularization [39].

When scattering targets are concerned, the GFVs $\partial_\alpha g$ ($\alpha = x, y, z$), associated with the test target position X_p will be used to calculate the pseudo spectrum. For a target with both absorption and scattering properties at the wavelength of probing light, one GFV corresponding to absorption constructed as g and three GFVs corresponding to scattering target constructed with $\partial_\alpha g$, ($\alpha = x, y, z$), are used to calculate the pseudo spectrum over every voxel. Ideally, for an absorptive and scattering target four pseudo-values will be obtained for every target position. If the dominant value corresponds to the absorptive (any of the scattering) GFV the target will be identified as absorptive (scattering) in nature.

3. Algorithm

Implementation of TROT to locate targets embedded in a highly scattering turbid medium involves the steps outlined below. For simplicity, the sizes of source array and detector array are assumed to be the same, *i.e.*, $N_d = N_s = N$.

(a) A response matrix K with size $N \times N$ is constructed using experimental data (or estimated data in simulation). Data consist of the perturbations in the light intensity distribution due to the targets, $\Delta\phi = \phi - \phi_0$, where ϕ is the light intensity distribution measured on the sample boundary with targets embedded in the scattering medium and ϕ_0 is ideally the light intensity distribution without the targets. In practice, ϕ_0 is approximated by an "average" over all the multi-source measurements, while in simulation it can be estimated without such approximation.

(b) A detector array TR matrix, $T_{DSSD} = KK^T$ with size $N \times N$ for CW measurements is constructed. All the eigenvalues and the eigenvectors of the T_{DSSD} matrix are computed. The eigenvectors are orthogonal to each other. It is to be noted that in this procedure we only deal with a matrix of dimension N, not a matrix of dimension of $N \times N$ as done in traditional inverse procedures.

(c) The non-zero eigenvalues of T_{DSSD} belonging to the signal subspace are separated from the near-zero eigenvalues belonging to the noise subspace using the *L*-curve method [5,39,40].

(d) MUSIC approach [34,36,51] is next used to determine the locations of the targets as follows. (i) The 3-*D* medium is divided into a certain number of voxels. A detector array GFV, $g_d(X_p)$, associated with an absorptive test target position X_p at p^{th} voxel is calculated using Diffusion Approximation of RTE. Other proper forward models could be used as well. In order to check if $g_d(X_p)$ is located in the signal subspace or in the noise subspace, a pseudo spectrum associated with the detector array is computed using Eq. (20b), where *M* is the dimension of the signal subspace found in step (c). If $g_d(X_p)$ is located in the signal subspace, the corresponding pseudo value $P(X_p)$ in Eq. (20b) will become a maximum. (ii) Pseudo spectra are also calculated using the other three GFVs, $\partial_\alpha g_d(X_p)$, ($\alpha = x, y, z$) for scattering property. (iii) All pseudo values are put together and sorted in a descending order. Since the leading pseudo values at X_p are associated with targets and specific GFVs, the positions of the embedded targets and their nature (absorptive or scattering) are determined. The pseudo spectrum in the whole sample space can be used to plot pseudo tomographic images.

In this approach, only a single run is needed for calculating the pseudo spectrum and no iterative procedure is involved, which makes it faster and computationally less intensive than the traditional IIR approaches. Similar procedure can be used for application of TROT when

$N_d \neq N_s$. The pseudo spectrum associated with either the source array, or the detector array, or both source and detector arrays, as outlined in Eq. (20) can be used to obtain target positions.

It is instructive to compare the computational complexity of TROT formalism with that of typical iterative methods. For a typical iterative method, an equation $b = Wx$ is solved to find the inhomogeneities (targets), where W is a weight matrix with size $N_dN_s \times N$, N is the number of voxels, b is an $N_dN_s \times 1$ vector describing the perturbation in the detected light intensity due to the presence of inhomogeneities, and x is the perturbation or variation in the optical properties from the background values with dimension of $N \times 1$. The computational complexity is typically $O(N_dN_sN^2)$ for a single iteration. The computational complexity of TROT is much smaller than that for even one iteration of an iterative method. For the SDDS scheme, the complexity for TROT is $O(N_dN_s^2)$ if $N_dN_s > NN_k$, and $O(N_sNN_k)$ otherwise, where N_k is the dimension of the signal subspace. In the DSSD scheme, the complexity is $O(N_sN_d^2)$ if $N_dN_s > NN_k$, and $O(N_dNN_k)$ otherwise. TROT does not involve any iteration.

In the following sections, TROT will be tested using simulation and experimental data.

4. Testing TROT with simulated data

To test the efficacy of the TROT approach, we first consider a rather challenging task of detecting and locating six targets embedded in a simulated sample which is a 40-mm thick uniform scattering slab. Its absorption and diffusion coefficients are μ_a = 1/300 mm^{-1} and D = 1/3 mm, respectively. The incident CW beam was step-scanned in an x-y array of 41 × 41 grid points with a step size of 2 mm on the input plane covering an 80 mm × 80 mm area. Light transmitted from the opposite side (output plane) was recorded at 41 × 41 grid points covering the same area. No random noise was added.

The six (M = 6) point-like absorptive targets, with absorption coefficient difference of $\Delta\mu_a$ = 0.01 mm^{-1} from the background, were placed at A (24 mm, 26 mm, 9 mm), B (38 mm, 38 mm, 15 mm), C (38 mm, 38 mm, 21 mm), D (40 mm, 38 mm, 21 mm), E (44 mm, 42 mm, 21 mm) and F (30 mm, 30 mm, 31 mm), respectively. The origin (0 mm, 0 mm, 0 mm) was located at the upper-left corner of the input boundary (source plane) of the sample. The medium was divided into 40 × 40 × 20 voxels, with each voxel of size 2 mm × 2 mm × 2 mm. As can be seen from the assigned coordinates, targets C and D are located at two adjacent voxels, and are close to target E, and these three targets are located in the same z layer. Consequently, targets C and D are expected to be very difficult to resolve, and hard to distinguish from target E. Target B and C have the same lateral position x and y, and different depths. Target A is close to the source plane, while F is close to the detector plane.

Using the Diffusion Approximation of the RTE as the model for light propagation in slab geometry, signals arising from light propagation from the source array to the detector array through medium *with* and *without* the targets were calculated. The difference between the two sets, which is the perturbation due to the targets, was used as the "simulated data". The size of the K matrix is $N \times N$ = 1681 × 1681. The TR matrix $T = KK^T$ was constructed. Then, 1681 eigenvalues and 1681 eigenvectors of T were found.

The first seven (7) computed eigenvalues in a descending order of magnitude are listed in the first column of Table 1. The leading twenty eigenvalues are plotted in Fig. 1(a) on a logarithmic scale. The first six (6) eigenvalues are at least 10 orders-of-magnitude higher than the 7-th and other smaller eigenvalues. Hence, the dimension of the signal subspace and the number of targets are determined to be six. The pseudo spectrum (consisting of 40 × 40 × 20 × 4 elements) was calculated using the M eigenvectors in the signal subspace. The values of elements in the pseudo spectrum were sorted in a descending order. The seven leading pseudo values are listed in Table 1 with the corresponding positions of voxels. The six peaks are found to be associated with the GFVs for absorptive targets. Namely, the corresponding six targets are identified to be absorptive targets.

All six large pseudo-values are located at the exact known target locations and their values are approximately 9 orders-of-magnitude larger than those at their neighborhood locations. A

2-*D* slice of the pseudo spectrum on $z = 21$ mm plane is shown in Fig. 1(b), showing the locations of the three difficult targets.

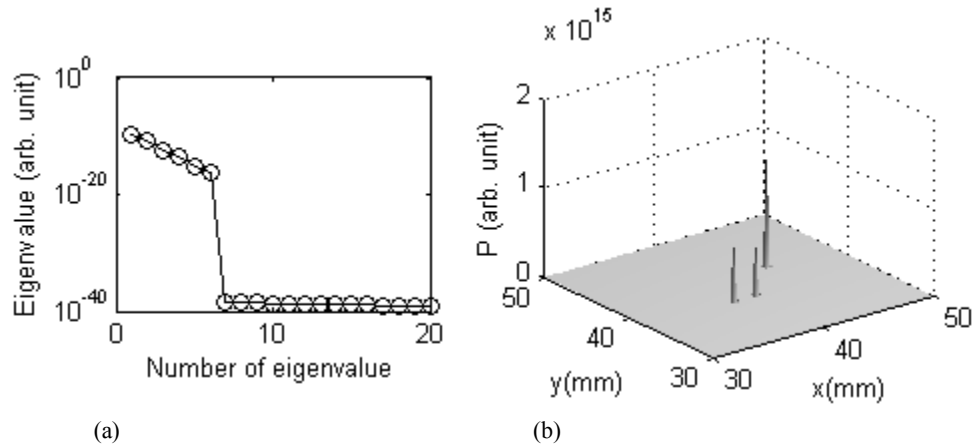(a)   (b)

Fig. 1. (a) A plot of first twenty (20) eigenvalues on logarithmic scale. (b) 2-*D* slice of the pseudo spectrum on $z = 21$ mm plane showing the location of the three difficult targets described in the text. Similar 2-*D* slices were also obtained for $z = 9$-mm, 15-mm, and 31-mm planes (not shown).

Table 1. Eigenvalues, pseudo spectrum and the corresponding positions

Leading Eigenvalues	Poles of Pseudo Spectrum	Retrieved Position (x, y, z) mm	Known Position (x, y, z) mm
2.6697E-010	1.5911E + 015	(44, 42, 21)	(44, 42, 21)
1.1722E-011	8.6376E + 014	(38, 38, 15)	(38, 38, 15)
4.0081E-013	7.9559E + 014	(38, 38, 21)	(38, 38, 21)
3.6676E-014	7.2328E + 014	(40, 38, 21)	(40, 38, 21)
5.2629E-016	6.3010E + 014	(24, 26, 9)	(24, 26, 9)
6.4837E-017	2.1159E + 014	(30, 30, 31)	(30, 30, 31)
2.8337E-039	2.4353E + 005	(38, 38, 19)	
…	…		

With the highly encouraging result from simulation even for a considerably challenging task, we proceeded to test the approach for the realistic situation of detecting and locating targets from experimental data.

5. Testing TROT using Experimental Data

5.1 Experimental materials and methods

Three different experiments with three different samples were carried out to test the efficacy of the TROT approach in detecting and locating targets in a turbid medium. All three samples used a 250 mm × 250 mm × 60 mm transparent plastic container filled with Intralipid-20% suspension in water as the background medium. The concentration of Intralipid-20% was adjusted to provide an estimated [53,54] absorption coefficient μ_a ~0.003 mm^{-1} at 790 nm, and a transport mean free path l_t ~1 mm, which were similar to the average values of those parameters for human breast tissue, while the cell thickness of 60 mm was comparable to thickness of a typical compressed breast.

In the first experiment, the depth (position along *z*-axis) of an absorptive target was varied to explore how the accuracy of position estimate depended on depth. The target was a glass sphere of diameter ~9 mm filled with ink dissolved in Intralipid-20% suspension in water (μ_s was adjusted to be the same as that of the background medium, while $\mu_a \approx 0.013$ mm^{-1} was about 3 times higher than that of background medium).

In the second experiment, the separation between two absorptive targets was varied to test how close those could be and yet be resolved as separate objects. Both the targets were similar to the target in the first experiment.

In the third experiment, the depth of a scattering target was varied to explore the efficacy of TROT in locating and characterizing a scattering target. The target was a glass sphere of diameter 10 mm filled with Intralipid-20% suspension in water to provide a transport mean free path l_t of 0.25 mm, and a scattering coefficient $\mu_s \approx 11$ mm^{-1}.

A multi-source interrogation and multi-detector signal acquisition scheme, shown in Fig. 2, was used to acquire data. A 100-mW 790-nm diode laser beam was used to illuminate the samples. A 1024 × 1024 pixels charge coupled device (CCD) camera equipped with a 60-mm focal-length camera lens was used on the opposite side of the sample to detect the transmitted light on the boundaries of the slab samples (detector plane). The pixel size was 24 μm. The multi-source illumination scheme was realized by scanning the sample across the laser beam in a two-dimensional x-y array of grid points using a computer-controlled translation stage. The first and third samples were scanned across the laser beam in an array of 9 × 9 grid points, and the second sample was scanned in an array of 15 × 11 grid points, with a step size of 5 mm in all cases. The scanning and data acquisition processes were controlled by a personal computer (PC). Raw transillumination images of the sample were recorded by the PC for each scan position, and stored for subsequent analysis. A typical image, which is a 2-D intensity distribution, is shown in the right side of Fig. 2.
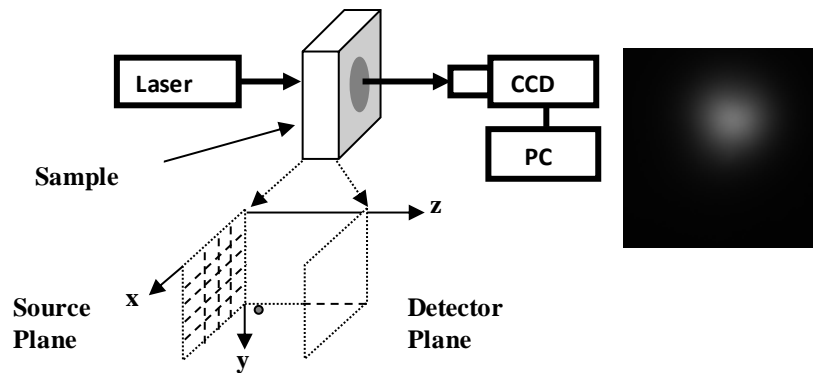

Fig. 2. A schematic diagram of the experimental arrangement for imaging objects embedded in a turbid medium. (Key: CCD = charge coupled device, PC = personal computer) Inset (below) shows the 2-D array in the input plane that was scanned across the incident laser beam, and inset (right) shows a typical raw image.

While we have scanned the sample and kept the source fixed in the experiments reported here, a more clinically relevant approach would be to scan the source and fix the sample. In the experimental arrangement, the source scanning may be accomplished by: (a) delivering the beam using an optical fiber, and translating the delivery end of the fiber in an x-y array using a computer-controlled translation stage; or (b) raster scanning the laser beam using two orthogonal (x-y) galvanometers. The main change in the processing of data would involve alignment of the images so that laser beam positions are overlapped before averaging to generate the background image.

5.2 Data Processing and Analysis

From each image, a region of interest was cropped out and then every 5 × 5 pixels in the cropped image were binned to one pixel to enhance the signal-to-noise ratio. The background image was generated by taking an average of the original images for all scan positions, which is a reasonable approximation since for most of the scan positions the target(s) is (are) not along the direction of the incident beam. Then the background image was also cropped and binned corresponding to the region of interest for each scan position. Perturbation in the light

intensity distribution $\Delta\phi$ due to targets in each image was found by subtracting the background image from each individual image. The response matrix was constructed using the light intensity perturbations, $-\Delta\phi$. The TR matrix was generated by multiplying the response matrix by its transpose for our continuous-wave (CW) probing scheme. The eigenvalue equation was solved and the signal subspace was selected and separated from the noise subspace. MUSIC was then used to calculate the pseudo spectrum for all voxels in the 3-*D* space of the sample. For each voxel, four pseudo values, one for absorption and three for scattering as described in Algorithm step (d), were calculated. The voxel size was 0.77 mm × 0.77 mm × 1 mm. By sorting the pseudo spectrum in a descending order, the target(s) were located.

The voxel size to be used in reconstruction and its relation to the target size is an important consideration. In general, smaller voxels provide reconstruction of higher resolution at the cost of increased computational time. Finer details of an extended target may be obtained using smaller voxels. Decreasing the voxel size indefinitely may not improve resolution because of the diffusive nature of light propagation in the turbid medium. However, the computation time increases dramatically, which has been observed by other researchers [55]. The optimal voxel size for a given reconstruction problem will depend on factors, such as, target size, experimental geometry, and noise level.

Since the signal used in image reconstruction is taken to be the difference between the image recorded for a scan position and the background image, estimation of the background image is an important issue. This is a common problem for every diffuse optical imaging modality using perturbation method, and needs further elaboration. We accumulated data in the transillumination slab geometry, and generated the background image by averaging images for all scan positions after proper alignment with respect to the incident source position. This averaging method for generating background image worked well for small targets that we used in our experiments, as the ratio of sample volume to target volume was quite high (~500:1). This volume ratio for breast and a tumor in early stages of growth will also be substantially high for the averaging method to be applicable. Assuming a scenario where the volume ratio is substantially smaller than in above examples, a modified approach would be to select recorded images which were minimally affected by embedded targets for averaging [56]. As long as the targets only occupy a limited volume within the host medium, a clean background image can be generated in this fashion. It should also be noted that while estimation of target optical properties, such as absorption coefficient and scattering coefficient, are sensitively dependent on background image estimation, estimation of target positions are not so sensitive.

Several alternative ways of generating background image are suggested in the literature. One experimental approach is to record image using a phantom that has the same average optical properties as the sample, such as human breast [57]. Along the same line, image of the healthy contralateral breast taken under the same experimental conditions as that of the suspect breast may be used as background image for breast imaging [58]. Some authors have suggested acquiring data at a wavelength for which the target(s) and the background have identical optical properties for assessing the background, *e.g.,* measurement using 805-nm light for which hemoglobin and oxyhemoglobin have the same absorption coefficient may serve as background to image hemoglobin oxygenation [59]. Still another approach is to compute the background using an appropriate forward model [18]. Any of these approaches may be employed for generating the background image for use with the TROT formalism presented here.

The geometries commonly used in DOT include slab, cylindrical, hemispherical, and semi-infinite; and different source-detector combinations have been used to record images in these geometries. As long as multiple source-detector combinations provide multiple angular views of the sample the TROT formalism can be adapted to obtain target location for these geometries. TR imaging and TR-MUSIC was originally developed for reflection (backscattering) geometry that used coincident transceiver array to detect the return signal

[28–30,34,35]. With requisite modification in the experimental arrangement TROT would be suited for use in the reflection geometry.

5.3 Results

5.3.1 Single absorptive target at different depths

In the first experiment, only one target was used, the lateral (x, y) position of the target was kept the same at (25.5 mm, 24.7 mm), while seven different depths (position along z-axis) of 15 mm, 20 mm, 25 mm, 30 mm, 35 mm, 40 mm and 45 mm were used. The eigenvalue spectrum plotted on logarithmic scale for the target at $z = 30$ mm is shown in Fig. 3. Similar eigenvalue spectra were obtained for other cases.
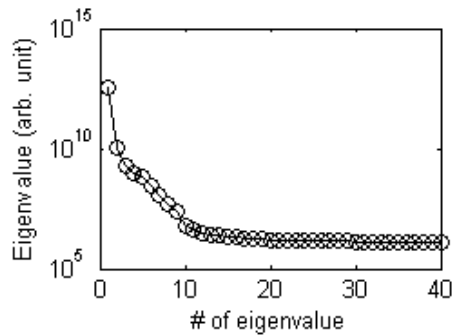

Fig. 3. A semi-log plot of eigenvalue spectrum with first 40 leading eigenvalues for the target at $z = 30$ mm.

Both SDDS and DSSD pseudo spectra were calculated using Eq. (20). The target was identified as an absorptive target. In the DSSD pseudo spectrum, the absorptive pseudo value at the peak position is ~41 times of the scattering pseudo value associated with $\partial_z g_d$, and even larger than those associated with $\partial_x g_d$, and $\partial_y g_d$, as shown in Table 2. Similarly in the SDDS scheme, the absorptive pseudo value at the peak position is ~33 times of the scattering pseudo value with $\partial_z g_s$, and much larger than the other two.

Table 2. Pseudo values associated with absorptive and scattering components at the peak position

Scheme with GFV (g)	Absorptive pseudo value	Scattering pseudo value		
		$\partial_x g$	$\partial_y g$	$\partial_z g$
DSSD (g_d)	1305.0	1.0	1.0	31.7
SDDS (g_s)	2729.3	14.0	1.1	81.6

Three-dimensional tomographic images were generated using the whole absorption pseudo spectrum for all voxel positions in the sample. The left pane of Fig. 4(a) shows a tomographic image for the target at $z = 30$ mm. The spatial profiles in the x, y and z directions, shown in the right pane of Fig. 4(a) were used to assess the target location. Similar images were generated for other depths. The retrieved target positions are compared with known positions in Table 3.

As is evident from Table 3, when DSSD scheme was used, the TROT-assessed lateral positions (x, y) were within 0.6 mm of the known values, which is an excellent agreement. The accuracy of the z-position was found to be optimal when the target was located in the middle plane of the sample, and deteriorated when the target was closer to the source plane or the detection plane. When using SDDS scheme, the TROT-assessed lateral positions were also within 0.6 mm of the known positions, except for $z = 40$ mm and 45 mm, where the error in y direction was 1.2 mm and 2 mm, respectively. However, remarkable improvement in the accuracy of the z-position estimation was observed, the error Δz being within 0.5 mm for all cases except for $z = 35$ mm, where the error was 1.5 mm. We ascribe the superior

performance of the scheme using T_{SDDS}, to the much larger size of the detector array (1024×1024) than that of the source array (9×9) used in the experimental arrangement.

Table 3. Positions of one target located at different depths

| Known Positions	DSSD Scheme		SDDS Scheme	
x, y, z (mm)	Retrieved Positions x, y, z (mm)	Error $\Delta x, \Delta y, \Delta z$ (mm)	Retrieved Positions x, y, z (mm)	Error $\Delta x, \Delta y, \Delta z$ (mm)
25.5, 24.7, 15	24.9, 24.4, 17.5	0.6, 0.3, 2.5	24.9, 25.2, 15.5	0.6, 0.5, 0.5
25.5, 24.7, 20	25.7, 24.4, 21.5	0.2, 0.3, 1.5	24.9, 25.2, 20.5	0.6, 0.5, 0.5
25.5, 24.7, 25	25.7, 24.4, 26.5	0.2, 0.3, 1.5	25.7, 24.4, 24.5	0.2, 0.3, 0.5
25.5, 24.7, 30	25.7, 24.4, 30.5	0.2, 0.3, 0.5	25.7, 25.2, 29.5	0.2, 0.5, 0.5
25.5, 24.7, 35	25.7, 25.2, 33.5	0.2, 0.5, 1.5	24.9, 24.4, 36.5	0.6, 0.3, 1.5
25.5, 24.7, 40	24.9, 25.2, 36.5	0.6, 0.5, 3.5	24.9, 25.9, 40.5	0.6, 1.2, 0.5
25.5, 24.7, 45	24.9, 25.2, 39.5	0.6, 0.5, 5.5	24.9, 26.7, 45.5	0.6, 2.0, 0.5
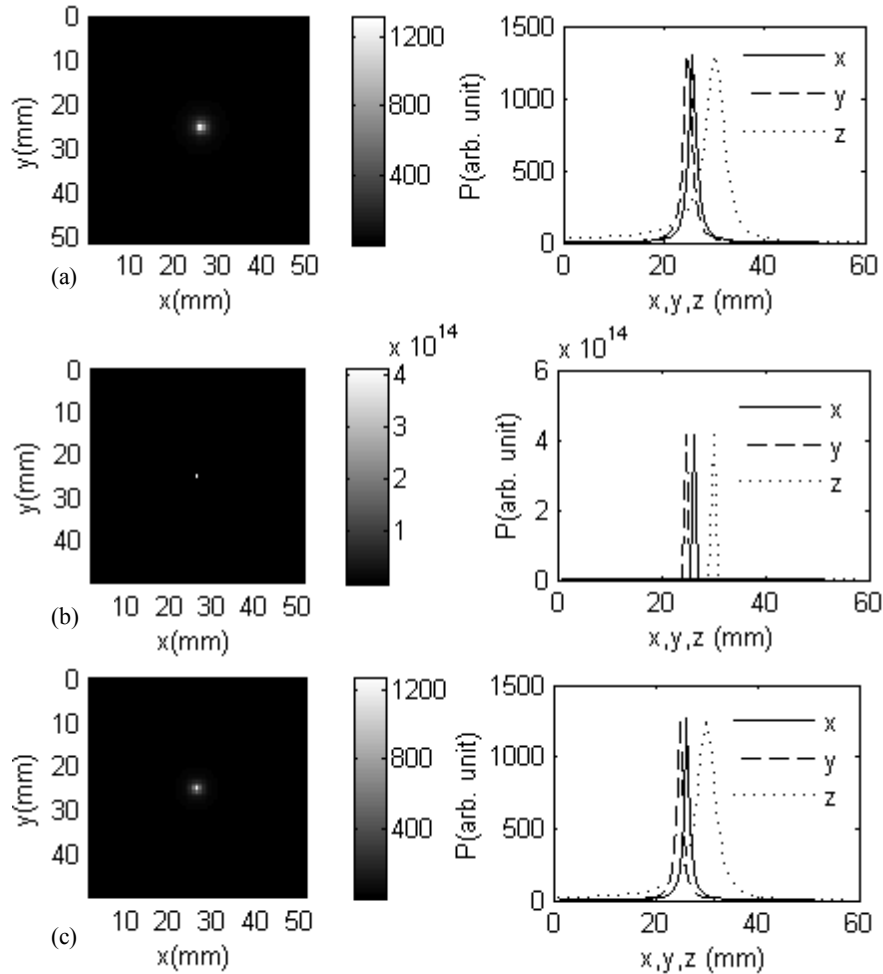
Fig. 4. Pseudo image of the target (left pane) and corresponding spatial intensity profiles (right pane) when the target is located at $z = 30$ mm: (a) experimental data; (b) simulation without any added noise; and (c) simulation with 20% Gaussian noise added. The pseudo values are calculated using Eq. (20).

It should be noted that the choice of either DSSD or SDDS scheme depends on experimental parameters, such as, the number and density of sources and detectors, and does not depend on the characteristics of the background medium. When more detectors than

sources are used and inter-detector spacing is small, SDDS would provide better resolution than DSSD, and vice versa. However, due to the diffusive nature of light propagation in the turbid medium, increasing the numbers and decreasing the spacing of the sources/detectors beyond a limit may not always improve the results.

While the target position could be obtained from the experimental data, it was observed that the difference between the smaller eigenvalues in the signal subspace and the larger eigenvalues in the noise subspace were not as pronounced as observed in the simulation in Section 4. To assess the effect of noise and to what extent noise may be present in the experimental data; we generated simulated data mimicking the experimental conditions, and added different noise levels. The lateral positions were (25.5 mm, 24.7 mm) and all seven z-positions (depth) of 15 mm, 20 mm, 25 mm, 30 mm, 35 mm, 40 mm, and 45 mm were tested. Typical pseudo images generated for $z = 30$ mm without and with 20% Gaussian multiplicative noise to compare with the experimental result are shown in Fig. 4(b) and Fig. 4(c), respectively. Simulated data provided the known position coordinates.

The simulated spatial profiles with zero added noise are much sharper than the profiles obtained from experimental data, or from simulated data with 20% added Gaussian noise. Broadening of spatial profile is an indication of the uncertainty in determination of position coordinates. Results from simulation show that uncertainty in position determination increases with added noise, and that experimental data behave in a way similar to simulated data with added noise.

5.3.2 Resolving two absorptive targets

In the second experiment using two targets the depth (z) and height (y) were kept same ($z = 30$ mm, $y = 26.0$ mm), while three different center-to-center separations, Δx of ~12.6 mm, 17.6 mm, and 27.6 mm, between them along the x-axis were considered. A cross-sectional pseudo image of the targets when separated by a center-to-center distance of 27.6 mm, generated using the pseudo spectrum is shown in the left pane of Fig. 5(a). Figure 5(b) shows a similar image for the separation 12.6 mm (separation between nearest edges ~4 mm). A similar image for the separation 17.6 mm was also obtained (not shown in the figure). The profiles in the x, y and z directions through the right target are shown in the right panes of Fig. 5(a)–Fig. 5(c). These profiles were used to assess locations of the targets, and the separation between the two targets. In all cases, the targets were determined to be absorptive, because peaks occurred in the pseudo spectrum with the GFVs corresponding to absorption property.

The known and retrieved positions from the experiments and separations Δx between the two targets appear in Table 4. In all the cases, the two targets were resolved, even when their center-to-center separation was 12.6 mm apart, nearest sides separated by only ~4 mm. For all retrieved positions, the maximum error in the lateral positions is 3.0 mm, and the maximum error in the axial positions is 1.5 mm. The errors in the lateral positions increase as the targets get closer. We ascribe this increase in error in the lateral position to the crosstalk between the two targets, the peak due to one target being affected by the other. The shift in the peaks is also affected by noise. When the two targets are very close or significant noise is present, the two peaks merge, so that the two targets are not resolved. This behavior was confirmed in simulations.

The results were compared with simulated data using similar conditions. For the more challenging case of two targets located at $z = 30$ mm and separated by 12.6 mm, exact target locations were found when no noise was added. With 10% noise present, the positions of the two targets were found to be (39.0 mm, 24.8 mm, 29.0 mm) and (30.0 mm, 24.8 mm, 29.0 mm) with target separation 9.0 mm, compared to 12.6 mm (known) and 6.9 mm retrieved from experiment. The pseudo image and the corresponding profiles through the right target are shown in Fig. 5(c). Similar images were also obtained for the left target. The retrieved separation between the two targets in simulation with 10% noise was smaller than the actual separation. But the error was less than the experimental result. However, when 20% noise was added, the two peaks merged (not shown here).
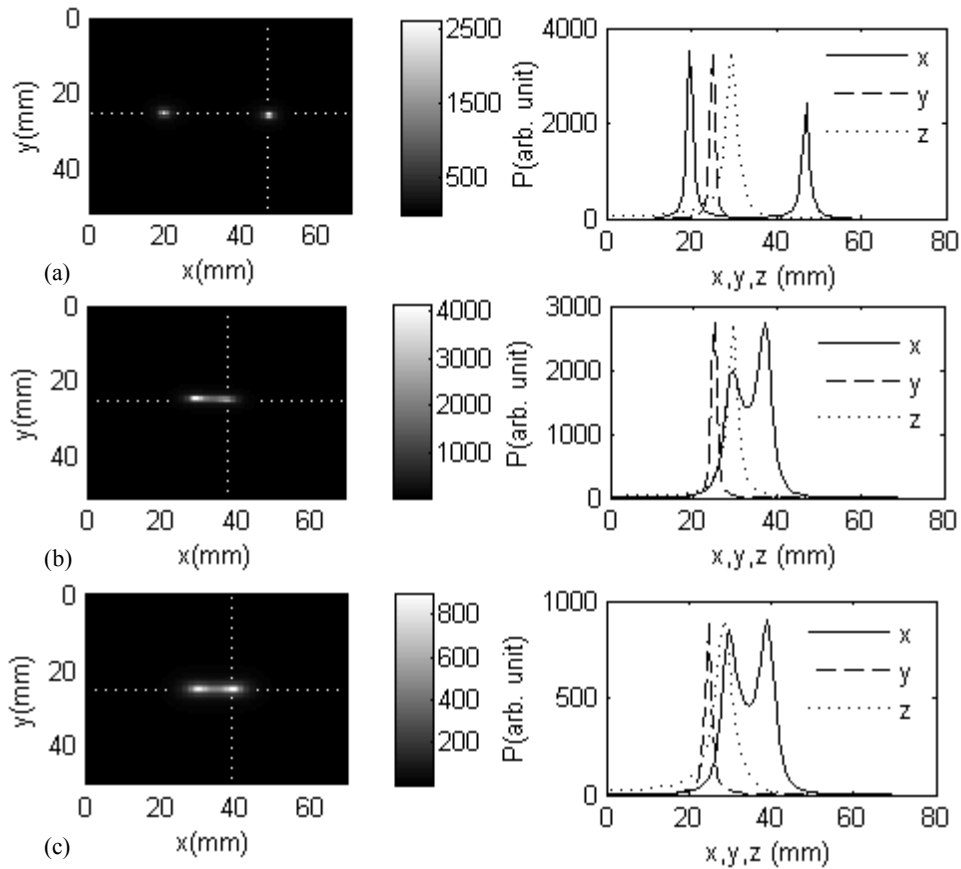
Fig. 5. (a) (Experiment): TROT generated cross-section pseudo image when the targets are separated by 27.6 mm is shown in the left pane and pseudo-value profiles through the right target along x, y and z directions are shown in the right pane. (b) (Experiment): TROT generated cross-section pseudo image when the targets are separated by 12.6 mm is shown in the left pane and the corresponding spatial profiles through the right target along x, y and z directions are shown in the right pane. (c) (Simulation): TROT generated cross-section pseudo image when two targets are separated by 12.6 mm is shown in the left pane and the corresponding pseudo-value profiles are plot in the right pane. In simulation 10% Gaussian noise is added for comparison with the experimental results. P is pseudo value calculated using Eq. (20).

Table 4. Positions of two targets separated with different distances

Known Separation [Δx (mm)]	Target #	Known Position [x, y, z (mm)]	Retrieved Position [x, y, z (mm)]	Error (mm)	Retrieved Separation [Δx (mm)]
12.6	1	27.6, 26.0, 30	30.3, 24.4, 28.5	2.7, 1.6, 1.5	6.9
	2	40.2, 26.0, 30	37.2, 25.2, 29.5	3.0, 0.8, 0.5	
17.6	1	25.1, 26.0, 30	26.4, 24.4, 28.5	1.3, 1.6, 1.5	14.6
	2	42.7, 26.0, 30	41.0, 25.2, 29.5	1.7, 0.8, 0.5	
27.6	1	20.1, 26.0, 30	19.5, 25.2, 29.5	0.6, 0.8, 0.5	27.6
	2	47.7, 26.0, 30	47.1, 25.2, 30.5	0.6, 0.8, 0.5	

The limits on the size of targets, separation between the targets, and the target-to-background contrast ratio that are needed to detect and locate the targets depend on noise level, experimental parameters (such as, number and concentration of sources and detectors), and ultimately on the diffuse nature of light propagation in the turbid medium. Coordinated experimental work and numerical modeling will be needed to assess those limits.

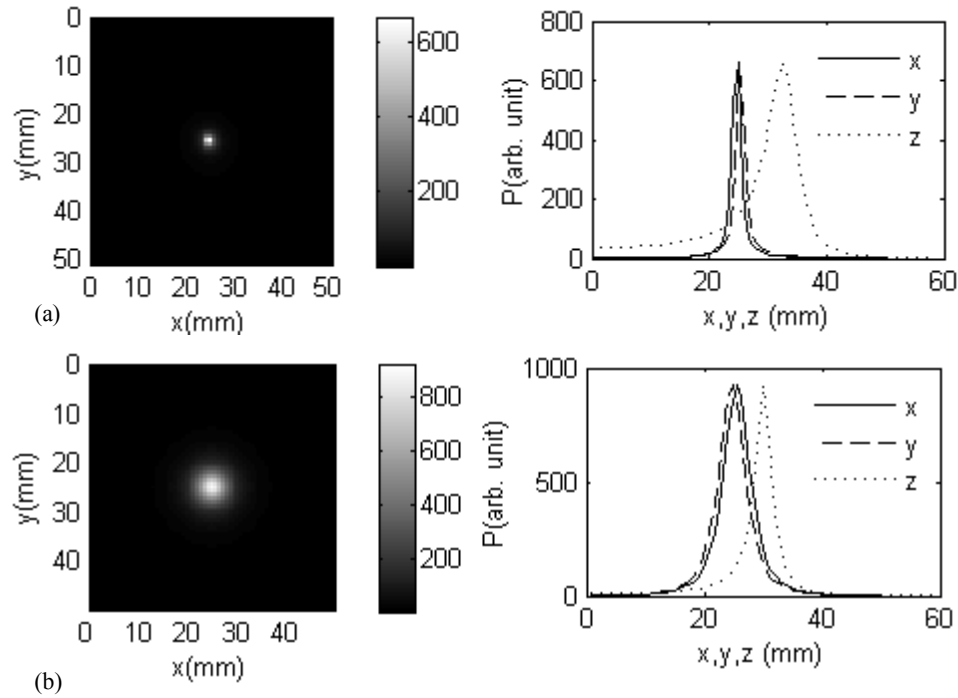### 5.3.3 Single scattering target at different depths

Fig. 6. Pseudo image of the target (left pane) and corresponding spatial intensity profiles (right pane) when the target is located at $z = 30$ mm: (a) experimental data; (b) simulation with 20% Gaussian noise added. P is pseudo value calculated using Eq. (20).

The experiment involving the third sample is the same as the first one except that the target was scattering in nature. The scattering target was a 10-mm diameter glass sphere filled with Intralipid-20% suspension in water, whose concentration was adjusted to provide $l_t = \sim 0.25$ mm, $\mu_s = 11.3$ mm^{-1}. The same scanning and data acquisition scheme was used as for the absorptive targets and the following z-positions of the target were used: 15 mm, 20 mm, 25 mm, 30 mm, 35 mm, 40 mm, and 45 mm. DSSD scheme was used to calculate the pseudo spectrum. A cross-section pseudo image and the corresponding spatial profiles are displayed in Fig. 6(a) when $z = 30$ mm. It is compared to the simulation results with 20% Gaussian noise (Fig. 6(b)). The lateral (x, y) spatial profiles of the pseudo image generated using simulated data are considerably wider, while the axial (z) spatial profile is narrower than those obtained using experimental data, and the peak values from the two cases are of the same order. The retrieved target positions are listed in Table 5. SDDS scheme was also used and provided with similar results.

Table 5. Positions of one scattering target located at different depths

Known Positions [x, y, z (mm)]	Retrieved Positions [x, y, z (mm)]	Error [Δx, Δy, Δz (mm)]
25.7, 24.5, 15	24.9, 25.9, 18.5	0.8, 1.4, 3.5
25.7, 24.5, 20	27.2, 26.7, 20.5	1.5, 2.2, 0.5
25.7, 24.5, 25	25.7, 26.7, 23.5	0.0, 2.2, 1.5
25.7, 24.5, 30	24.9, 25.2, 32.5	0.8, 0.7, 2.5
25.7, 24.5, 35	24.9, 25.2, 36.5	0.8, 0.7, 1.5
25.7, 24.5, 40	24.9, 25.9, 41.5	0.8, 1.4, 1.5
25.7, 24.5, 45	24.9, 25.9, 45.5	0.8, 1.4, 0.5

In Fig. 5, and more prominently in Fig. 6, the image resolution seems better for experimental data than simulated data. Since the peak values and bandwidth of lines (the

poles) in the pseudo spectrum depend strongly on the noise, this difference in image resolution is presumably due to lower noise level in the experiments than that used in simulations.

A comparison of experimental results for scattering and absorptive targets validate the common notion that it is more challenging to locate and image scattering targets than absorptive targets in a highly scattering medium. Also the lateral (x, y) positions are determined with higher accuracy than the axial (z) position. Overall the TROT-retrieved target positions are in good agreement with the known positions.

6. Discussion

The article presents the development of time reversal imaging approach with subspace classification, MUSIC in the optical domain. The results from experiment and simulation show that TROT is a faster and less computation intensive approach for detecting small targets in highly scattering turbid media and determining their locations in 3-D than other inverse image reconstruction techniques. While the dominant features in the pseudo spectrum are related to the square of the difference between the absorption (scattering) coefficient of the targets and that of the background, the approach does not directly determine these parameters. It is common for IIR approaches to estimate the optical properties of every voxel in the sample and identify target(s) from differences of these properties between the sample and the target(s), which is a considerably computation intensive undertaking. On the contrary, TROT identifies the targets as poles of the pseudo spectrum and focuses on determining their positions, which do not require as much computation time. Other IIR approaches involve iteration, while TROT is non-iterative. In TROT the data dimension is lower compared to other IIR approaches, which enables analysis and utilization of very large data sets. These two features together make TROT faster. Fast image reconstruction algorithms are of particular interest.

It was observed that lateral (x, y) positions are better determined than the depth (z). Also the spatial profile is more spread out along z compared to that along x, y. We ascribe this difference to fewer data along z-direction compared to those along x-y planes. Addition of another set of data with light incident and signal collected perpendicular to the z-direction is expected to further improve resolution in this dimension. Even without that addition, TROT determines the target position well.

While we have used slab geometry and CW illumination, the TROT approach may be used for other geometries (such as, cylindrical, and spherical), different types of illumination (e.g. frequency domain and pulsed) and different models for light propagation through the medium. Application and adaption of the TROT formalism to inhomogeneous media and extended targets may require careful consideration of several factors. In a non-uniform, inhomogeneous medium, structures other than the desired targets may appear as "false targets" and may interfere with identification of "real targets". However, as long as the contributions to the signal by any false target is smaller than that made by real targets, TROT with MUSIC will be useful in detecting and locating targets, by choosing a proper threshold to separate the signal and noise subspaces. What is even more important, expected wavelength dependence of the target spectroscopic properties could be used to assess the difference between the real and false targets in experiments using multi-wavelength interrogation of the sample.

The TROT formalism presented in this article is particularly suited for point-like targets requiring fewer eigenvectors in the signal subspace to construct a pseudo spectrum. However, for extended finite-size targets, the formalism needs to be modified and much more eigenvectors may be needed to calculate the pseudo spectrum [40,60,61]. These interesting problems for further study are currently being pursued.

Multi-functional tumor-targeting nanocomposites and time-reversal optical imaging for early detection of breast cancer and prevention of micro-metastases

Abstract of a pre-proposal submitted to the Idea Award (collaborative option) of BCRP 2011 by
S. K. Gayen (Initiating PI) and Valeria Balogh-Nair (Collaborating PI)
City College of New York

Research Idea

The *objective* of the proposed research is to develop multi-functional, tumor-targeting nanocomposites and near-infrared (NIR) optical imaging approaches for early detection of breast cancer, and prevention of micro-metastases that are responsible for majority of breast cancer mortality. The nanocomposite *synthesis* will use a multivalent dendrimer (a class of organic macromolecules) platform to incorporate fluorescent moieties (*e.g.*, semiconductor quantum dots, or gold/silver nanoparticles) as contrast agents for *imaging*, and chemokine mimics for *selective targeting* of cancer cells and *prevention* of metastases. The high affinity of chemokine mimic's ligands for chemokine CXCR4 receptors will ensure selective delivery of the nanocomposite to the target. A multi-source NIR probing and multi-detector signal acquisition arrangement along with a time-reversal image reconstruction algorithm will be used for fast detection of tumor and determination of its location in three dimensions.

Impact and Innovation

The *major impact* of the proposed research is that it has the potential to provide a modality for early detection of breast cancer, and for prevention of metastases, the major cause of mortality. A *broader potential impact* is that the approach could be extended to other cancers using chemokine mimics directed to other chemokine receptors.

The project is highly innovative in many ways. First, the synthesis process brings together the concept of multivalency, the idea of chemokine mimics for prevention of cancer cell migration, and use of dendrimers as stabilizers and nanoreactors for contrast agent synthesis. A combination of these novel ideas is proposed, to the best of our knowledge for the first time, as a multi-prong approach to fight the menace of breast cancer. Second, the affinity of the chemokine mimics to seven helix chemokine CXCR4 receptors obviates the need for a targeting vector. The chemokine mimics will play the dual role of: (1) "homing devices" for selective delivery of the nanocomposite to the tumor sites; and (2) "prevention agents" interacting with the chemokine receptor sites to inhibit metastases. Third, the efficacy of noninvasive NIR imaging approach for early detection and potential diagnosis will be significantly enhanced through design of efficient contrast agent. Fourth, the idea of time-reversal optical tomography (TROT) is a new paradigm in diffusive optical tomographic (DOT) imaging. While currently pursued DOT approaches are iterative and computation time intensive, TROT is non-iterative and will be faster, which is a necessary condition for real-time imaging. TROT is designed for detecting and locating small targets and will be suited for early detection when tumors are small. Finally, the dendrimer platform with multivalent surface will enable incorporation of moieties that enhance other imaging modalities, such as, magnetic resonance imaging, enabling development of sought-after dual or multimodal imaging modules.